UNIVERSITÀ DEGLI STUDI DI PAVIA
DOTTORATO DI RICERCA IN FISICA – XXXIV CICLO

Dynamic Nuclear Polarization of Beta-Cyclodextrin Derivatives

Efstathios Charlaftis

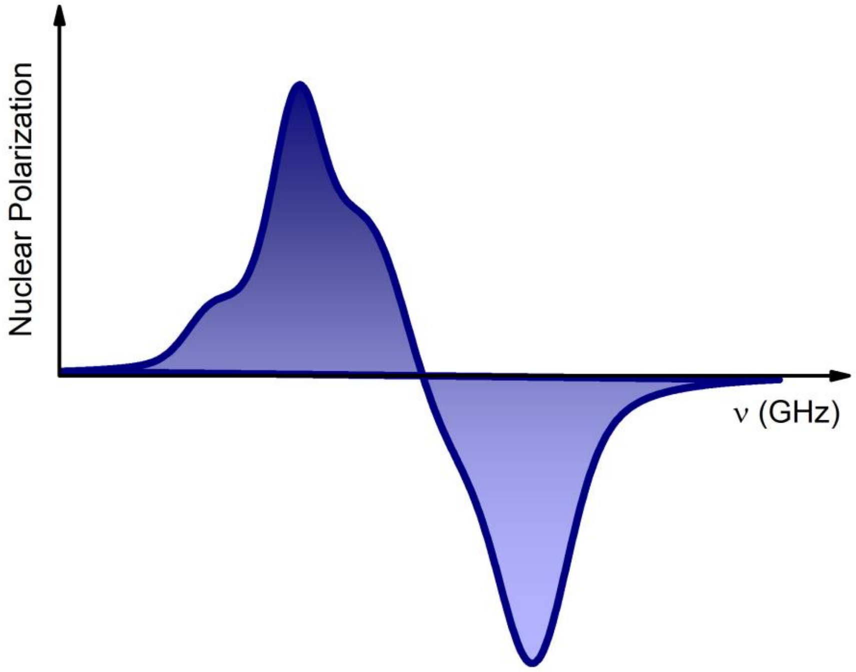

Tesi per il conseguimento del titolo

Università degli Studi di Pavia, Dipartimento di Fisica
PhD programme in Physics - XXXIV cycle
2021

Dynamic Nuclear Polarization of Beta-Cyclodextrin Derivatives

Submitted to the Graduate School of Physics by

EFSTATHIOS CHARLAFTIS

In partial fulfilment of the requirements for the degree of

DOCTOR OF PHILOSOPHY IN PHYSICS

Supervisor

Prof. Pietro Carretta

“Πάντα χρήματα ἦν ὁμοῦ, εἶτα νοῦς ἐλθὼν αὐτὰ διεκόσμησε.”

“In the beginning all things were the same, then the mind came and [distinguished them] and classified them.”

– *Anaxagoras, 500-428 BC*

Contents

Introduction

Nuclear magnetic resonance (NMR) is one of the most powerful, weakly perturbing spectroscopic techniques which can be applied in different sectors not only for scientific research but also in everyday life. In physics[1], it is well suited for probing the microscopic properties of materials, as the spin and the molecular dynamics. In medicine[2, 3], where the NMR takes the form of the magnetic resonance imaging (MRI) it is used for medical diagnosis, to form and provide images of the anatomy and the physiological processes in the human body. In chemistry[4] and pharmaceutical sciences[5] it is extremely useful since it can provide information about the type and the relative amounts of atoms present in the sample, the specific environments of atoms within a molecule, the purity and the composition of a sample and the structural determination and dynamics of macromolecules and compounds with further applications to the food industry[6].

In practice, this technique exploits the nuclear spins as local probes to investigate the properties of matter under a static magnetic field by applying suitable radiofrequency pulse sequences to excite the nuclear spin system. The main limitation of NMR is its low sensitivity at room temperature which results from both, the small separation of the nuclear Zeeman energy levels, much lower than the thermal energy, as well as the small magnetic moment which gives rise to a small magnetization to which the NMR signal is proportional. Different techniques of hyperpolarization have been devised to overcome this limitation and amplify the NMR signal and one of the most important among them is the dynamic nuclear polarization (DNP)[7, 8]. This technique is used in order to amplify the nuclear polarization, that is, to force the population in a single energy level (typically the lower). The DNP can be achieved in samples with homogeneously dispersed paramagnetic centres that contain unpaired electrons. The polarization of the electronic system is transferred through hyperfine interactions to the nuclear system after irradiation with microwaves close to the Larmor frequency of the electrons. Thanks to the huge enhancement of the NMR signal the hyperpolarized substrate can be used to perform the in vivo molecular imaging, aimed at following the real time evolution of metabolic and physiological processes. There are four different mechanisms that bring the polarization transfer. One of them, typically observed in metals, is the Overhauser Effect (OE)[9] by which the polarization is transferred from the conduction free electrons to the nuclei by the Fermi contact interaction. The other three are present in insulating systems where the unpaired electrons are typically added in the form of radicals. The Solid Effect (SE)[10] is induced in the case of narrow electron spin resonance (ESR) lines and requires low concentration of radicals with respect to the nuclei and induces the simultaneous flips of electron and nuclear spins that in general are prohibited. The last two, Thermal Mixing (TM)[11] and Cross Effect (CE)[12] are relevant in the case of the broad ESR lines and require somewhat higher concentrations of radicals than for the previous processes. The polarization transfer in this case is achieved through the triple spin mechanism; a mechanism that predicts the simultaneous flip of two electron and one nuclear spins.

The aim of this thesis is the implementation of the DNP technique to organic compounds of biomedical interest, such as the β-Cyclodextrin (CD) macromolecules, with final goal the application of them in molecular imaging studies. CDs[13, 14] are basically sugar macromolecules bound together in a conical form having a hydrophobic internal cavity and a hydrophilic external surface which contributes to optimize the solubility. The shape of these macromolecules is suitable to host inside the cavity different compounds of various interests, like other molecules and active principles, that are protected from the external environments. Thanks to the non-toxicity and the great solubility they have many applications in biomedicine, chemistry and pharmaceutical sciences. In particular, owing to their physicochemical properties CDs doped with radicals can be used as very efficient contrast agents that increase the quality of the MRI images, reduce the dose of contrast liquids and the time needed for an MRI scanning becoming also a vehicle for drug delivery. Thus they can merge, in a way, the diagnosis with the therapy.

This dissertation is divided into four chapters. In the first chapter a general introduction to the utility of the macromolecules to the biomedical sector, implementing the DNP technique, is presented. Then, a description of the molecular structure and of the properties of the cyclodextrins is given as well as the vast applicability of these organic materials to the different scientific, and not only, sectors. Finally, we present the samples studied in this work (CD derivatives) in detail, alongside with the synthesis process.

The second chapter introduces the basic concepts of the nuclear and electron magnetic resonance. We start by a quick introduction of the most important NMR applications and its evolution through the years followed by the classical and the quantum mechanical description of the nuclear spin resonance. We introduce the Bloch equations for the time evolution of the magnetization concluding with the theoretical analysis of the spin-lattice and spin-spin relaxation time which are important tools in order to investigate the local environment. The effect of the molecular motions to the NMR spectrum is also indicated. At the end we introduce the basic aspects of the electron paramagnetic resonance (EPR) giving emphasis to the Zeeman anisotropy factor and the effect of the hyperfine interactions on the EPR spectra, concluding with the informations that one can obtain analysing the properties of an EPR spectra.

The third chapter describes the nuclear hyperpolarization processes. The main hyperpolarization techniques that were used over the years are presented like the Brute Force method, the Spin Exchange Optical Pumping, the Parahydrogen Induced polarization and the Nitrogen-Vacancies in diamonds; achieved physically by optical and microwave excitation of the electronic system or chemically through reactions. Emphasis is given to the microwave-driven hyperpolarization like in the Overhauser Effect, in the Solid Effect, in the Thermal Mixing and in the Cross-Effect. In particular the Thermal Mixing is the one describing the systems under investigation.

In the final chapter, after a brief presentation of the experimental set-up and techniques, the main NMR-DNP and EPR experimental results are presented and discussed in view of the possible applications. In particular, the first part is dedicated to the DNP performance (NMR signal enhancement and enhanced nuclear polarization) of the ^{1}H and ^{13}C nuclei at low temperatures ($1.6\,K \leq T \leq 4.2\,K$). In the second part we exploit the relaxation mechanisms of the nuclei and the time that they remain in the hyperpolarized state, in the same temperature range, investigating the DNP mechanism responsible for the polarization transfer. The final part is dedicated to the temperature dependence of ^{1}H and ^{13}C relaxation times over a large temperature range ($10\,K \leq T \leq 320\,K$). Specific attention has been paid to the motion of the molecules at high temperatures that, as expected, affect the NMR spectrum.

After the concluding remarks of this work, it is presented in the appendix the experimental set-up of the NMR, DNP and EPR studies, described in detail, as well as a table containing all the samples that were studied.

Chapter 1

Macromolecules for dynamic nuclear polarization: Cyclodextrins

Nuclear magnetic resonance (NMR) and magnetic resonance imaging (MRI) become particularly useful in the area of the preclinical molecular imaging with the application of hyperpolarization techniques[15]. So far, MRI has been mainly applied to ^{1}H nuclei because they are characterised by the highest gyromagnetic ratio (42.577 $\frac{MHz}{T}$) of all the other active NMR nuclei and also because of their large abundance in the living tissues, which contain a lot of water molecules. With the introduction of the DNP technique also other nuclei with lower gyromagnetic ratio can be investigated, such as ^{13}C. This makes possible a far more effective imaging and also enables, for example, the real time study of the metabolic processes and of the blood flux by analysing the in-vivo distribution of the molecules[16]. Over the past decade there have been numerous studies on various organic compounds that can be used in the field of molecular imaging thanks to their general DNP performance, that is, the total signal enhancement and the time that the system can remain in the hyperpolarized state. In fact some of them, like the pyruvic acid[17], are already in use and have been widely tested in mice and small animals, showing promising results for preclinical molecular imaging.

For the application of the DNP technique the presence of radicals or metal ions is essential[18]. A radical is a small paramagnetic molecule that contains at least one unpaired valence electron. Such molecules are added in order to provide the system with free electrons for the realisation of the polarization transfer to the nuclei of interest. DNP performance strongly depends on the local characteristics of these unpaired electrons like the homogeneous and the inhomogeneous linewidth of the electron paramagnetic resonance (EPR) spectrum, the electron Larmor frequency and the g-anisotropy of the molecule. At low magnetic fields ($H < 7$ T) where the g-factor anisotropy does not play a significant role one can use radicals like TEMPO (aminoxyl radical). At higher fields, because of the dominant Zeeman interaction, BDPA- (Koelsch carbon centred radical) and trityl-type radicals are usually preferred. Of course, one should consider that the introduction of radical molecules to the system affects important biophysical parameters like the solubility, the absorption and the toxicity. All these parameters should be controlled before an out of the laboratory testing.

One of the most important areas in the field is the development of gas or liquid metabolites (substrates) that contain hyperpolarized agents. The tricky part here is to choose wisely the suitable type of substrate in order to examine a specific part of the body and also to combine it with an NMR active nuclei that in total, as a system, will offer not only good DNP performance but it will also be safe for the patient.The most common liquid phase hyperpolarized agents include the active nuclei ^{13}C, ^{15}N and small endogenous molecules that take actively part in various metabolic circles [19] like pyruvate, fumarate, urea, glucose and others. For example, using hyperpolarized ^{13}C-pyruvate one can study the metabolism of the brain[20] by monitoring in real time the transformation of pyruvate to lactate by tracking the signal of the carbon nuclei. Non healthy tissues of the brain will have an increased metabolic rate and this results in different quantities of the metabolites that can be traced by MRI. On the other hand, because of the low density of ^{1}H nuclei in the lungs, hyperpolarized ^{3}He and ^{129}Xe in gaseous mixtures are used for the magnetic imaging in lungs[21]. Initially ^{3}He was used mainly because of its large diffusion coefficient but due to the small natural resources of helium and its high cost ^{129}Xe enriched xenon gas started to be used. Hyperpolarized xenon gas demonstrated also the ability to defuse into blood and tissues from the gas phase enabling the measurement of the perfusion and the gas exchange in the blood plasma.

In the present study we have worked with a particular kind of macromolecules that belong to the family of cage molecules, the cyclodextrins[22]. They represent one of the most studied biomolecular compounds basically because of low absorbency index by the molecular membrane and thus the low chance of being metabolised, becoming very efficient transport vehicles of hydrophobic substances increasing aqueous solubility. The physicochemical properties of the CDs in combination with the relative low fabrication cost and the variety of sizes makes them an important, multi-purpose substrate for hyperpolarized agents but have also found a number of applications in a wide range of fields such as pharmacology[23] and food industry[24].

1.1 Structure and physicochemical properties

Cyclodextrins are the crystallites that are formed after the enzymatic degradation of starch (transglycosylation) through heating. First it was Antoine Villiers[25] in the 19^{th} century who studied the reaction and discovered its products. Soon later Schardinger[26] classified these molecules into three categories, $\alpha-$, $\beta-$ and $\gamma-$ CDs, depending on their size and structure. In literature[27] there is a confusion over the name of these molecules since they can also be found with other names like cyclomaltoses, cycloamyloses or just Schardinger dextrins, but the name cyclodextrins has prevailed. These three types are the most common ones while now more complex cyclodextrin structures have been synthesized, with up to 13 glucopyranose units ($C_6H_{12}O_6$)[28]. The $\alpha-$CD is the smallest possible one that can be fabricated, containing 6 glucopyranose units. Formation of even smaller CDs is prevented by steric factors[29].

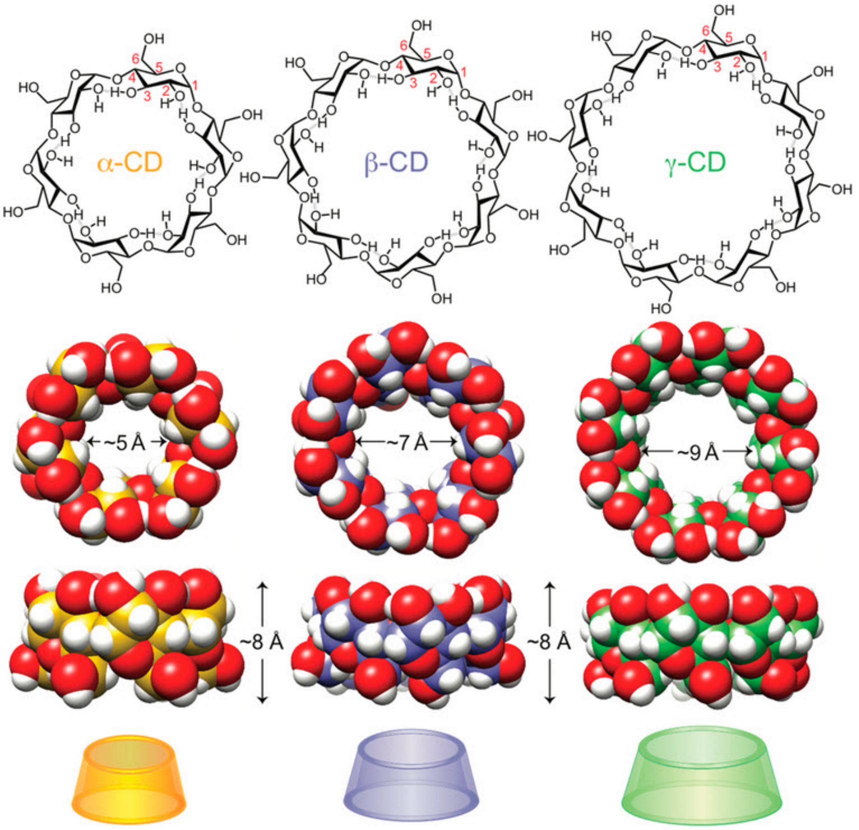

Figure 1.1: (top) Chemical structure of the $\alpha-$CD ($C_{36}H_{60}O_{30}$), $\beta-$CD ($C_{42}H_{70}O_{35}$) and $\gamma-$CD ($C_{48}H_{80}O_{40}$); (middle) three-dimensional representation of the cyclodextrin molecules where the red and white spheres depict the oxygen and hydrogen nuclei while the carbon nuclei are depicted by the colourful spheres for each CD category. The relevant dimensions can also be seen; (bottom) schematic representation of the CDs. Figure adapted from *Bruns et al.* [30].

They are formed by long sugar molecular chains bound together forming an empty truncated cone-like shape as we can see in figure 1.1. On the top of this figure we have the chemical structure of the three CD types while, in the middle, we can see the three-dimensional scheme of the macromolecules, where the white and red spheres represent the hydrogen and the oxygen nuclei, respectively, and the colourful spheres represent the carbon nuclei of each different CD type. We can also observe that the height of the cone is independent of the number of the monomers (~0.8 nm) while we have a significant change in the diameter of the cone (~0.5 nm, ~0.7 nm and ~0.9 nm). In the bottom, we can see also the classification of the different kinds of CDs depending on the number n of the monomers of glucopyranose. The larger the number of the monomers, the larger the CD macromolecule and the larger the cavity.

The importance of the CDs relies on their physicochemical properties[31]. By the term physical properties it is meant the cavity size, as it can be grasped from figure 1.2, it acts like a host-guest system with various compounds in the solid, liquid or gas phase, which can lie inside the cavity, giving rise to inclusion complexes[32]. Of course, the size of the guest-molecule has to be compatible with the size of the cavity. Thanks to the many different kinds of CDs, a variety of molecules can be guested.

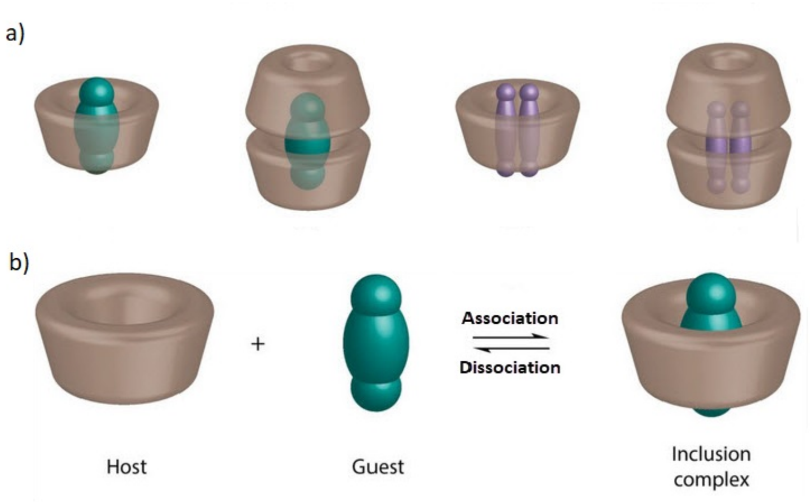

Figure 1.2: Schematic representation of a) the possible host-guest systems that form inclusion complexes and b) the association-dissociation of the guest-molecules from the CD cavity. Figures adapted from *Kfoury et al.* [33].

As regards the chemical properties, the chemical reactivity of the internal and external surface of the macromolecules can vary. The exterior of the molecules is hydrophilic which makes the molecule compatible with a solvent. In fact, the narrower and the wider rims of the ring, which are also called primary and secondary faces respectively, contain several unbound hydroxylic (OH-) groups. These OH groups can easily make bonds with the molecules of the solvent where the CDs are immersed and this gives rise to a high solubility[34]. As a result there is no aggregation of CDs in a solvent and moreover the guest-molecules cannot interact with external of the CDs. On the other hand, the internal surface is apolar, which means that it is hydrophobic. Thus, the water molecules are expelled by the internal cavity and the host-guest interaction inside the cavity is non-covalent. This implies that the association- dissociation has a low energy cost and is reversible (fig. 1.2). In fact, the interactions inside the cavity can be hydrogen bonding or weak van der Waals ones depending on the nature of the guest-molecule.

The dissociation of the host-guest system and the realise of the guest[35] can be achieved either slowly by the natural degradation of the CDs or instantaneously by simple dilution, a quick temperature change or dynamic phosphorescence decay[36, 37, 38]. Of course, the stronger is the bonding in the internal cavity the slower are the relative kinetics for the dissociation[36].

1.2 Applications

Due to the fact that CDs do not modify the physical, chemical and biological properties of guest-molecules by formation of inclusion complexes with diverse molecules, they offer versatile benefits in the pharmaceutical[39, 40], in the food industry[41] as well as in the cosmetics[42].

CDs play an important role in the chemical stability of drugs, since the guest-molecule captured inside the cavity is protected from many external factors like oxidation, UV radiation, extreme pH conditions and heat. Also different types of chemical reactions like hydrolysis, dehydration and isomerization slow down due to the minimization of the free interacting surface of the molecule. The macromolecule walls act like a shield protecting the drug molecule and making it more resistant and thus more efficient.

A drug substance has to have a certain level of water solubility to be readily delivered to the cellular membrane, but it needs to be hydrophobic enough to cross the membrane. If not, then a very small amount of drug reaches the inside area of the cell and becomes less efficient. Enhancement of solubility of the drug further helps in the better bioavailability and hence more therapeutic efficiency of the dosage form. This is exactly what CDs have to offer, a soluble transport vehicle that permits the controlled drug delivery and deposition through the bio-membrane inside the cell.

The use of CDs in food processing and as food additives mainly focuses on the delay and prevention of food molecular degradation by isolating the system from oxygen, light and heat. Moreover, they are also widely used for stabilization of flavours, for the removal of offensive tastes and other undesirable compounds. By controlling the volatility of the substances CDs are able to trap specific molecules, unpleasant to human, compounds and protect others, contributing to the quality and stability of food products. Because of this, CDs serve also as very efficient packaging material.

Recent use of CDs has been discovered in the field of the cosmetic preparation. The advantage that CDs have to offer lies on the preservation of stability, the odour control and of course the protection of the active cosmetic compounds from heat, light and humidity.

1.3 Samples under investigation

In this work we have studied different variations of β-CD compounds by means of NMR and EPR spectroscopies and for the application of the DNP technique. All the samples mentioned in this chapter were synthesised by Lucio Melone from the Polytechnic University of Milan. The goal of the study is the implementation of the DNP technique in cyclodextrin derivatives in order to enhance the ^{1}H and ^{13}C NMR, and accordingly, MRI signal, making them promising candidates for molecular imaging applications. Usually, in MRI studies, there are used contrast agents that contain paramagnetic ions and the difference in the intensity of the signal that is coming from the tissues relies on the intensity of the T_1 and T_2 nuclear relaxation times. In our case, we use hyperpolarization to enhance selectively, the signal of molecules that are involved in the human metabolize. In the sites where these molecules are located the MRI signal is enhanced.

More specifically, attention has been focused on three different sample categories formed mainly by β-CD macromolecules and TEMPO radicals to provide the system with the necessary free electrons for the DNP study. Differences among the samples, corresponding for example to the addition of methyl-groups or to the deuteration of the samples have been applied in order to maximize the general DNP performance, taking also care of the future application of them in the health sector. As it will be mentioned in the following, these changes were performed in order to reduce the spin-lattice relaxation rate which determines the life-time of the hyperpolarized state. For all these three categories the synthesis strategy is almost the same but with slight modifications, reported in the following references[43, 44, 45, 46].

In order to induce hyperpolarization the nuclei of the compound under study have to interact with unpaired electrons that, after irradiation close to the electron Larmor frequency, they transfer the polarization. Here, the radical TEMPO ([2,2,6,6-tetramethylpiperidin-1-yl]oxyl) introduces the unpaired electron. TEMPO is a paramagnetic, stable ring structured organic molecule, with the unpaired electron strongly localized on the nitroxide ($NO^{\cdot}$) group and chemical formula $C_9H_{18}NO$. TEMPO was discovered by Lebedev and Kazarnowskii[47] in 1960 and has the form of reddish crystallites.

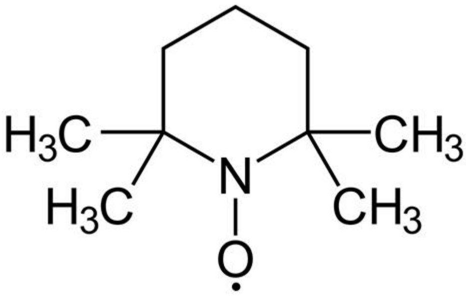

Figure 1.3: Chemical structure of the TEMPO radical.

The g-factor of TEMPO shows a small anisotropy while its average value is comparable to the free electron one[48]. Its electron spin resonance (ESR) linewidth is broad and this could be a first indication that the DNP mechanism responsible for the polarization transfer is the Thermal Mixing[49, 11, 50, 51] (see also section 3.5.3). The inert CH_3 groups around the molecule offer a great chemical stability. Thanks to the stability and the great solubility in water and alcohol, it constitutes the perfect candidate for the DNP-NMR measurements of materials of biomolecular interest[52]. Hereafter we present more in detail each one of the *beta*-CDs families studied in this work doped with a single or multi (Hepta-TEMPO) TEMPO unities.

1.3.1 Completely methylated β-CDs

For this sample category we focused on the completely methylated β-Cyclodextrins[45] with chemical formula $[C_{42}\,{}^{13}C_{21}H_{49}D_{63}O_{35}]$. Regarding previous works[43, 44] we obtained good DNP performance in these rarely studied molecules but a somehow short relaxation time at room temperature; which could be detrimental for applications. Here the molecules are optimized by a total deuteration of the samples by a 1:1 substitution of the ^{1}H atoms of the methyl groups with ^2D atoms. According to the literature[53, 54, 55] this will increase the nuclear relaxation time by at least a factor of ten. With the deuteration we have a reduction of the nuclear magnetic moment that results into a reduced fluctuating magnetic field and consequently, to a longer relaxation time T_1 which is necessary to maintain the hyperpolarized state for longer. Through the methylation by the methyl-agent $^{13}CD_3$ (1:3 carbon to deuterium atoms) we achieved the enriched macromolecules with ^{13}C and ^2D atoms but also increased its solubility making it interesting for pharmaceutical purposes. Two samples for this category were prepared, one of them doped with 11% in weight TEMPO radicals while the other one undoped.

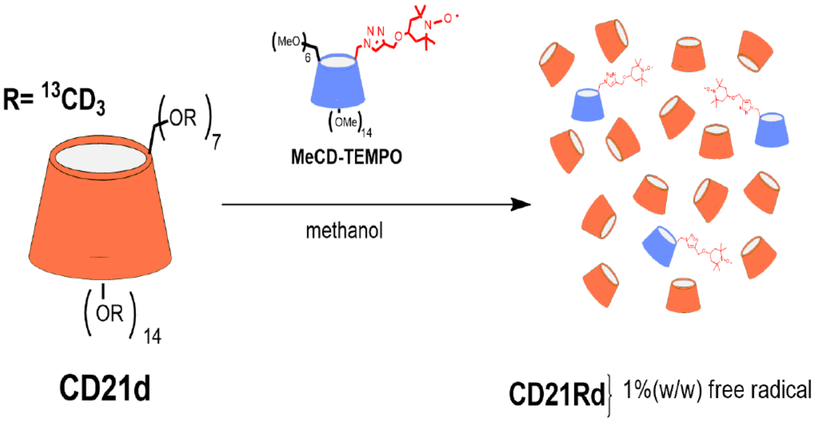

Figure 1.4: Schematic view of the synthesis procedure of CD21Rd sample by doping of the CD21d sample in methanol with MeCD-TEMPO.

For the synthesis of the undoped sample CD21d, weighted amounts of pure $\beta - CD$ were dissolved in dimethylformamide (DMF). Sodium hydride (60% in mineral oil) was added and the mixture was stirred for 30 minutes at $0°C$ in a N_2 environment and $^{13}CD_3I$ dissolved in DMF was added to the mixture. After 24 hours in N_2 the excess of NaH was removed with H_2O and the product was extracted with chloroform. The pure product was afforded after purification on an SiO_2 column and evaporation.

In order to dope the sample with radicals a doped CD derivative was synthesised (MeCD-TEMPO)[44, 56, 46]. Weighted amounts of Permethylated βCD-azide (MeCD-N_3) was mixed in methanol with propargyl-TEMPO, CuI and drops of Et_3N. After stirring for 24 hours at $50°C$ under N_2 the mixure was obtained after extraction with EtOAc, purification on an SiO_2 column and evaporation. The doped sample CD21Rd was obtained by mixing weighted amounts of CD21d and MeCD-TEMPO in methanol. After 10 minutes of stirring the final sample was recover after vacuum evaporation. The amount of radical doping (% w/w) is given by the formula:

$$\%TEMPO = 100 \times \frac{\frac{M_{MeCD-TEMPO}}{1650.82} \times 156.25}{M_{CD21d} + M_{MeCD-TEMPO}}, \tag{1.1}$$

where 1650.82 and 156.25 are the MeCD-TEMPO and TEMPO molar masses, respectively.

1.3.2 Hepta-TEMPO and Mono-TEMPO doped randomly methylated β-CDs

The need for new, non harmful and equally or more effective metal-free contrast agents for preclinical MRI studies leads to the fabrication of these samples. The goal here was to prepare a molecule that has a high enough effective magnetic moment to lead to a more efficient transfer of the polarization to the nuclei, offering high MRI resolution, regarding the diffused gadolinium complexes[57, 58], but less toxic[59]. Poly-nitroxides seem to be good candidates for this purpose[60, 61, 62]. In combination with the property of cyclodextrins[63], thanks to the numerous free OH bonds on their outer surface, the Hepta-TEMPO poly-nitroxide was fabricated. The interesting part here is that, all the seven hydroxyl groups of the small rim of the molecule are occupied with TEMPO radical moieties while, in the Mono-TEMPO lot, the initial material is doped with β-CDs that contain single TEMPO radical moieties[46].

For the synthesis of the Hepta-TEMPO samples a selective substitution of all hydroxyl groups of the small rim of the molecule with iodine atoms was achieved by a standard procedure[64]. The iodine atoms were then replaced by azide[65] and the mixture was dissolved in DMF with weighted amounts of propargyl-TEMPO, CuI and Et_3N drops. The product was recovered with the same purification method used before. The final samples were obtained by

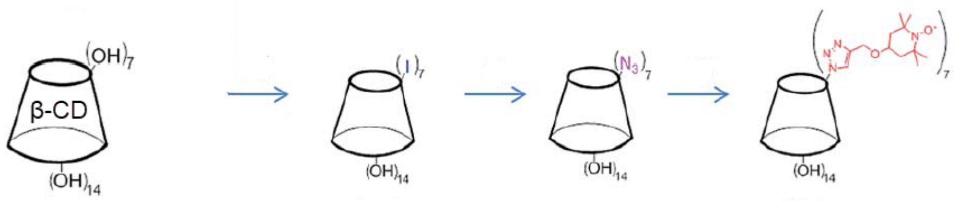

Figure 1.5: Step by step preparation of the Hepta-TEMPO β-CDs from the bare β-CD macromolecule. The seven TEMPO moieties cover the small rim of the cyclodextrin molecule. Figure adapted from *Caglieris et al.* [46].

mixing the A_0 sample (RAMEB) with different quantities of Hepta-TEMPO radical doped $\beta-$CD derivatives dissolved in methanol and stirred for 10 min. The final product was recovered after solvent evaporation under vacuum.

For the synthesis of Mono-TEMPO weighted amounts of RAMEB and MeCD-TEMPO were dissolved in methanol and after stirring the solid samples were recovered after solvent evaporation under vacuum. For the synthesis of the MeCD-TEMPO the same procedure as in the subsection 1.3.1 was followed.

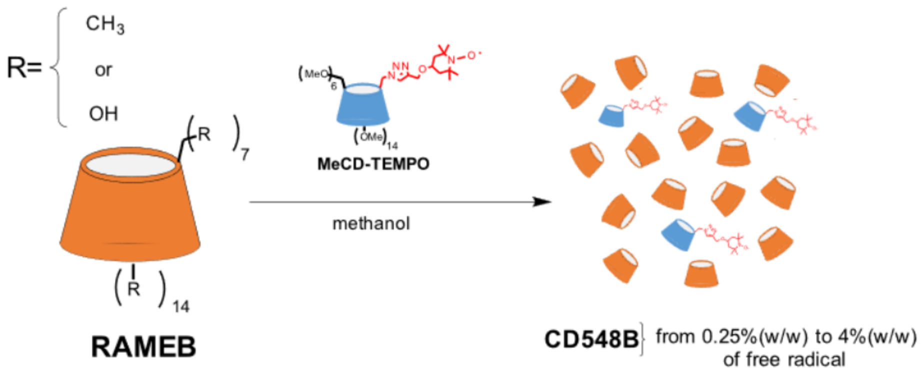

Figure 1.6: Schematic view of the synthesis of the Mono-TEMPO β-CDs after mixture of RAMEB and different quantities of MeCD-TEMPO in methanol.

1.3.3 Acetylated β-CDs

The good DNP performance of the completely methylated β-CD samples drove us to improve the disadvantage of the fast nuclear relaxation time at room temperature. The substitution of the CD_3 groups with carboxyl groups is expected to provide much longer relaxation times, since methyl motion contribution to the relaxation are avoided and since ^{16}O nuclei are characterised by a nuclear spin equal to zero. The acetylated samples were prepared of β-CDs with an average number of 7 carboxyl groups (COOH) per cyclodextrin molecule. All of the COOH groups are marked with ^{13}C that are the nuclei of interest for the NMR-DNP study. For this sample category 2 samples were prepared one of them with addition of TEMPO radicals and the other without.

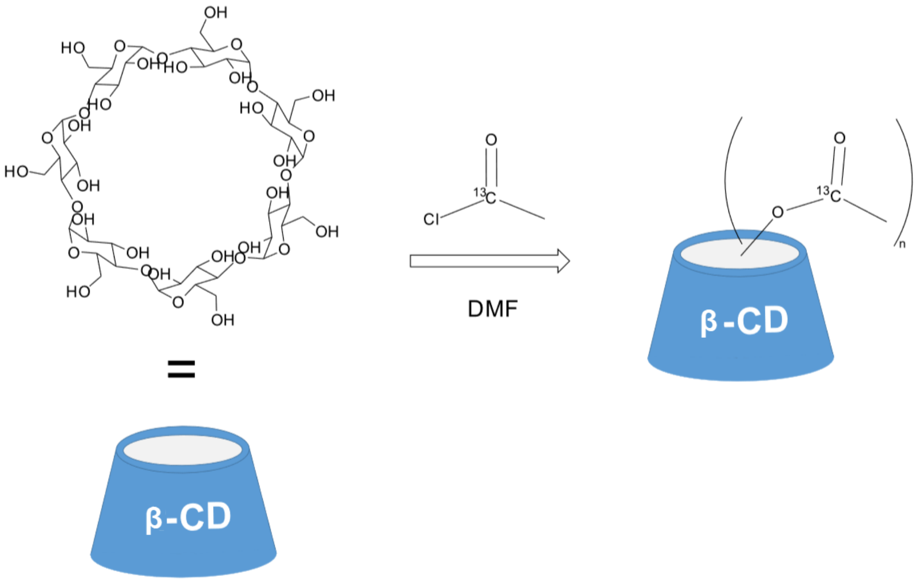

Figure 1.7: Schematic view of the synthesis of CD585 sample. The average value of n is 7.

For the preparation of the CD585 sample a weighted amount of commercially available β-CD was dissolved in DMF into a two-necked flask and cooled down to $0°C$. Acetyl-chloride-1-^{13}C was added by drops under a N_2 flow. After 3 hours stirring the sample was obtained by precipitation in EtOAc and purification by washing (4 times) using EtOAc and CHCl. In order to synthesise the doped sample CD586 the same procedure as in the completely methylated sample (CD21Rd) was followed (see subsection 1.3.1) with the final product been doped with 1% in weight TEMPO.

All the aforementioned samples form amorphous glasses upon cooling down with the glass transition occurring around 260 K. We will see that this property of the cyclodextrin samples will play an important role in the analysis of the experimental results since the glassy dynamics at low temperatures and the glass transition at higher temperature dominate the nuclear relaxation.

Chapter 2

Basic aspects of nuclear and electron magnetic resonance

Nuclear magnetic resonance (NMR)[66] is a powerful technique already in use for several decades[67] that is applied to various disciplines. It is a non-invasive technique where one uses the nuclei (table 2.1) as probes of a sample and monitors their response after excitation with radio-frequency fields. The information that can be obtained by NMR has applications to a wide range of fields like physics, chemistry, geochemistry and biology, biomedicine, food industry and cultural heritage. In physics[68] the NMR spectrum and relaxation times provide relevant information on the local magnetic and electronic properties, which are present in the system. In chemistry[69] NMR is an important tool because reveals information about the type and the neighbour of the nuclei. By studying the NMR spectra one can distinguish and identify different isotopic nuclei[70] but also can study the interaction between close nuclei[71] and follow the chemical reactions. In this way it is possible the identification of unknown samples but also their control for the possible existence of impurities.

Nucleus	**Spin**	**Nat. abundance(%)**	$\frac{\gamma}{2\pi}(\mathbf{MHz \cdot T^{-1}})$
^{1}H	$\frac{1}{2}$	99.985	42.577
^{13}C	$\frac{1}{2}$	1.108	10.7084
^{14}N	1	99.63	3.077
^{17}O	$\frac{5}{2}$	0.037	-5.772
^{19}F	$\frac{1}{2}$	100	40.078
^{23}N	$\frac{3}{2}$	100	11.262
^{31}P	$\frac{1}{2}$	100	17.235
^{39}K	$\frac{3}{2}$	93.08	1.98

Table 2.1: Common NMR active isotopes. Their spin value, natural abundance and gyromagnetic ratio are reported.

In biology[72] this technique is important for the reconstruction of the structure of molecules and proteins[73]. Since proteins have low symmetry, it is difficult to study their structures by means of the common spectroscopic techniques. With NMR and especially 2D-NMR[74] by locating a specific nucleus and studying its environment, it is possible to reconstruct pieces of highly asymmetric proteins and then proceed to the discovery of its exact structure.

The projection of NMR into the biomedical sector is the magnetic resonance imaging (MRI)[75]. By using a magnetic field gradient one can spatially separate the resonance frequencies and thus, obtain information about the exact positions of the nuclei that give rise to a signal. Thus it is possible to reconstruct images of organs inside the human body, for diagnostic purposes. It is also possible to monitor the blood flow[76] in vivo, and by the molecular imaging MRI one can obtain information about the metabolic processes[77] and different pathologies that interfere with the normal physiology.

There are also more general applications that are somehow detached from the scientific world. For example in cultural heritage[78] NMR contributes to the conservation of important paintings or statues by monitoring the penetration of water molecules in the inner layers of the object or by examining the under-surface morphology. This information is crucial for the conservation of important historical pieces. Furthermore, NMR is exploited in the food industry where it helps to identify the origin of a product, like wine[79], or the control of the food quality[80].

On the other hand, electron paramagnetic resonance (EPR)[81] is a non invasive spectroscopic technique that contains the same basic physical principles as NMR being based on the magnetic resonance phenomena. The EPR signals are the response of free electrons to the external irradiation excitation in the region of microwaves when they are placed in a magnetic field. It is a highly sensitive technique with respect to NMR since it takes advantage of the fact that the gyromagnetic ratio of the electron is three orders of magnitude higher than the nuclear one. EPR studies find various applications in an extended region of areas like physics[82], chemistry[83], medicine[84], biology[85], pharmacology[86], cosmetology[87] and cultural heritage[88]. By the signal of free electrons or paramagnetic ions in organic and inorganic samples in the solid, liquid, or gaseous state we obtain information for the physical and chemical properties of the mater.

With EPR in physics, for example, we obtain information about the magnetic behaviour of the materials (magnetic susceptibility) or we can study the conduction electrons in semiconductors and conductors and the detection of paramagnetic defects in crystals like color ions. In chemistry EPR is useful in the catalysis, the kinetics of the radical reactions, in polymerisation reaction and oxidation and reduction processes while in medicine and biology it can be used in the examination of the living tissues, blood cells, enzyme reactions, oximetry and the photosynthesis process. Apart from the numerous scientific applications EPR has also contributed in the industrial research like the detection of defects in diamonds and optical fibers and the degradation of paint, polymers and metals from natural sources like light and humidity or by irradiation.[89]

2.1 Classical description of NMR

In the classical description, the effect of a static magnetic field $\overrightarrow{H_0}$ on a magnetic dipole is to induce a precession of the latter around the direction of the field. Supposing that the external field is applied along the $\widehat{z}$ axes we have the precessional motion shown in figure (2.1a). The frequency of the precession is known as Larmor Frequency and is given by

$$\omega_0 = \gamma H_0 \tag{2.1}$$

where γ is the nuclear gyromagnetic ratio. The component of the magnetization m on the xy plane rotates at the Larmor frequency while the $\widehat{z}$ component is constant.

The aim is to follow the time evolution of the magnetization in order to investigate the interactions with other spin systems like nuclei and electrons or, in case of quadrupole nuclei with the electric field gradients determined by the electronic charge distribution. To simplify the description it is convenient to move to a reference frame S' rotating at the Larmor frequency, in order to cancel the effect of the precessional motion around the static field (figure 2.1b).

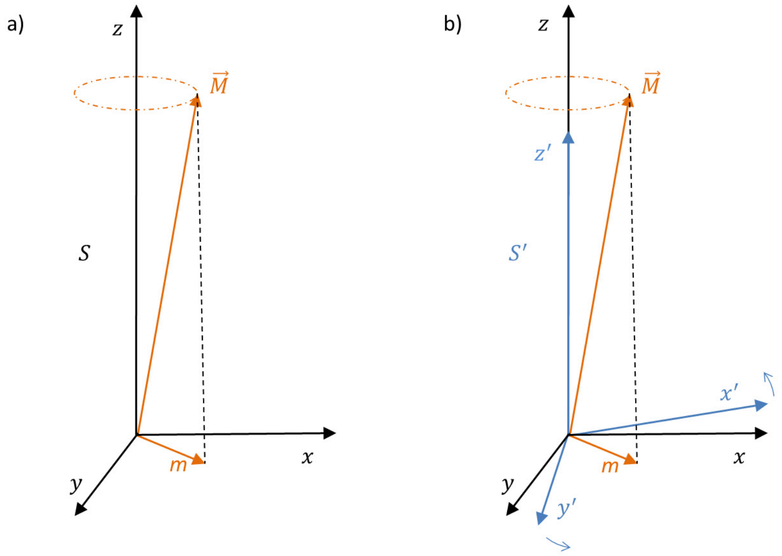

Figure 2.1: Precession of the magnetization around the axis of the magnetic field $\widehat{z}$ in a) the static laboratory frame S and in b) the rotating frame S'.

In the initial, laboratory frame S, the time evolution of the different components of the magnetization as given by

$$\begin{cases} \frac{dM_z(t)}{dt} = 0 \\ \frac{dM_x(t)}{dt} = \gamma H_0 M_y \\ \frac{dM_y(t)}{dt} = \gamma H_0 M_x \end{cases} \Rightarrow \begin{cases} M_z(t) = \text{const.} \\ M_x(t) = Mcos(\omega_0 t) \\ M_y(t) = -Msin(\omega_0 t) \end{cases} \tag{2.2}$$

while in the rotating frame for the time evolution of the magnetization we have

$$\frac{dM_z(0)}{dt} = \gamma M \times \left(H_0 + \frac{\Omega}{\gamma}\right) \tag{2.3}$$

where Ω is the rotational frequency of the frame S'. If we choose $\Omega = -\omega_0$, with $\omega_0 = \gamma H_0$ (equal to the Larmor Frequency), so that the resonance condition holds, the magnetization will remain constant along $\widehat{z}$, without any rotational motion in this frame. Then, by applying a small magnetic field $H_1 = \frac{\omega_1}{\gamma}$ perpendicular to H_0 (90° or $\frac{\pi}{2}$ pulse) the magnetization will start precessing around an effective magnetic field $H_e = \left(H_0 + \frac{\Omega}{\gamma}\right)\widehat{z}' + H_1\widehat{x}'$ (figure 2.2). In the case where $|\Omega| = \gamma H_0$, the magnetization rotates entirely around the axes $\widehat{x}'$.

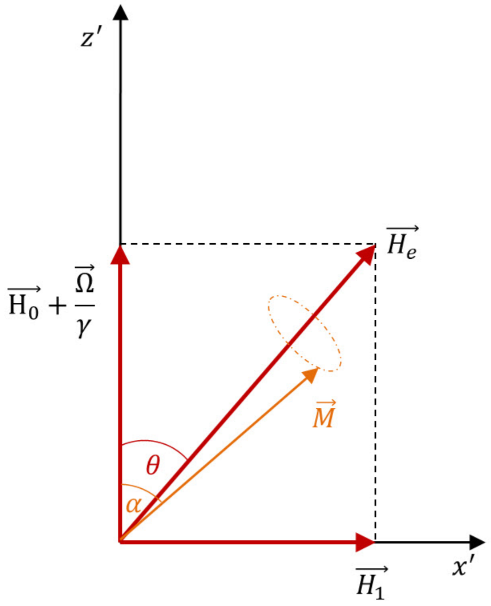

Figure 2.2: The magnetization precesses around an effective magnetic field produced by the application of the field H_1, as it is detected in the rotating frame.

The angle between the $\widehat{z}$ axes and the time evolution of the magnetization α, seen in the above figure, is given by the equation

$$cos(\alpha(t)) = 1 - 2sin^2\left(\frac{\omega_1 t}{2}\right) \quad (2.4)$$

In NMR experiments the H_1 fields are radiowaves which have been produced by a coil that is also used for the signal readout. Once we satisfy the resonance condition, even if the RF field is small $H_1 \ll H_0$ it is equally effective.

2.2 Quantum mechanical description of NMR

Stable isotopic nuclei that contain a non-zero total magnetic moment interact with a static applied magnetic field. The nuclear energy levels interact with the magnetic field through the Zeeman interaction giving rise to the Zeeman energy split. The interaction Hamiltonian is

$$\mathcal{H} = -\gamma\hbar I_z H_0 \quad (2.5)$$

since we suppose that the magnetic field is applied along $\widehat{z}$ direction and the energy eigenvalues are

$$E_{m_I} = -\gamma\hbar H_0 m_I \quad (2.6)$$

In figure (2.3) the effect of the Zeeman split is shown for a spin $I = \frac{1}{2}$

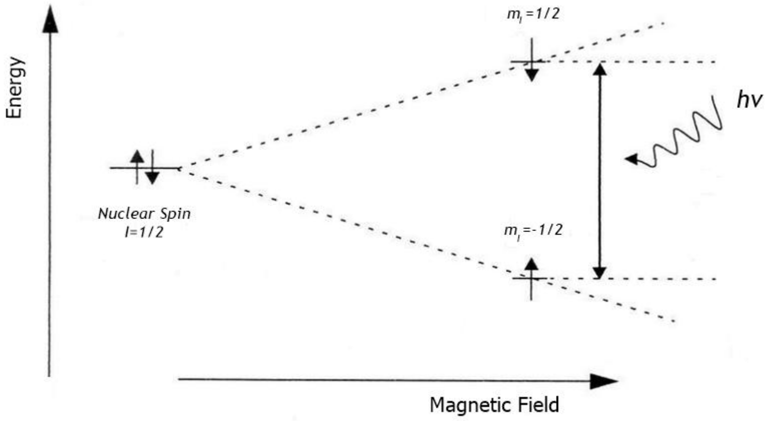

Figure 2.3: Zeeman split of the nuclear energy levels in the presence of magnetic field for a system with spin $\frac{1}{2}$.

Magnetic dipole transitions between the nuclear energy levels can be induced by radiowave irradiation at the resonance frequency, namely $\omega_0 = \gamma H_0$. This is the quantum analogue of the classical case where we had used the RF field H_1 for the excitation of the system and as a result the flip of the magnetization in the plane.

The expectation value of the z component of the nuclear spin for a two energy level system is given by the equation

$$\langle I_z \rangle = -\frac{1}{2}(p_+ - p_-) \tag{2.7}$$

where $p_\pm$ is the occupation probability for the two energy levels. Since we have a two level system the relation $p_+ + p_- = 1$ holds and for the probability we have

$$p_-(t) = \frac{1}{2}\left(1 - 2\langle I_z \rangle\right) \tag{2.8}$$

Since I_z is the component along $\widehat{z}$ of the nuclear spin it is determined by the cosine of the angle α (eq. 2.4). Under this assumption we have for the probability that the system passes by the two possible configurations

$$p(t) = \sin^2\left(\frac{\gamma H_1 t}{2}\right) \tag{2.9}$$

which corresponds to the well-known Rabi equation.

Now, since the systems that we shall consider are formed by a macroscopic ensemble of nuclear spins we need to consider a statistical ensemble of magnetic moments and determine the statistical average of the spin components. The expectation value of the $\widehat{z}$ component of spin is

$$\langle \overline{I_z} \rangle = \langle \psi | I_z | \psi \rangle = \sum_{m,n} \overline{c_m^* c_n} \langle m | I_z | n \rangle = \sum_{m,n} \overline{c_{mn}}^2 \langle m | I_z | n \rangle \tag{2.10}$$

where $|\psi\rangle = \sum_n c_n |n\rangle$ is the system's wavefunction, described by the linear combination of the eigenstates $|n\rangle$ with coefficient c_n. The horizontal bar over the coefficients indicates the statistical average. The statistical occupation probability can be computed by resorting to the Boltzmann statistics and by resorting to the random phase approximation so that $c_{mn} \neq 0$ only for $m = n$, so we have,

$$\overline{|c_{nn}|}^2 = \frac{e^{-\beta E_n}}{\mathcal{Z}} \tag{2.11}$$

where $\mathcal{Z}$ is the partition function. Thus the total polarization in thermal equilibrium will be given by the formula

$$P_n = \frac{\langle I_z \rangle}{I} = \frac{\sum_{m_I} m_I e^{-\left(\frac{E m_I}{k_B T}\right)}}{I \sum_{m_I} e^{-\left(\frac{E m_I}{k_B T}\right)}} \tag{2.12}$$

with $\mathcal{Z} = \sum_{m_I} e^{-\left(\frac{E m_I}{k_B T}\right)}$.In particular, for $I = \frac{1}{2}$, which is the case we shall consider, we have

$$P_n = \tanh\left(\frac{\gamma_n \hbar H_0}{2 k_B T}\right) \tag{2.13}$$

that is the equation reported in section (3.1). Finally the total magnetization is given by

$$M = \mu N P_n = \mu N \tanh\left(\frac{\gamma_n \hbar H_0}{2k_B T}\right), \tag{2.14}$$

which in the high temperature limit $k_B T \gg \gamma_n \hbar H_0$ corresponds to Curie law. It can also be seen from the last equation that at high magnetic fields and low temperatures we have higher magnetization.

2.3 Bloch equations

One of the first attempts to describe phenomenologically the time evolution of the nuclear magnetization in real systems was provided by the Bloch equations (2.15). These equations include the interactions of the nuclei with the electrons, the other nuclei, the presence of ions and the lattice vibrations, through two characteristic relaxation times T_1 and T_2.

$$\begin{cases} \frac{dM_z}{dt} = \gamma(M \times H_0)_z + \frac{M_0 - M_z}{T_1} \\ \frac{dM_{x,y}}{dt} = \gamma(M \times H_0)_{x,y} - \frac{M_{x,y}}{T_2} \end{cases} \tag{2.15}$$

The first equation describes the relaxation of magnetization along the $\widehat{z}$ axes and contains the T_1 relaxation time that is also called as spin-lattice relaxation time, while the second equation describes the relaxation in the xy plane and contains the T_2 relaxation time or spin-spin relaxation time. In NMR experiments one can measure separately these two relaxation times by using different pulse sequences.

The time evolution of the in plane components of the nuclear magnetization, i.e. the NMR signal, can be derived from the solution of the Bloch Equations by considering a small excitation rotating field H_1 [66] perpendicular to the external static magnetic field H_0. After the application of this small field the effective magnetic field will be

$$H_{eff} = H_1(\widehat{x}\cos(\omega t) - \widehat{y}\sin(\omega t)) + H_0\widehat{z} \tag{2.16}$$

By substituting the H_{eff} to the Bloch equations and by assuming that

$$M_{x,y} \ll M_z \cong M_0 \tag{2.17}$$

we have that

$$\begin{cases} \frac{dM_z}{dt} = 0 \\ \frac{dM_x}{dt} = \omega_0 M_y + \omega_1 M_z \sin(t) - \frac{M_x}{T_2} \\ \frac{dM_y}{dt} = -\omega_0 M_x + \omega_1 M_z \cos(t) - \frac{M_y}{T_2} \end{cases} \tag{2.18}$$

For the small excitation field holds the relation $\gamma H_1 \ll \frac{1}{\sqrt{T_1 T_2}}$ thus the product $\omega_1 \cdot M_{x,y}$ tends to zero. So, if we search solutions of the form

$$\begin{aligned} M_x &= m\cos(\omega t + \phi) \\ M_y &= -m\sin(\omega t + \phi) \end{aligned} \tag{2.19}$$

after some calculations, we have for the transversal component of the magnetization that

$$m = \frac{\omega_1 M_0 T_2^2}{\sqrt{1 + (\omega_0 - \omega)^2 T_2^2}} \tag{2.20}$$

The x and y components of the magnetization are tied to the nuclear spin susceptibility. More specifically, the complex susceptibility is equal to $\chi(\omega) = \chi' + i\chi''$ where, for the real part of the signal we have

$$\chi'(\omega) = \frac{M_0}{H_0}\frac{\omega_0(\omega_0 - \omega)T_2^2}{1 + (\omega_0 - \omega)^2 T_2^2} \tag{2.21}$$

while for the imaginary part we have

$$\chi''(\omega) = \frac{M_0}{H_0}\frac{\omega_0 T_2}{1 + (\omega_0 - \omega)^2 T_2^2} \tag{2.22}$$

The real part of the susceptibility shows the dispersion while the imaginary part is proportional to the power absorption by the NMR coil. Thus the imaginary part of the NMR signal is represented by a Lorentzian function. The width of the line shows the distribution of the nuclear resonance frequencies and indicates the spin-spin relaxation rate $\frac{1}{T_2}$. The more homogeneous is the systems the narrower is the line. The intensity of the curve for each frequency gives us the fractions of the nuclei that are resonant at that frequency, corresponding to the NMR spectrum.

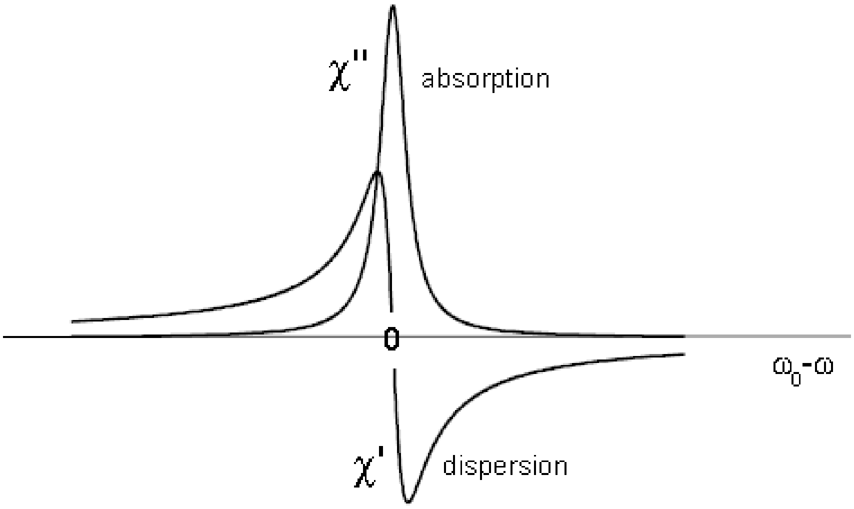

Figure 2.4: Real and imaginary part of the magnetic susceptibility. The imaginary part represents the NMR signal.

2.4 Spin-Lattice relaxation time T_1

The first of the Bloch equations evidences that T_1 process determines the return of the magnetization from the xy plane to the $\widehat{z}$ direction. This means that when the polarization is on the plane, the population difference is zero since there is no component along $\widehat{z}$. When we stop irradiating the system the magnetization returns to its equilibrium value and accordingly also do the populations of the nuclear energy levels. So, from the first of the equations (2.15) we have that

$$M_z(t) = M_z(0)\left(1 - e^{\frac{-t}{T_1}}\right) \tag{2.23}$$

The system relaxes back to the thermal equilibrium by exchanging energy with the surrounding lattice at a rate which is determined by the transition probabilities among the energy levels.

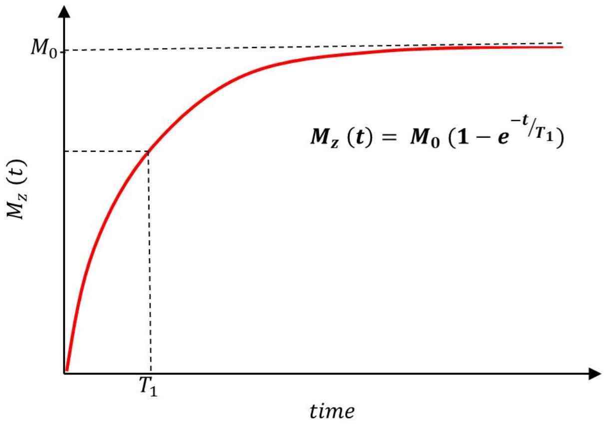

Figure 2.5: Time evolution of the magnetisation components recovery along the $\widehat{z}$ axis. The spin-lattice relaxation time T_1 indicates a magnetization recovery equal to 66% and M_0 is the infinite time (saturation) magnetization.

The time evolution of the population of the energy levels and the transition probabilities is determined by the master equations

$$\frac{dN_m}{dt} = \sum_{n \neq m} (N_n W_{nm} - N_m W_{mn}) \tag{2.24}$$

where $N_{n,m}$ are the populations of the Zeeman energy states $E_{n,m}$ and W_{nm} are the transition probabilities per unit time between the two energy levels. If we consider a nucleus with $I = \frac{1}{2}$ and $m_I = \pm\frac{1}{2}$, one has

$$\frac{1}{T_1} = W_{\pm} + W_{\mp} \tag{2.25}$$

and since $M_z(t) \propto N_+(t) - N_-(0)$, one derives the equation (2.23).

To establish a relationship between T_1 and the local dynamics we first need to calculate the transition probability determined by the perturbation of the system. Considering the time dependent perturbation Hamiltonian

$$H_p(t) = -\gamma\hbar \overrightarrow{I} \cdot \overrightarrow{h}(t) \tag{2.26}$$

where $\overrightarrow{h(t)}$ is a fluctuating local field, we have for the probability that the system passes from $m_I = +\frac{1}{2}$ to $m_I = -\frac{1}{2}$ after a certain time t

$$\begin{aligned}
P_{+-}(t) &= \frac{1}{\hbar^2}\left|\int_0^t e^{\frac{-iE_+t'}{\hbar}}\langle +|H_p(t')|-\rangle e^{\frac{iE_-t'}{\hbar}}dt'\right|^2 \Rightarrow \\
P_{+-}(t) &= \frac{1}{\hbar^2}\left|\int_0^t \langle +|H_p(t')|-\rangle e^{i\omega_0 t'}dt'\right|^2 \Rightarrow \\
P_{+-}(t) &= \frac{1}{\hbar^2}\int_0^t dt'\int_0^t \langle +|H_p(t'')|-\rangle\langle -|H_p(t')|+\rangle e^{i\omega_0(t''-t')}dt''\,.
\end{aligned} \tag{2.27}$$

Now we introduce the correlation function

$$G(t''-t') = \langle +|H_p(t'')|-\rangle\langle -|H_p(t')|+\rangle \tag{2.28}$$

where the average is over the lattice ensemble. So, the transition probability over time is equal to

$$W_{+-} = \frac{P_{+-}(t)}{t} = \frac{1}{\hbar^2}\frac{1}{t}\int_0^t dt'\int_0^t G(t''-t')e^{i\omega_0(t''-t')}dt'' \tag{2.29}$$

by introducing the correlation time $\tau = t'' - t'$ and considering that the correlation time is much smaller than the time t of the measurement we have for the spin-lattice relaxation rate

$$\frac{1}{T_1} = \frac{2}{\hbar^2}\int_{-\infty}^{\infty} G(\tau)e^{i\omega_0\tau}d\tau \tag{2.30}$$

that is nothing more than the Fourier transform at the Larmor frequency of the correlation function of the system that also involves the energy conservation by taking into consideration that only the fluctuations at an energy equal to $\hbar\omega_0$ contribute to the transitions. The expansion of the scalar product in the perturbative Hamiltonian gives as

$$\begin{aligned}
H_p(t) &= -\gamma\hbar(I_xh_x + I_yh_y + I_zh_z) \Rightarrow \\
H_p(t) &= \frac{-\gamma\hbar}{2}(2I_zh_z - I_+h_- + I_-h_+)
\end{aligned} \tag{2.31}$$

where $I_\pm = I_x + iI_y$ and $h_\pm = h_x + ih_y$. The first term commutes with the Hamiltonian giving no transitions while the components I_x and I_y contribute to the transitions satisfying in this way the magnetic dipole selection rules. So we finally have that

$$\frac{1}{T_1} = \frac{\gamma^2}{2} \int_{-\infty}^{\infty} \langle h_+(\tau) h_-(\tau) \rangle e^{i\omega_0 \tau} d\tau. \tag{2.32}$$

where $\langle h_+(\tau) h_-(\tau) \rangle$ is the correlation function of the fluctuating transverse local field components.

Now, assuming that this correlation function decays exponentially, as it is often the case, the Fourier transform of an exponential is a Lorentzian, and if we have isotropic transverse fluctuations, namely

$$\langle h_+(\tau) h_-(0) \rangle = \langle \Delta h_\perp^2 \rangle e^{\frac{-\tau}{\tau_c}} \tag{2.33}$$

where τ_c is the characteristic correlation time of the fluctuations and

$$\langle h_x(\tau) h_x(0) \rangle = \langle h_y(\tau) h_y(0) \rangle \tag{2.34}$$

we have for the spin-lattice relaxation that

$$\frac{1}{T_1} = \frac{\gamma^2}{2} \langle \Delta h_\perp^2 \rangle \frac{2\tau_c}{1 + \omega_0^2 \tau_c^2} \tag{2.35}$$

that it is also known as the Bloembergen, Purcell and Pounds (BPP) formula[90].

In DNP experiments the fluctuating local field $\overrightarrow{h(t)}$ that perturbs the system and forces the nuclei to relax is produced by the presence of the electrons under the form of radicals and by other nuclear spins. The main interactions between electrons and nuclei are the transferred hyperfine interaction and the magnetic dipole-dipole interaction[91]. Both can be represented by the general Hamiltonian

$$\mathcal{H} = \boldsymbol{\alpha} \cdot \overrightarrow{I} \cdot \overrightarrow{S} \tag{2.36}$$

where α is a tensor. In the simplest case the electron nucleus interaction is governed by the dipole-dipole one and the tensor components are given by

$$\alpha_{ij} = |\gamma_I \gamma_S| \hbar^2 \frac{\delta_{ij} - 3\widehat{r}_i \cdot \widehat{r}_j}{r^3} \tag{2.37}$$

with $\overrightarrow{r}$ being the vector connecting the electron and the nucleus. In the case where we have to consider also the transferred hyperfine interaction the coupling is strongly dependent on the electron wavefunction overlap. The general Hamiltonian can also be written in the form of

$$\mathcal{H} = -\gamma_I \hbar \overrightarrow{I} \cdot \overrightarrow{h} \tag{2.38}$$

where $\overrightarrow{h}$ is the fluctuating field produced by the electron spin that perturbs the system and is equal to

$$\overrightarrow{h} = -\gamma_S \hbar \boldsymbol{\alpha} \cdot \overrightarrow{S} \tag{2.39}$$

These random fluctuations depend either on the time dependence of the tensor α that describes the relative motion of the nuclei and the electrons or by the time evolution of the electron spin, that is its relaxation time.

By introducing this fluctuating field into the equation (2.39), considering a magnetic dipolar coupling, we have that

$$\frac{1}{T_1} = \frac{9}{2}\gamma_S \gamma_I \hbar^2 \frac{\sin^2(\theta)\sin^2(\theta)}{r^6} \int_{-\infty}^{\infty} \langle S_z(0) S_z(t) \rangle e^{-i\omega_0 t} dt \tag{2.40}$$

with θ the angle between the direction of the magnetic field and the vector r. At low temperature and high fields it is wise to consider the fluctuation of spin around the average value which in the isotropic case becomes

$$\langle (S_z(0) - S_0)(S_z(t) - S_0) \rangle = \frac{1}{3} S(S+1) e^{-\frac{t}{T_{2e}}} \tag{2.41}$$

and considering the population of the Zeeman energy levels (eq. 2.7), for spin $S = \frac{1}{2}$ we have

$$\frac{1}{3} S(S+1) e^{-\frac{t}{T_{2e}}} = \frac{1}{4}(1 - P_0^2) e^{-\frac{t}{T_{2e}}} \tag{2.42}$$

with T_{2e} the electron spin-spin relaxation time and P_0 the thermal polarization. Finally, for the nuclear relaxation rate we have

$$\frac{1}{T_1} \cong \left(\frac{H_e}{H_0}\right)^2 \frac{1}{T_{2e}} (1 - P_0^2) \tag{2.43}$$

with H_0 the externally applied magnetic field and H_e the effective field that is produced by the electron. So it can be seen that the nuclear relaxation rate depends on the electron thermal polarization. In specific systems though, one can consider that the decay of the spin components $S_{x,y}$ determined by the electron spin-lattice relaxation time T_{1e} is some times more effective.

Temperature plays an important role in the dynamics of the systems. More specifically, molecules in a sample can move or rotate faster at higher temperatures or being almost frozen at low temperatures. Since with NMR experiments we monitor the behaviour of the nuclei in these molecules, it can be easily seen that the relative motion of the nuclei affects also the NMR signal and relaxation times. In particular we can examine three different regimes for T_1:

A. Fast Motions

Typically at high temperatures, the fluctuation frequency is much larger than the Larmor Frequency

$$\omega_0 \tau_c \ll 1 \tag{2.44}$$

and as a consequence the BPP formula becomes

$$\frac{1}{T_1} = \gamma^2 \langle \Delta h_\perp^2 \rangle \tau_c. \tag{2.45}$$

B. Intermediate Motions

In the case of intermediate temperatures the fluctuation frequency becomes almost equal to the Larmor frequency

$$\omega_0 \tau_c \cong 1 \tag{2.46}$$

and for the BPP formula we have

$$\frac{1}{T_1} = \frac{\gamma^2}{2} \langle \Delta h_\perp^2 \rangle \frac{1}{\omega_0}. \tag{2.47}$$

This means practically that the fluctuations have the exact energy to induce the transitions. In this regime the temperature dependence of the relaxation rate $\frac{1}{T_1}$ displays a peak indicating that the frequency of the motions is equal to the Larmor frequency and in this situation the transition probability reaches its maximum.

C. Slow Motions

Decreasing even more the temperature the fluctuation frequency becomes much smaller that the Larmor frequency

$$\omega_0 \tau_c \gg 1 \tag{2.48}$$

and for the BPP formula we have

$$\frac{1}{T_1} = \gamma^2 \langle \Delta h_\perp^2 \rangle \frac{1}{\omega_0^2 \tau_c}. \tag{2.49}$$

2.5 Spin-Spin relaxation T_2

Besides the return of the magnetization along the $\widehat{z}$ axes we have also the decay of the transverse components. The time evolution of the transverse components is described by the second of the Bloch equations (2.15) from which we can derive

$$M_{x,y}(t) = M_{x,y}(0) e^{\frac{-t}{T_2}} \tag{2.50}$$

In principle, it is different than the T_1 and it does not depend on the energy exchange with the lattice as the spin-lattice relaxation. This relaxation mechanism depends mainly on the interaction with the other spin species that are located in the proximity of the nucleus under investigation but also to the local magnetic field and the presence of electric field gradient; the last one is not present in the case that the nuclear spin is $I = \frac{1}{2}$.

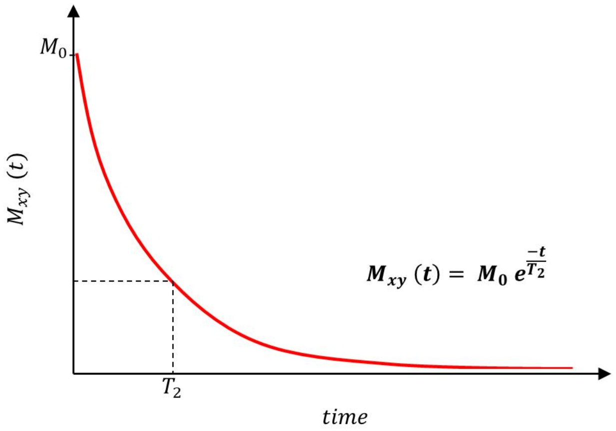

Figure 2.6: Time evolution of the magnetisation components decay in the xy plane. The spin-spin relaxation time T_2 indicates a magnetization equal to 33% and M_0 is the magnetization at $t = 0$.

As mentioned before the main interaction responsible for the evolution of the magnetization in-plane is the nuclear dipole-dipole interaction. So, in the simplest case the system is described by the Hamiltonian

$$\mathcal{H}_n = -\gamma\hbar H_0 \sum_j I_z^j + \sum_{j<k} \frac{\hbar^2\gamma^2}{r^3}\left[\overrightarrow{I}^j\overrightarrow{I}^k - 3\frac{(I^j r_{jk})(I^k r_{jk})}{r_{jk}^2}\right] \tag{2.51}$$

where the first term indicates the Zeeman interaction and the second the nuclear dipole interaction. The dipole interaction term can be written also in the form

$$\mathcal{H}_d = \sum_{j<k} \frac{\hbar^2\gamma^2}{r^3}(A + B + C + D + E + F)_{jk} \tag{2.52}$$

which is also known also as the dipole alphabet. We can divide the above terms into three groups; the first one contains A and B and describes the interaction without any energy level transition since they both commute with the principal Zeeman Hamiltonian H_z, namely

$$[A, \mathcal{H}_z] = 0 \tag{2.53}$$

and

$$[B, \mathcal{H}_z] = 0 \tag{2.54}$$

while the other two groups describe transitions between the energy levels with $\Delta m = \pm 1$ (C and D) and $\Delta m = \pm 2$ (E and F) respectively. These terms are given by the equations (2.55) in spherical coordinates.

$$\begin{aligned}
A &= I_i^z I_j^z (1 - 3\cos^2\theta_{ij}) \\
B &= -\frac{1}{4}(I_i^+ I_j^- - I_i^- I_j^+)(1 - 3\cos^2\theta_{ij}) \\
C &= -\frac{3}{2}(I_i^+ I_j^z - I_i I_j^+)(\cos\theta_{ij}\sin\theta_{ij})e^{-i\phi} \\
D &= -\frac{3}{2}(I_i^- I_j^z - I_i I_j^-)(\cos\theta_{ij}\sin\theta_{ij})e^{i\phi} \\
E &= -\frac{3}{4} I_i^+ I_j^+ \sin^2\theta_{ij} e^{-2i\phi} \\
F &= -\frac{3}{4} I_i^- I_j^- \sin^2\theta_{ij} e^{2i\phi}
\end{aligned} \tag{2.55}$$

We consider that the dipole interaction, giving rise to magnetic fields of the order of the Gauss, is a perturbation of the Zeeman interaction and since it is much weaker only the terms of the first group can be considered to a first approximation. So we have for the correlation function to which the NMR signal is proportional that

$$\begin{aligned}
G(t) &= \langle M_x(t) M_x(0) \rangle \Rightarrow \\
G(t) &= Tr\left\{ e^{-\frac{iH_d^{'}t}{\hbar}} M_x e^{\frac{iH_d^{'}t}{\hbar}} M_x \right\} \xRightarrow{\frac{\gamma^2\hbar t}{r^3}<1} \\
G(t) &= G(0)\left[M_0 + M_2\frac{t^2}{2!} + M_4\frac{t^4}{4!} + ... \right]
\end{aligned} \tag{2.56}$$

where the H_d' is the dipole interaction Hamiltonian considering only the first two terms, the first moment (M_0) indicates the mean value of the distribution, the second moment (M_2) indicates the variance of the mean value and the third moment (M_4) represents the skewness of the distribution. In the study of spin-spin relaxation we are interested in the second moment since we are interested in the width of the distribution in order to recover the relaxation rate $\frac{1}{T_2}$. The signal can be found by the Fourier Transform (FT) of the correlation function and the T_2 is proportional to the second moment that is given in polar coordinates by

$$M_2 = \gamma^4\hbar^2 \frac{I(I+1)}{3} \sum_k \left(\frac{3}{2} \frac{1 - cos^2(\theta_k)}{r_k^3} \right)^2 . \tag{2.57}$$

It is worth to mention that by T_2 measurements, since it is proportional to the second moment, one can retrieve the distance between the interacting nuclei and thus reconstruct the geometry of the sample structure.

2.6 Motions effect on the NMR spectrum and motional narrowing

Now, by considering a time dependent perturbation which can be described by a time dependent resonance frequency, yielding a shift in the resonance frequency of the i^{th} nucleus $\Delta\omega_i(t)$

$$\mathcal{H}_d = -\hbar \sum_i \Delta\omega_i(t) I_z^i \tag{2.58}$$

where the mean value of the distribution of resonance frequency $\Delta\omega_i(t)$ can be given by

$$\langle \Delta\omega_i(t) \rangle = \frac{1}{t} \int_0^t \Delta\omega_i(t') dt'. \tag{2.59}$$

Assuming a stationary Gaussian distribution for the frequency, namely

$$P\left(\Delta\omega(t)\right) = \frac{1}{\sqrt{2\pi M_2}} e^{-\frac{\Delta\omega^2(t)}{2M_2}}. \tag{2.60}$$

By introducing the correlation function for the frequency fluctuations with $M_2 = \langle \Delta\omega^2(t) \rangle$ the second moment of the frequency distribution we have

$$G^{'(\tau)} = \langle \Delta\omega(t+\tau)\Delta\omega(t) \rangle = \langle \Delta\omega^2 \rangle G(\tau) \tag{2.61}$$

and for the NMR signal one can write

$$\begin{aligned} S(t) &= e^{-i\int_0^t \Delta\omega_i(t')dt'} \\ S(t) &= \int P\left(\Delta\omega(t'')\right) e^{-i\int_0^t \Delta\omega_i(t')dt'} dt'' \Rightarrow \\ S(t) &= S(0) e^{-M_2 \int_0^t (t-\tau) G(\tau) d\tau} \end{aligned} \tag{2.62}$$

The signal is also called as signal of free induction decay (FID).

A. Slow Motions

In this regime the correlation time is much longer than the time for the signal acquisition

$$t \ll \tau_c. \tag{2.63}$$

Hence, during the signal acquisition, the system hasn't evolved yet and the correlation function can be approximated as $G(t) \cong G(0) = 1$. The signal then becomes

$$S(t) = S(0) e^{-\frac{-M_2 t^2}{2}} \tag{2.64}$$

which is a Gaussian. From the FT of the signal we obtain the NMR spectra that it is still a Gaussian of the form

$$f(\omega) \propto e^{\frac{-\omega^2}{2M_2}}. \tag{2.65}$$

This result is something we expect because we started the analysis with the assumption that the distribution is a Gaussian and we assumed also that the system hasn't evolved until the time of the signal acquisition. From the behaviour of the spectrum we can recover the second moment and then from the equation (2.57) we can retrieve all the other values in which we are interested.

B. Fast Motions

In this regime the acquisition time is much longer that the correlation time

$$t \gg \tau_c \tag{2.66}$$

and the system has fully evolved during the acquisition time. By recalling that the correlation time is defined as

$$\tau_c = \int_0^\infty G(\tau) d\tau. \tag{2.67}$$

By neglecting the time τ in the last of the equations (2.62), since it is much smaller than the time t, we have

$$\begin{aligned} S(t) &= S(0)e^{-M_2 t \tau_c} \Rightarrow \\ S(t) &= S(0)e^{\frac{-t}{T_2'}} \end{aligned} \tag{2.68}$$

where $\frac{1}{T_2'} = M_2\tau_c$. The form of the signal is an exponential decay and from the FT we obtain the NMR spectrum which is a Lorentzian of the form

$$f(\omega) = \frac{T_2'}{1+\omega^2 T_2'^2}. \tag{2.69}$$

The transverse relaxation rate $\frac{1}{T_2}$ can be found from the Full Width at Half Maximum (FWHM) of the Lorentzian curve.

With respect to the previous case of the slow motions, when the motions become faster, the NMR spectrum becomes narrower and transforms from a Gaussian to a Lorentzian. By increasing the frequency of the motions, the width of the spectrum becomes even smaller. This effect is called motional narrowing[92] and it is an effect mainly powered by the relative motion of the nuclei.

2.7 NMR pulse sequencies: the FID signal

Free induction decay (FID) consists a very straightforward method of NMR signal detection. Here, a single RF pulse of frequency comparable to the Larmor frequency of the nuclear spins is applied across $\widehat{x}$ or $\widehat{y}$ direction in order to bring the magnetization onto the plane xy. Finally, after monitoring the time evolution of the magnetization component along the $\widehat{z}$ axis, we can apply Fourier transform in order to acquire the frequency spectrum of the respective NMR signal. In this way we can measure the spin-lattice relaxation T_1.

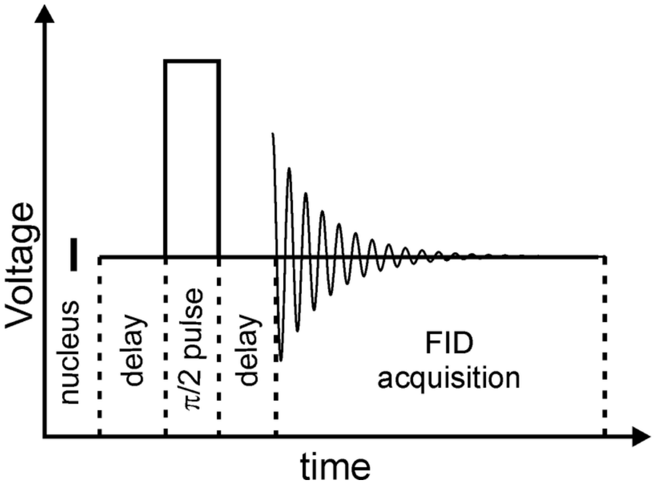

Figure 2.7: A common FID sequence consists of an excitation pulse ($\frac{\pi}{2}$) that brings all the magnetisation components in the xy plane, perpendicular to the externally applied magnetic field. The time evolution of the magnetisation is recorded either in plane ($\frac{1}{T_2}$) or in the z axis ($\frac{1}{T_1}$). Figure created by *R. D. Majumdar.*

We can generally say that FID is the damped oscillation close to the nuclear resonance when the non-equilibrium magnetization has been brought into the transverse xy plane decaying over a time T_2. Despite the fact the T_2 time seems very easy to obtain, we have to take into account that the applied magnetic field presents inhomogeneities as well as the nuclear diffusion affects critically the NMR spectrum. In order to tackle this, someone can use either the spin echo sequence or other multi-pulse sequences, such as the Carr-Purcell sequence[93].

2.7.1 The Spin Echo

In order to measure the spin lattice relaxation time T_2 we need to construct the magnetization recovery curve that is to map the time evolution of the magnetization. This can be done by an NMR Spin Echo sequence.

A spin echo is generated by two successive RF pulses[94]. The first one is a $\frac{\pi}{2}$ pulse along $\widehat{x}$ direction that brings the magnetization on plane. The second pulse is usually a π pulse along the $\widehat{y}$ direction that refocuses the spins that are now dephased due to the dipolar interactions of the nuclei and/or the inhomogeneity of the static applied field. The exact process can be seen better step by step in Figure 2.8.

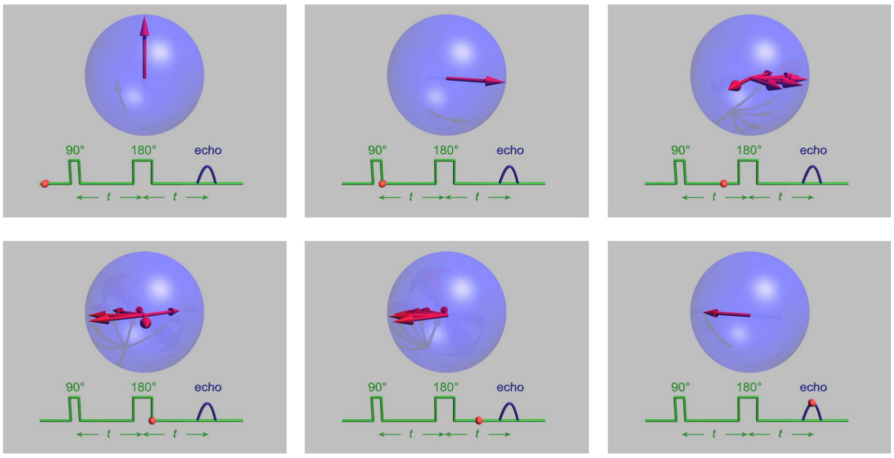

Figure 2.8: Representation of the Spin Echo sequence. A $\frac{\pi}{2}$ pulse excites the system and a second π pulse flips the on-plane magnetization components around $\widehat{x}$ axes. The components are gathered together after some time (Time Echo) giving the signal. Figure created by *G. W. Morley*.

At time zero all the nuclear spins are oriented along the $\widehat{z}$ direction. When the $\frac{\pi}{2}$ pulse is applied all the components of the spin will be brought onto the xy plane. Then, during the time between the first and the second pulse t, the spin components will dephase because the local microscopic fields may differ slightly. Some will rotate at higher frequencies while the rest at lower frequencies. The second pulse will flip the entire system by 180°. The distribution of the local fields will remain the same but the magnetic components will rotate obtaining opposite orientation; the faster ones will take the place of the slower ones and vice versa. In time 2t, or as it is called Time Echo (TE), all the components will catch up each other (rephased) giving rise to the echo NMR signal.

An advantage of the spin echo is the purification of the final signal from the inhomogeneous static magnetic field that results in a distribution of resonance frequencies and a broadening of the NMR signal, the coil ringing which is mechanical oscillation produced during the creation of the RF pulses and of course the so called dead time which is the finite time that the system need to start the signal recording.

2.8 Fundamental principles of EPR spectroscopy

As mentioned before, EPR spectroscopy shares the same fundamental physical principles with NMR spectroscopy. Both techniques involve the study of the interaction between electromagnetic radiation and magnetic moments.

In the case of EPR these magnetic moments originate from the unpaired electrons and the electromagnetic frequencies lie in the microwave regime $(1 - 100\,GHz)$. In fact, depending on the frequency value of the irradiation, we can distinguish four basic types of EPR spectrometers:

- 2-3 GHz (S-band)
- 9-10 GHz (X-band)
- 32-35 GHz (Q-band)
- 90-95 GHz (W-band)

In figure 2.9 we can see the energy diagram of a particle with spin $\frac{1}{2}$ placed in a magnetic field. In the absence of a magnetic field the energy states associated with $m_S = \pm\dfrac{1}{2}$ are degenerate and the magnetic moment of the particle is oriented randomly.

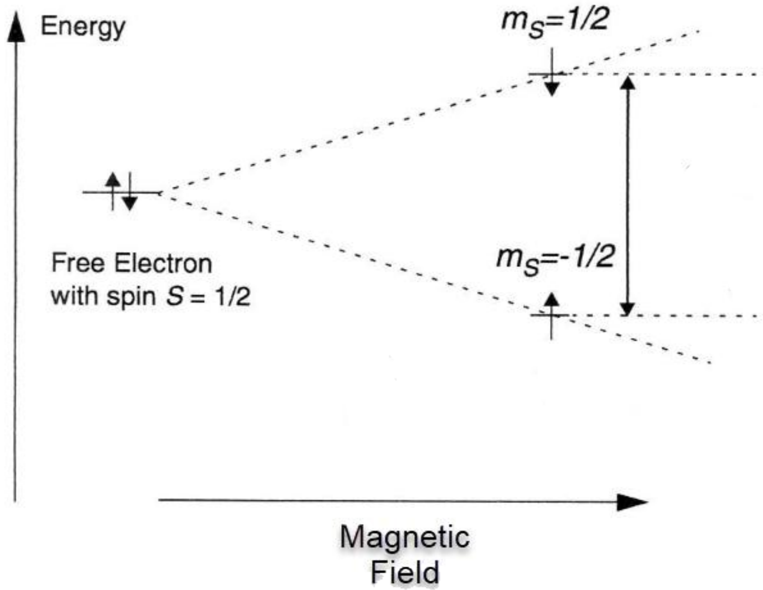

Figure 2.9: Zeeman split of the electron energy states in a magnetic field

The energy difference (Zeeman energy) between the two energy states that split up in the presence of the externally applied magnetic field can be described by the following equation,

$$\Delta E = g_e \mu_B H \tag{2.70}$$

where g_e is the Landè factor, which for the free electron is equal to 2.0023, and μ_B is Bohr magneton. The magnetic moment now can have only two

orientations, one parallel and one anti-parallel to the direction of the applied magnetic field.
When the energy difference of the energy levels matches the energy of the irradiation we have the resonance condition

$$\Delta E = hv_0 = g_e \mu_B H_r \tag{2.71}$$

where the particle absorbs and emits energy.

In practice, there are two ways to perform an EPR experiment and detect the signal. The first and the most usual one is to use a microwave source that irradiates the sample at fixed frequency (ν_0) and change the value of the magnetic field is changed progressively (figure 2.10). This approach is named continuous wave (CW EPR). When the magnetic field reaches a certain "correct" value (H_r) the resonance condition (eq. 2.71) is fulfilled. The second way to obtain an EPR signal, although less common, is to keep the value of the magnetic field fixed and then sweep a specific frequency range with microwaves, until the resonance condition is obtained.

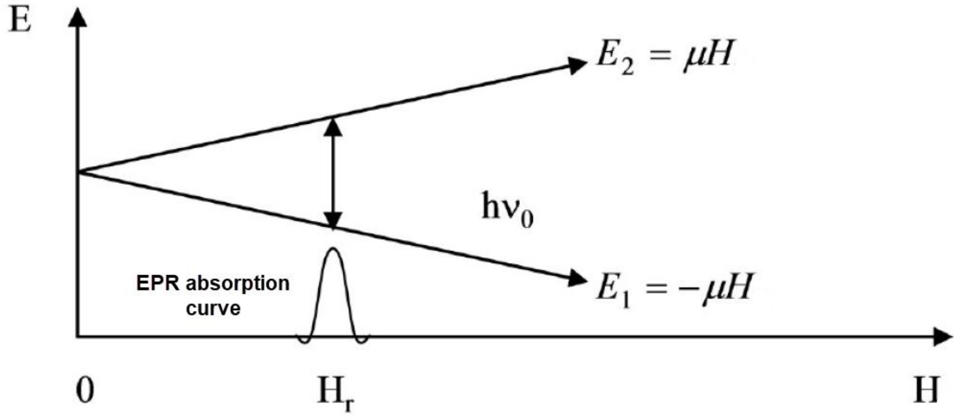

Figure 2.10: Resonance configuration with constant irradiation (ν_0) and changing magnetic field H.

In both ways the results should be the same and the right choice depends on the experimental equipment that one has in disposal. For a typical CW X-band EPR experiment on free radicals characterised by $g_e \simeq 2$ the resonance magnetic field is $H_r \simeq 0.335$ T.

2.8.1 Zeeman anisotropy and the g-factor

Zeeman anisotropy causes a dependence of the electron energy levels on the orientation of the applied magnetic field with respect to the symmetry axis of the paramagnetic center. The orientation of this axis is determined by the crystal field at the electron in a sample. Accordingly, depending on the orientation the resonance field may be different. In the most general case, the spin Hamiltonian that describes the Zeeman interaction taking into account the three components of g-factor is,

$$\mathcal{H}_S = \mu_B(g_x H_x S_x + g_y H_y S_y + g_z H_z S_z). \tag{2.72}$$

In the case that the crystal field of the electron is isotropic (cubic symmetry) the three components of the g-factor have the same value and we have:

$$g_x = g_y = g_z = g_{iso}. \tag{2.73}$$

If the crystal field of the electron has an axial symmetry and supposing that the symmetry is along $\widehat{z}$ the equation 2.72 becomes

$$\mathcal{H}_S = \mu_B H(g_{\|} \cos\theta S_z + g_{\perp} \sin\theta S_y) \tag{2.74}$$

where θ is the angle between the axis z and the xy plane, $g_{\|} = g_z$ and $g_{\perp} = g_x = g_y$. Here the effective g-factor can be calculated from the equation 2.75

$$g^2(\theta) = g_{\|}^2 \cos^2\theta + g_{\perp}^2 \sin^2\theta. \tag{2.75}$$

Finally, in the case of rhombic symmetry of the crystal field for all three directions there are different resonant fields. Then the spin hamiltonian takes the following general form

$$\mathcal{H}_S = \mu_B H(g_x \alpha S_x + g_y \beta S_y + g_z \gamma S_z) \tag{2.76}$$

where α, β and γ are the directional cosines of the angles that are formed between the magnetic field vector and the Cartesian coordinate axis. The effective g-factor here obeys the following relation.

$$g^2 = \alpha^2 g_x^2 + \beta^2 g_y^2 + \gamma^2 g_y^2. \tag{2.77}$$

The different components of the g-factor can be found experimentally by setting the external magnetic field parallel along the three different axis if the sample is a single crystal. In case the sample is a powder of crystallites or a frozen solution, the paramagnetic centres have random orientations and we have a distribution of resonant fields. As a result, the EPR signal becomes broader. Specifically, in the case of the axial symmetry of the g-factor, there is a statistical accumulation of centers with spins oriented onto the xy plane and the EPR absorption at $H_{\|}$ is higher while at $H_{\perp}$ is lower (figure 2.11). For centers with intermediate orientations a continuous distribution of EPR absorption signals is observed.

From the g-factor we can obtain informations about the molecular symmetry around the paramagnetic center and the electronic structure of the atoms.

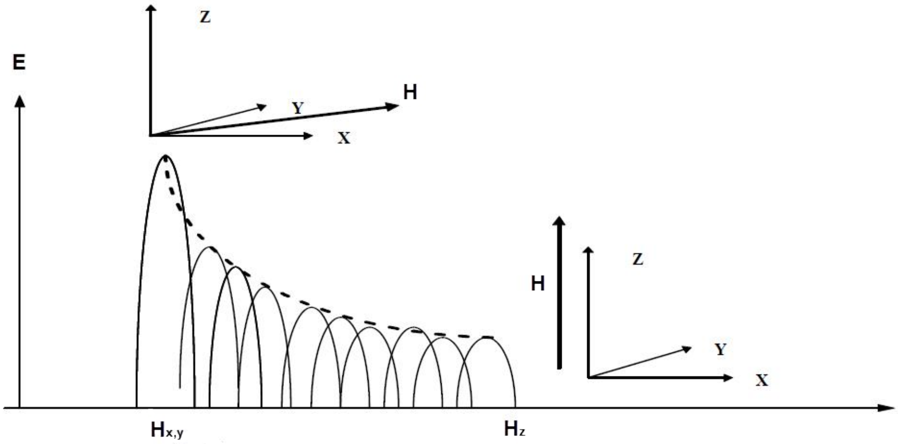

Figure 2.11: Absorption EPR powder spectrum of a system with Zeeman anisotropy of axial symmetry.

2.8.2 Hyperfine interaction

The interaction between electron spins and nuclear spins plays an important role in the EPR spectra giving information about the magnetic local field sensed by the paramagnetic center and the characterization of the molecular structure around it. Many stable isotopes with a non zero nuclear spin (I), like for example ${}^{1}H(I=\frac{1}{2}),{}^{14}N(I=1)$ and ${}^{63,65}Cu(I=\frac{3}{2})$, can interact with the electron spin (S) producing a local magnetic field at the electron site and this leads to a further split of the energy levels that obeys the $(2I+1)$ rule. The spin hamiltonian that describes the system is given by the equation 2.78

$$\mathcal{H}_S = \mu_B g_e \overrightarrow{S} \cdot \overrightarrow{H} + A\overrightarrow{S} \cdot \overrightarrow{I} - \gamma\hbar\overrightarrow{I} \cdot \overrightarrow{H} \tag{2.78}$$

where γ is the nuclear gyromagnetic ratio and A is the hyperfine coupling constant.

There are two different mechanisms[95] that determine the hyperfine interaction: the Fermi contact interaction and the electron-nucleus dipole-dipole interaction (see also sections 3.5.1 and 3.5.2). So, the hyperfine coupling constant becomes

$$A = \alpha + A_{dip} \tag{2.79}$$

where α and A_{dip} are the coupling constants for the Fermi contact and the dipole-dipole interaction respectively. The first interaction is usually related to the probability of the electron to be found at the nucleus site and typically is isotropic and more significant for s-orbital unpaired electrons. On the other hand, the dipole-dipole interaction depends on the relative orientation of the magnetic moments and is anisotropic.

2.8.3 Shape and area of the EPR signal

In a typical EPR experimental what we obtain is the intensity of the absorption of the microwaves as a function of the magnetic field intensity. In order to increase the signal to noise ratio of the signal a modulation approach is used. Hence, what we record is the first derivative of the absorption curve (figure 2.12).

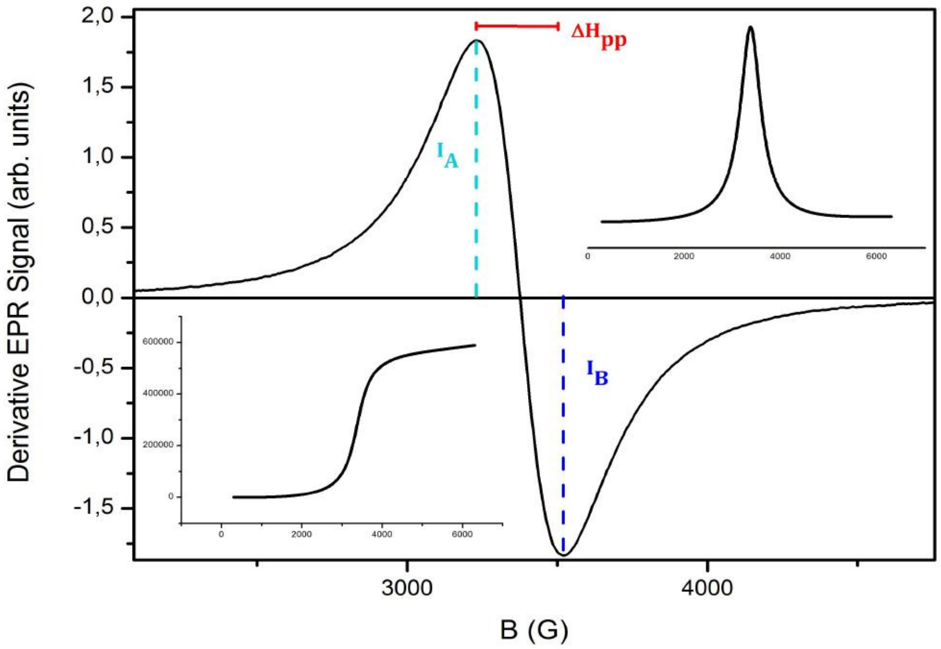

Figure 2.12: EPR absorption signal of Fe^{3+} in pure zinc ferrite at room temperature. The integration and the second integration of the absorption curve can be seen on the upper and the lower corner, respectively.

Usually the EPR resonance line can be either a Lorentzian or a Gaussian curve and from the shape we can obtain information on the magnetic interactions among the electrons and also on the homogeneity of the sample. The broadening of the lines[96] can be either homogeneous or inhomogeneous and the final result is described as a convolution of the two. The usual sources of the homogeneous broadening are the interaction of the electrons with lattice (spin-lattice relaxation) and the interaction among the electron spins (spin-spin relaxation). On the other hand, the common causes of the inhomogeneous broadening are the dipolar interactions between the electrons and the nuclei (hyperfine), the magnetic anisotropy of the g-factor, the chemical disomogeneity of the sample, the presence of different phases but also the inhomogeneity of the applied magnetic field.

From an EPR curve (figure 2.12) we can obtain many important values like the width of the line (ΔH_{pp}) which is characteristic of the sample, the ratio of the intensity of the peaks (I_A/I_B) which is useful in the evaluation of the signal symmetry and also the value of the resonance field (H_r) and the g factor by the equation 2.80

$$g = \frac{h\nu_0}{\mu_B H_r}, \tag{2.80}$$

where ν_0 is the irradiation frequency and $\frac{h\nu_0}{\mu_B} \simeq \frac{1}{1.3996}$.

Another parameter that can be obtained from an EPR curve and more specifically the second derivative of the absorption curve is the intensity of the signal. Knowing this value the number of paramagnetic centres that the sample contains can be calculated from the comparison with a reference sample using the following formula (eq. 2.81)

$$N_S = \frac{Area}{Area_{Stand}} \frac{H_{modStand}}{H_{mod}} \frac{g^2_{Stand}}{g^2} \frac{S_{Stand}(S_{Stand}+1)}{S(S+1)} \sqrt{\frac{P_{Stand}}{P}} N_{Stand} \tag{2.81}$$

where H_{mod} is the amplitude of the modulation field, S is the spin quantum number and P is the microwave power. The index "Stand" stands for a standard paramagnetic compound (Strong Pitch, pitch in KCl) with an already known number of spins $N_{Stand} = 6 \times 10^{15}$, electron gyromagnetic ratio $g_{Stand} = 2,0028$ and electron spin $S_{Stand} = \frac{1}{2}$ that has been used as reference sample.

Furthermore, from the variation of the value of the area of the EPR signal as a function of the temperature it is possible to follow the evolution of the magnetic susceptibility of the ions[97] and to distinguish the magnetic contribution of the different EPR active nuclei that are present in the sample.

Chapter 3

Dynamic Nuclear Polarization

Despite of the wide applicability of NMR, the signal is limited by three basic constraints: the low sensitivity at room temperature, where the population difference is of the order of 10^{-6} with respect to the total number of nuclei, the small nuclear magnetic moment and in some cases the low natural abundance of the isotopes. Thus, since it is difficult to change the amount of probe-nuclei in a sample, keeping the initial characteristics of the material unchanged, great effort has been made to enhance the reduced sensitivity that arises basically from the low nuclear Zeeman split with respect to the thermal energy. The polarization, which the NMR signal is proportional to, is not only proportional to the population difference between the nuclear energy levels, namely to the intensity of the externally applied static magnetic field and to the inverse of the temperature. So by using the techniques presented in this chapter we will see how, controlling external parameters we can hyperpolarize the nuclei.

Another possible solution is to transfer the polarization from highly polarized electrons spins, to the less polarized the nuclear spins. Due to interactions between the species, the polarization transfer is possible and an increase of nuclear polarization and thus an enhancement of the population difference between the nuclear energy levels. As a result, also the NMR signal is increased and the sample reaches the so-called hyperpolarized state.

There are different techniques that one can use in order to reach the hyperpolarized state which use either optical or microwave radiation to excite the electronic system but the most recent and with more promising results is the dynamic nuclear polarization (DNP)[98]. It is based on the polarization transfer from paramagnetic centrers that are homogeneously dispersed into the sample, to the specific nuclear spin species by suitable microwave irradiation of the electron spins. Hereafter the different hyperpolarization techniques will be presented with a more detailed description of DNP mechanisms.

3.1 Brute Force

The key aspect of the enhancement of the NMR signal is the population difference between the nuclear energy levels, or better the polarization of the nuclear spins. The equation that describes the polarization is

$$P_n = \frac{\Delta N_\pm}{N} = \tanh\left(\frac{\gamma\hbar H_0}{2k_B T}\right) \tag{3.1}$$

where $\Delta N_\pm$ is the population difference between the $m_I = \pm\frac{1}{2}$ levels of an $S = \frac{1}{2}$ nucleus as ^{1}H or ^{13}C as we can see in figure 3.1, N is the total number of the nuclear spins, γ the gyromagnetic ratio and H_0 the applied magnetic field.

Since the gyromagnetic ratio of the nuclei is much lower than the one of the electrons ($\leq 10^{-3}$) the polarization is generally low. But as we can see by the formula the population difference, that has to be increased, is proportional to the applied magnetic field and inversely proportional to the temperature. This means that the polarization can be amplified by external parameters that can be controlled. Here comes one of the hyperpolarization techniques called Brute Force Method[99]. By reaching extremely low temperatures (~1 mK) and applying high magnetic fields (~20 T) we can obtain highly hyperpolarized states. Unfortunately this is not the best case scenario. In general it is difficult and expensive to reach such extreme conditions and especially, if the final goal is a biomedical application, it is not all that practical.

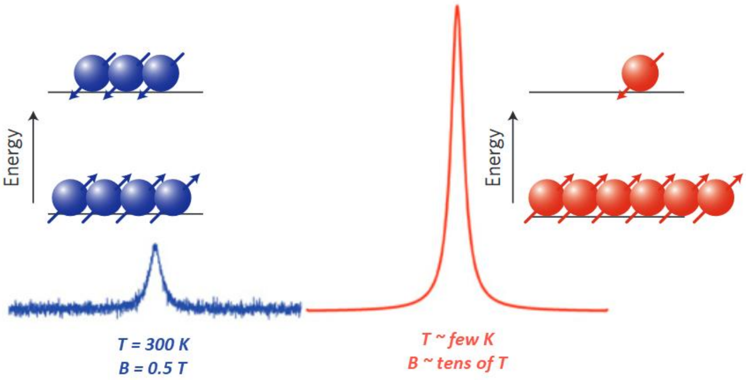

Figure 3.1: NMR signal enhancement with the application of the Brute Force method. Figure adapted from *Munnemann et al.* [100].

3.2 Spin Exchange Optical Pumping

Spin Exchange Optical Pumping (SEOP)[101] is widely used to produce hyperpolarized ^3He[102] and ^{129}Xe[103] atoms. The polarization can be enhanced by a factor of 10^4-10^5 and finds its application mainly in lungs MRI[104].

The He or Xe gases are inhaled by the patient before the procedure for in-vivo metabolic imaging.

The vast majority of SEOP experiments use high-power diode laser arrays to spin-polarize a Rb vapour by optical pumping.

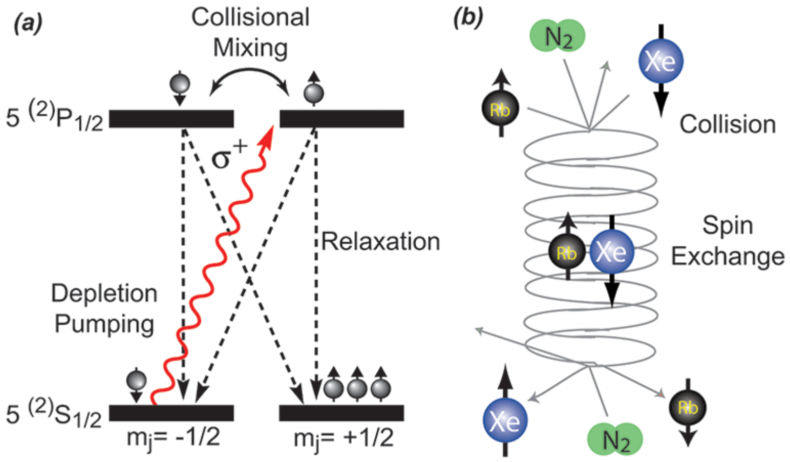

Figure 3.2: Visual representation of the Spin exchange optical pumping mechanism. Metallic Rb is excited at higher energy levels by optical irradiation and relaxes through non-radiative processes. The polarization is transferred to the Xe nuclei through the hyperfine interaction after collisions of Rb and Xe atoms. Figure adapted from *Goodson et al.* [105].

Resonant circularly polarized light is absorbed by the alkali vapour which is excited to a higher energy level. Then it relaxes through non-radiative processes (addition of N_2 for fast quenching) and through collisions with the ^{129}Xe atoms the polarization is transferred from the alkali-metal electrons to the nuclear spin of the ^{129}Xe thanks to the weak hyperfine interaction. Limits of this method can be the consistency of the SEOP cell and the high energy laser needed for the Rb excitation especially for a large scale production of the hyperpolarized helium gas.

3.3 Parahydrogen Induced Polarization

Parahydrogen Induced Polarization (PHIP)[106] is a hyperpolarization technique driven by a chemical reaction, where the nuclear singlet state of parahydrogen is used as a source of hyperpolarization and allows a fast build-up of polarization. This technique is relatively cheap and easy to perform finding application in MRI in-vivo molecular imaging[107]. Parahydrogen itself possesses nuclear spin equal to zero, thus it is not NMR sensitive. By means of fast field cycling[108] or after radiowave irradiation[109], the molecule becomes NMR active but its sort relaxation time does not allow the in-vivo application and here rises the necessity of its polarization transfer to nuclei with longer relaxation times.

For the production of parahydrogen, we start by molecular gas hydrogen that contains orthohydrogen (triplet nuclear spin state) and parahydrogen (singlet spin state) in a ratio 3:1. The conversion of the first to the latter can be achieved at low temperatures in a presence of a catalyst (charcoal or iron oxide). The parahydrogen enriched gas interacts with the substrate surface (hydrogenation) that contains nuclei with long relaxation times, like ^{13}C or ^{15}N, that we intend to hyperpolarize. The chemical reaction breaks the magnetic symmetry of parahydrogen (becomes polarized) and the polarization (spin order) is transferred to the desired nuclei, intra-molecularly, via spin-spin coupling (J-coupling). When the hydrogenation reaction is achieved in high magnetic field the experiment is referred as PASADENA[110] while in low magnetic fields it is referred as ALTADENA[111].

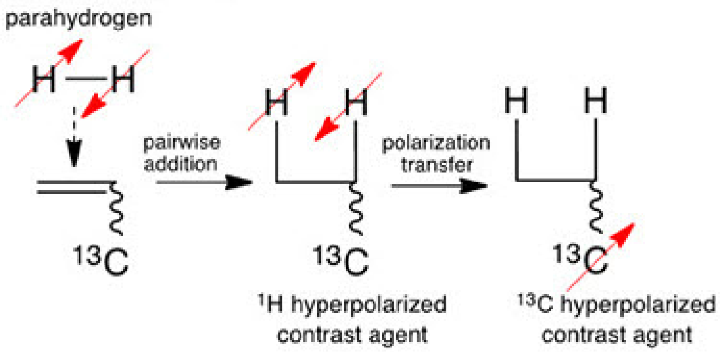

Figure 3.3: Representation of the PHIP mechanism. Parahydrogen interacts chemically with the substrate (hydrogenation). The magnetic symmetry of the molecule brakes due to the reaction, transferring the polarization to carbon nuclei.

3.4 Nitrogen-Vacancy centres in diamonds

A rising alternative to the usual low temperature and high magnetic field nuclear hyperpolarization is the use of optically pumped Nitrogen-Vacancy (NV) centres in diamonds that can lead to sufficient hyperpolarization at room temperature[112]. They can be used either as MRI contrast agents in the nanoscale for hyperpolarized ^{13}C studies[113] or as means of hyperpolarization transfer to liquids and gasses for biomedical use[114, 115].

NV centres are negatively charged color defects in the crystal structure of diamond that possess an electronic spin $S = 1$. They are characterised by a ground state triplet and an excited state triplet with a zero field split and it can be easily optically excited with green light (532nm) as we can see in figure (3.4a).

Hence the system has two important properties: a) the state $m_S = 0$ is not affected by the application of an external magnetic field while we have the removal of degeneracy for the states $m_S = \pm 1$ and b) the system preferentially,

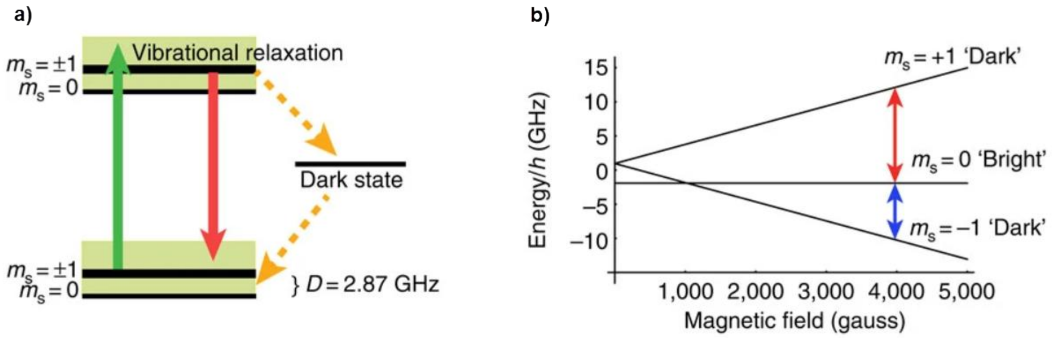

Figure 3.4: a) Ground and excited triplet state of the NV center ($S = 1$) in diamond. The excitation can be achieved optically at 532 nm (green arrow) while its relaxation to the ground state is a non radiative process. b) Application of magnetic field along the crystal orientation and Zeeman split of the $m_S = \pm1$ states. The $m_S = 0$ state is not affected by the magnetic field. Figure adapted from *King et al.* [112].

through non-radiative transitions, populates the $m_S = 0$ state. So, in figure (3.4b) we have the energy split of the $m_S = \pm1$ states and by applying proper microwave irradiation we can polarize the system. Then, thanks to a combination of thermal mixing (see section 3.5.3) and by solid effect mechanism (see section 3.5.2) the polarization passes to the ^{13}C atoms in the proximity (first-shell). Finally the polarization passes to the rest of the sample, in a certain volume that is defined by the spin diffusion process (see subsection 3.5.3.1). It is worth to be mentioned that the magnetic field has to be applied along the symmetry axes of the crystal.

3.5 DNP mechanisms

There are four different mechanisms through which we can obtain a hyperpolarized state due to DNP. The first and older one is called Overhauser effect (OE)[116]; where the nuclear spin polarization could be enhanced by the microwave irradiation of the conduction electrons in certain metals or of unpaired electrons in liquids. The second is the Solid effect (SE) where Abragam and Proctor[117] achieved hyperpolarization by irradiating the electronic system at a frequency slightly different than the Larmor resonance frequency; the difference being given by the nuclear resonance frequency. The third one is called Cross Effect (CE) where two unpaired electrons are needed as polarizing agents; the three spin system can produce hyperpolarization by simultaneous change of spin orientations. The fourth and last mechanism is known as Thermal Mixing (TM) and is very similar to the CE although, in this case, the nuclear spin interacts with an ensemble of electrons characterized by large inter- electron interactions. The three later mechanisms exploit the magnetic dipolar hyperfine interaction in the polarization transfer process.

3.5.1 Overhauser Effect

The polarization is transferred by the spins of the free electrons of the metal to the nuclear spins due to the hyperfine interaction between the two spin species. This hyperfine interaction is dominated by the scalar Fermi contact interaction, which arises by the probability of the s-orbital free electron to be found at the nucleus.

Supposing that we apply an external magnetic field along the $\widehat{z}$ axes, then the total Hamiltonian of the system can be written as

$$\mathcal{H} = \gamma_e \hbar S_z H_0 + \alpha \overrightarrow{I} \cdot \overrightarrow{S} - \gamma_n \hbar I_z H_0 \tag{3.2}$$

where the first and the last terms indicate the Zeeman split due to the applied magnetic field for the electron and nuclear spin systems, respectively, while the second term represents the hyperfine interaction of scalar nature between the two spin species with the coupling constant[118] being equal to $\alpha = \frac{-8\pi}{3}\left(\frac{e\hbar^2}{mc}\right)^2 \delta(r)$ with c the speed of light and $\delta(r)$ the Dirac delta function of the electron-nucleus distance. At high magnetic fields, known also as Paschen-Back regime, the relation $\gamma_e \hbar S_z H_0 \gg \alpha$ holds, thus the hyperfine interaction acts as a perturbation of the Zeeman Hamiltonian and the correspondent eigenvalues, can be written as

$$E = \gamma_e \hbar H_0 m_S + \alpha m_S m_I - \gamma_n \hbar H_0 m_I \tag{3.3}$$

where m_S, m_I are the eigenvalues of S_z and I_z. With these quantum numbers we can define the eigenstates $|m_S, m_I\rangle$ that represent the four possible energy states as we can see in figure (3.5). The allowed transitions are characterized by the selection rules for a magnetic dipole

$$\begin{cases} \Delta m_S = \pm 1, & \Delta m_I = 0 \\ \Delta m_S = 0, & \Delta m_I = \pm 1 \end{cases} \tag{3.4}$$

and the resonance frequencies for these transitions are

$$\begin{cases} \omega_{12,21} = \gamma_e H_0 \pm \frac{\alpha}{2\hbar} \\ \omega_{23,32} = \gamma_e H_0 - \gamma_n H_0 \\ \omega_{13,24} = \gamma_n H_0 \mp \frac{\alpha}{2\hbar} \end{cases} \tag{3.5}$$

By irradiating the system with microwaves one changes the population among the electron energy levels and, as a consequence, one changes the population among the nuclear energy levels, thus transfer of polarization is achieved.

Assuming also that the spin-lattice relaxation is much longer than the time of the experiment, that is $T_1 \to \infty$, that nucleus-nucleus transitions are negligible and that the probability of the transition under MW irradiation (W_e) is much higher than the probability of transition because of the electron-lattice interaction (W_{12}, W_{21}), that is $W_e \to \infty$ which implies that $P_1 = P_2$, we can

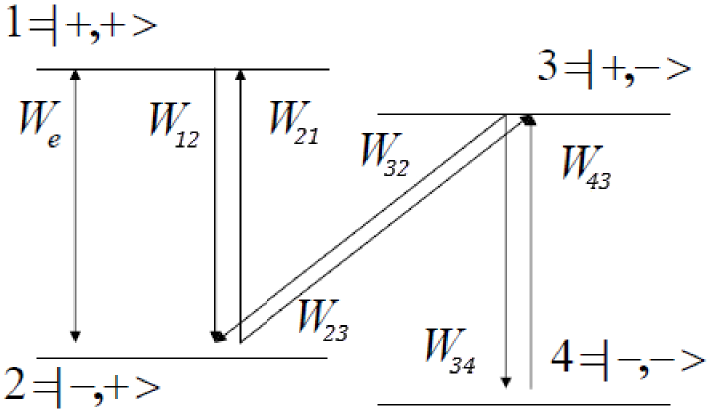

Figure 3.5: Energy level transitions in the Overhauser effect with W_{23}, W_{32} the zero quantum transition rates, W_{12}, W_{21}, W_{34}, W_{43} the double quantum transition rates and W_e the electron excitation probability. The energy difference between the energy levels can be seen by the respective resonance frequencies as reported in the equations 3.5.

write the equations for the time evolution of the population, the so called rate equations

$$\begin{cases} \frac{dp_1}{dt} = p_2W_{21} - p_1W_{12} + (p_2 - p_1)W_e \\ \frac{dp_2}{dt} = p_1W_{12} - p_2W_{21} + (p_1 - p_2)W_e + p_3W_{32} - p_2W_{23} \\ \frac{dp_3}{dt} = p_4W_{43} - p_3W_{34} - p_3W_{32} + p_2W_{23} \\ \frac{dp_4}{dt} = p_3W_{34} - p_4W_{43} \end{cases} \tag{3.6}$$

Recalling the normalization condition for the occupation probability $p_1 + p_2 + p_3 + p_4 = 1$ we can solve the above system of the rate equations in a steady state, where the time evolution of the populations is frozen. So, from the two last equations we have that

$$\begin{cases} \frac{p_1}{p_4} = \frac{W_{43}}{W_{34}} \\ \frac{p_3}{p_2} = \frac{W_{23}}{W_{32}} \end{cases} \tag{3.7}$$

which is what one can find in equilibrium. But at thermal equilibrium, with temperature fixed by the lattice, we can assume that the ratio of the populations is equal to the ratio of the Boltzmann's factors. So,

$$\frac{p_i}{p_j} = e^{\frac{-(E_i - E_j)}{k_B T}} \equiv B_{ji} \tag{3.8}$$

and for the rate equations we have

$$\begin{cases} p_1 = p_2 \\ p_3 = p_2B_{23} \\ p_4 = p_2B_{23} \end{cases} \xrightarrow{p_1+p_2+p_3+p_4=1} \begin{cases} p_2 = \frac{1}{2+B_{23}+B_{24}} \\ p_3 = \frac{B_{23}}{2+B_{23}+B_{24}} \\ p_4 = \frac{B_{24}}{2+B_{23}+B_{24}} \end{cases} \tag{3.9}$$

Then the average value of the $\widehat{z}$ component of the nuclear spin turns out to be

$$\langle I_z \rangle = \sum_i p_i \langle i|I_z|i\rangle = \frac{1}{2}\left(\frac{2 - B_{23} - B_{24}}{2 + B_{23} + B_{24}}\right) \tag{3.10}$$

and in the high temperature limit where the energy separation is much smaller than the thermal energy $E_{ij} \ll k_B T$ the Boltzmann's factor becomes

$$e^{\frac{-E_i}{k_B T}} \simeq 1 - \frac{E_i}{k_B T} \tag{3.11}$$

while for the polarization, recalling that electron transition energy is much larger than the hyperfine interactions and the nuclear transition energy, we have that

$$\langle I_z \rangle_{MW_{on}} \simeq \frac{1}{2}\frac{\gamma_e \hbar H_0}{4 k_B T}. \tag{3.12}$$

With the microwaves turned off we have that $p_1 \neq p_2$ and especially for the ratio of them $\frac{p_1}{p_2} = \frac{W_{21}}{W_{12}} = B_{21}$. So, we can obtain for the polarization that

$$\langle I_z \rangle_{MW_{off}} \simeq \frac{1}{2}\frac{\gamma_n \hbar H_0}{2 k_B T}. \tag{3.13}$$

By calculating the ratio of the polarization for the same system with the microwaves turned on and off we obtain that we have a hyperpolarized state and as a result a signal gain equal to the ratio of the electron and two times the nuclear gyromagnetic ratio, so

$$\frac{\langle I_z \rangle_{MW_{on}}}{\langle I_z \rangle_{MW_{off}}} \simeq 10^3. \tag{3.14}$$

In fact, this result stands, assuming a complete saturation of the electrons and that the only relaxation process is due to the scalar Fermi contact interaction. In more realistic conditions, the nuclear enhancement is given by the relation $\gamma_n + s\left(\frac{T_{1n}}{T'_{1n}}\right)|\gamma_e|$, where the factor s lies between 0 and 1 and indicates the level of electron saturation, while T_{1n} and T'_{1n} represent the total nuclear relaxation and the relaxation due to the Fermi contact interaction, respectively.

As mentioned before, this effect was first described theoretically by Overhauser and then proved experimentally by Carver and Slichter[119] for the nuclei of metallic lithium as we can see in figure 3.6. Here, the upper line represents the thermal signal of the nuclei of metallic lithium without microwave irradiation. This is a signal proportional to the magnetization $M = \hbar\gamma\langle I_z \rangle$, where the magnetization turns out to have a Curie type form, as calculated before. Since the signal to noise ratio can be very small no signal is detected. When one irradiates the electron system at the Larmor frequency one observes the resonance curve and the experimental proof of Overhauser's theoretical findings.

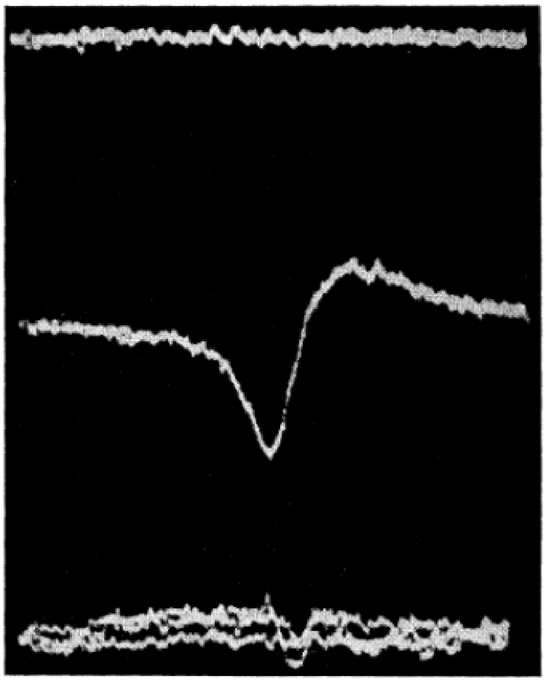

Figure 3.6: NMR signal of metallic ^{7}Li in the absence (top) and in the presence (middle) of microwave irradiation. In the bottom it is depicted the ^{1}H NMR signal of glycerine. Figure adapted from *Carver et al.* [119].

As an extension to this, we can mention that the polarization is not necessarily transferred just from the electron spin system to the nuclear spin system but is also possible a transfer of polarization from a nuclear spin species to another one, as long as we irradiate at the resonance frequency of the one of the two species and there is of course an interaction between them. This is indicated as nuclear Overhauser effect (NOE)[120].

3.5.2 Solid Effect

Another mechanism of polarization transfer that this time is taking place in insulating solids is the Solid Effect (SE). This mechanism shows some common elements with the OE but there are also relevant differences: the electron-nucleus transition is induced after microwave irradiation at a frequency that differs from the electron Larmor frequency by the nuclear Larmor frequency and the interaction between the electrons and the nuclei is not any more the scalar Fermi contact interaction characteristic of metals but the dipole-dipole one. So in the SE mechanism the spin Hamiltonian (eq. 3.2) takes the form

$$\mathcal{H} = \gamma_e \hbar S_z H_0 + \gamma_e \gamma_n \hbar^2 \left[\frac{\overrightarrow{I} \cdot \overrightarrow{S}}{r_{IS}^3} - 3 \frac{(\overrightarrow{I} \cdot \overrightarrow{r}_{IS})(\overrightarrow{S} \cdot \overrightarrow{r}_{IS})}{r_{IS}^5} \right] - \gamma_n \hbar I_z H_0 \quad (3.15)$$

where again the first and the last terms represent the Zeeman interaction of the electrons and the nuclei, respectively, and the second term represents the dipole-dipole interaction between the two spin species.

Lets examine an ensemble of electron and nuclear spins with spin numbers $S = I = \frac{1}{2}$, where the concentration of the electrons is much lower than the concentration of the nuclei. The ensemble is brought at a low temperature and placed into a static magnetic field such that the electrons are completely polarized while the nuclei almost equally populate the energy levels, that is, they are weakly polarized. Recalling the quantum numbers of the eigenvalues of the previous Hamiltonian and disregarding further interactions with other nuclei or electrons, we have as before the four energy states named by the quantum numbers. $|m_S, m_I\rangle$ and every transition has to obey the dipole selection rules given by the equations (eq. 3.4).

Now we include the electron-nucleus interaction and we suppose that it is much weaker than the Zeeman interaction. So, the dipole-dipole interaction acts like a first order perturbation to the system and permits transitions that previously were prohibited by the selection rules. This means that a simultaneous transition between electrons and nuclei is now permitted and more specifically there are two kinds of these transitions; the simultaneous reversal of the spins at the opposite direction (flip-flop transition) and the reversal at the same direction (flip-flip transition).

In fact, after the application of the first order perturbation theory to the Zeeman separated energy levels, the new eigenstates of the electron and the nuclear spin system as depicted in figure 3.7 can be written as

$$\begin{aligned}
&|+\frac{1}{2},+\frac{1}{2}\rangle - \alpha^*|+\frac{1}{2},-\frac{1}{2}\rangle \\
&|-\frac{1}{2},+\frac{1}{2}\rangle + \alpha^*|-\frac{1}{2},-\frac{1}{2}\rangle \\
&|+\frac{1}{2},-\frac{1}{2}\rangle + \alpha|+\frac{1}{2},+\frac{1}{2}\rangle \\
&|-\frac{1}{2},-\frac{1}{2}\rangle - \alpha|-\frac{1}{2},+\frac{1}{2}\rangle
\end{aligned} \tag{3.16}$$

where α is the mixing factor given by

$$\alpha = \frac{3}{4}\frac{\hbar\gamma_e}{r^3 H_0}\sin\theta\cos\theta e^{-i\phi} \tag{3.17}$$

with r being the distance between the electron and the nucleus and the angles θ and ϕ being the polar coordinates of the distance vector r with the externally applied magnetic field.

Each one of these transitions can be excited by microwave irradiation at frequencies which differ from the electron Larmor resonance frequency by a factor equal to the Larmor resonance frequency of the nuclei: at $\Omega_{\pm} = \omega_S \pm \omega_I$. Here, the electron-nucleus hyperfine interaction results into mixed quantum states permitting the selective excitation of the otherwise forbidden electron-nucleus quantum transitions that lead to a polarization transfer from

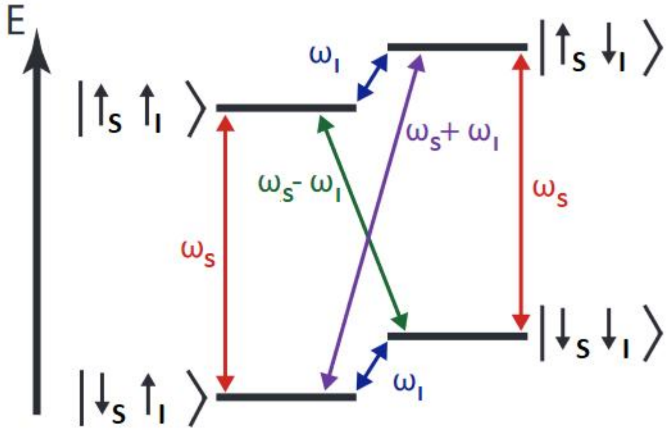

Figure 3.7: Energy level diagram of the four energy states in the Solid Effect regime. The oblique coloured arrows indicate the forbidden transitions. The flip-flop transition is depicted by the violet arrow while the flip-flip transition by the green one.

the electrons to the nuclei and thus a nuclear hyperpolarized state. After the transitions take place, the polarization will pass from the nuclei in the proximity of the electrons to the rest of the sample via the spin diffusion (see section 3.5.3.1) thanks to the nuclear dipole-dipole interaction. The relaxation of the electrons is very fast, for example $\frac{1}{T_{1e}} > 10^3 s^{-1}$, while for the nuclei are supposed to be much slower ($\frac{1}{T_{1n}} \simeq 10^{-3} s^{-1}$)[17]. In order to have an effective spin diffusion the time needed to transfer the polarization across the whole sample should be less than T_{1n}.

It is important to note that for an effective SE there are some conditions that have to be fulfilled: i) the concentration of electrons has to be much smaller than the concentration of the nuclei. The electron spin has to return faster than the nucleus to the equilibrium state in order to have high repeatability of the electron transitions (until all the nuclear spins are polarized). By increasing the concentration of radicals the nuclei relax faster so, one needs to find the optimal level of doping; ii) the SE experiments should be performed at low temperatures and high magnetic field. At higher temperatures the nuclei relax faster because there are other relaxation mechanisms that interfere with T_{1n}. Taking these into account, for an effective SE the following relation should be respected

$$\frac{N_S}{T_{1e}} \gg \frac{N_I}{T_{1n}}. \tag{3.18}$$

If the ESR line of the radicals is narrow, namely $\Delta\Omega_- < \omega_I$, it is possible to excite selectively either the flip-flop or the flip-flip transition. This is known as the Well Resolved Solid effect (WRSE)[121]. In figure (3.8) we can see both transitions; the positive polarization peak represents the flip-flop transition after irradiation at a frequency equal to Ω_- while the negative polarization peak represents the flip-flip transition irradiating at a frequency equal to Ω_+.

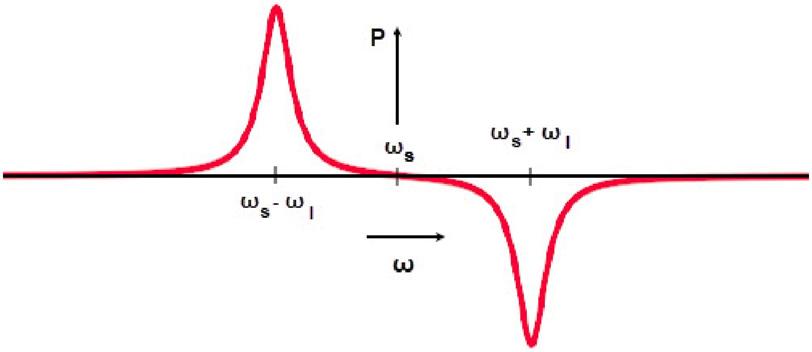

Figure 3.8: Frequency dependence of the nuclear polarization in the case of Well Resolved Solid Effect.

In the case that the radical ESR line is wider, such as $\Delta\Omega_\pm \geq \omega_I$, we are at a condition called Differential Solid Effect (DSE)[122]. In this condition we excite both, flip-flop and flip-flip transition simultaneously. The transitions will counter one another and as a result we will have a polarization which is much lower than in the WRSE while the positive and negative polarization peaks will be superimposed (figure 3.9).

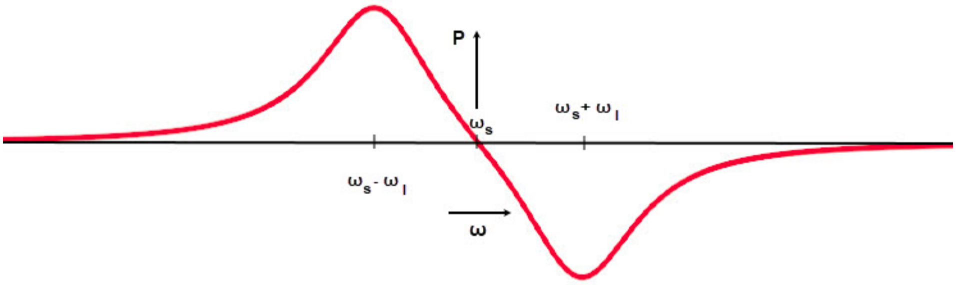

Figure 3.9: Frequency dependence of the nuclear polarization in the case of Differential Solid Effect.

3.5.3 Thermal Mixing

Thermal mixing (TM)[49] is another mechanism of polarization transfer and is basically the most frequent mechanism of polarization in organic systems doped with broad EPR spectrum free radicals ($\Delta\omega_e \gtrsim \omega_n$), with a concentration much lower than the one of the nuclei; typically one has $\frac{N_e}{N_n} \simeq 10^{-3}$, where N_e is the number of the radical molecules and N_n the number of the nuclei in the sample. The radicals supply the system with unpaired valence electrons that are polarized at sufficiently low temperature. The electron polarization is given by the formula,

$$P_e = \tanh\left(\frac{\gamma_e \hbar H_0}{2k_B T}\right) \tag{3.19}$$

so one can achieve high electron polarization at liquid helium temperatures and high fields, typically at temperatures around 1 K and magnetic fields of a few Tesla.

To understand this mechanism we have to separate the system into four thermal baths depending on the interactions characterizing the spins of each bath[123, 124].

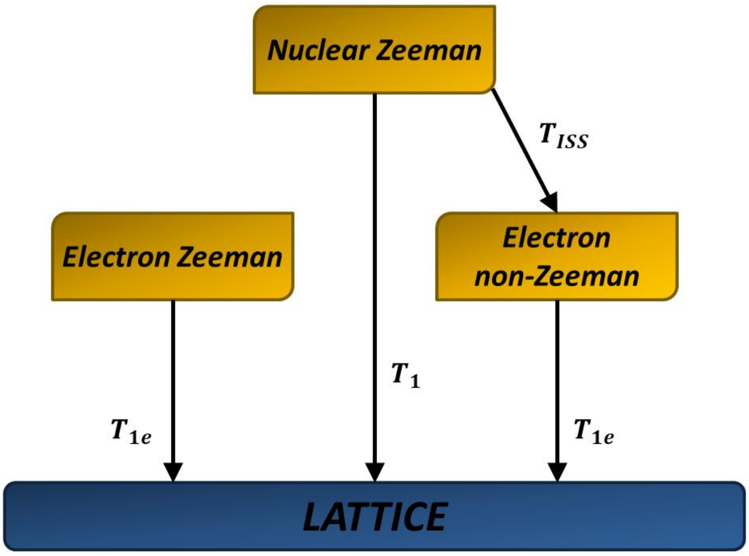

Figure 3.10: Visual representation of the four spin temperature reservoirs and the interactions among them in the TM. The characteristic times describing the relaxation processes and the polarization transfer are also depicted.

In this frame we have the electron Zeeman reservoir that contains the electrons interacting with the external magnetic field, the electron non-Zeeman reservoir which contains the electrons that interact, one with the other via dipolar interaction, the nuclear Zeeman reservoir that contains the nuclear spins that interact with the external magnetic field and finally we have the lattice that contains all the excitations and the glass dynamics characterizing the substrate. (figure 3.10)

This is exactly how the name thermal mixing was derived; from the mixing of the nuclear Zeeman and the electron non-Zeeman temperature spin baths. First we have to irradiate the system and cool the non-Zeeman electron reservoir through a procedure called dynamic cooling. Then thanks to an energy exchange between the cooled non-Zeeman electron reservoir and the nuclear Zeeman reservoir the polarization transfer is achieved. The latter process is a three spin interaction (ISS) that contains the dipole interaction between two electrons of the same reservoir and the hyperfine interaction between the nuclear spin and the electrons. The electron spins interact through the dipole interaction and by recalling the dipole interaction alphabet (eqs. 2.55) and especially the second term, the flip-flop term, we have the simultaneous flip of two electrons. If the dipole interaction is larger than the excitation energy of a nuclear spin we have the flip also of a nuclear spin by the absorption of an energy quantum. In this framework the electronic transitions occur at a frequency $\omega_{MW} = \omega_e \pm \Delta$ where the $\pm$ is assigned to the positive and negative polarization. There are some prerequisites so that this three spins mechanism takes place. The two electron spins do have to interact with the dipole interaction and at least one of them has to interact with nucleus via the hyperfine interaction. This is the triple spin process (figure 3.11) and in this frame we have the polarization transfer to the nuclear reservoir which is our objective.

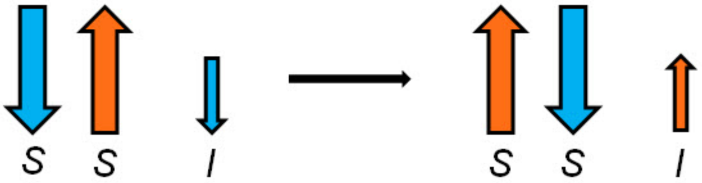

Figure 3.11: Triple spin process with the simultaneous flip of two electron spins (S) and one nuclear spin (I).

Now, to cool down the non-Zeeman reservoir one has to apply the dynamic cooling[125]. After irradiation with microwaves close to the electron resonance frequency, one can induce electronic transitions inside the Zeeman band as can be seen in figure (3.12). The broadening of the two bands is determined by the electron spin-spin interaction, namely by the non-Zeeman reservoir Hamiltonian. In this way, the spin temperature of the non-Zeeman reservoir decreases while the temperature of the Zeeman one increases. This can be seen by the statistical populations of the energy levels which are expressed with the Boltzmann exponents α and β. By irradiating at a frequency slightly below the electron resonance frequency ($\omega_{MW} = \omega_e - \Delta$) it is possible to excite the upper electrons of the lower band and populate the lower states of the upper band and cool the non-Zeeman reservoir. On the other hand, if we irradiate the system at a frequency slightly higher than the electron resonance frequency ($\omega_{MW} = \omega_e + \Delta$) it is created a population inversion inside the electron band reaching a negative temperature. Since $\beta > \alpha$ and both terms are inversely proportional to the $k_B T$ the dynamic cooling is achieved.

Finally in figure (3.13) one can see the curve of the polarization versus the resonance frequencies in the Thermal Mixing regime. In comparison with the WRSE there is non-zero polarization plateau between the positive and negative polarization curves. This is another way to identify and distinguish the two DNP mechanisms[126] except from the irradiation frequency and the distance between the positive and the negative polarization peaks.

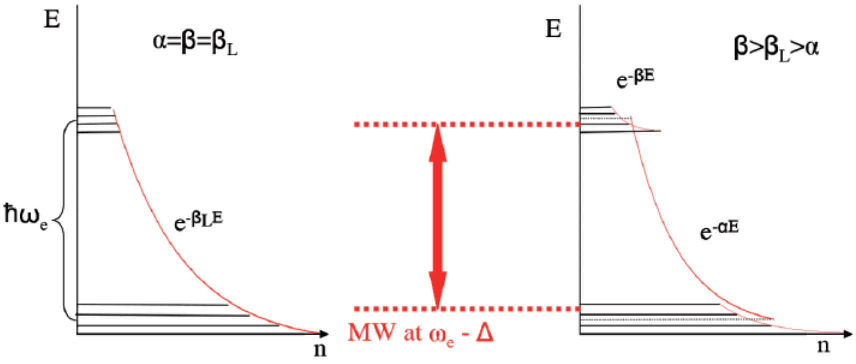

Figure 3.12: Microwave excitation of the non-Zeeman reservoir electrons to the Zeeman reservoir in the dynamic cooling process. The spin temperatures of the electron non-Zeeman, Zeeman and lattice reservoirs are represented by the Boltzman exponents α, β and β_L, respectively. Figure adapted from *Lascialfari et al.* [125].

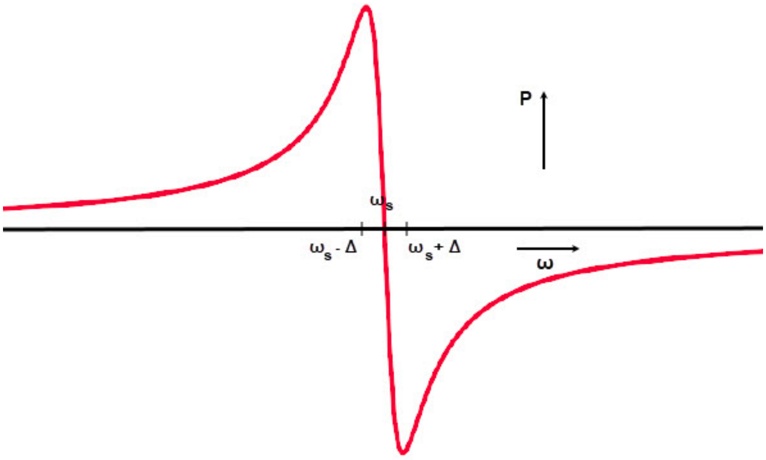

Figure 3.13: Frequency dependence of the nuclear polarization in the Thermal Mixing Regime.

Very similar to the thermal mixing is another mechanism known as Cross Effect (CE)[127]. The difference here stands to the different type of radicals that one uses. Also in this case we have a polarization transfer through a triple spin process. The radicals that are used should have a broad ESR line higher than the nuclear Larmor resonance frequency. Again by irradiating the system at the electron Larmor frequency of the electrons, thanks to the dipole-dipole interaction between them, you have flip-flop transitions and then you have a simultaneous flip of the nuclear spin thanks to hyperfine interactions. But in this case the two electrons are originated by different radical molecules. So it is important to be very close in order to have the dipole-dipole interaction between them ($\propto \frac{1}{r^3}$) but also you have to satisfy the condition for the respective frequencies, namely

$$|\omega_{e1} - \omega_{e2}| \simeq \omega_n. \tag{3.20}$$

In both cases the polarization transfer is immediate but always depends on the precise irradiation frequency and to the kind of radicals or better biradicals[60] and substrates that one uses.

3.5.3.1 Spin diffusion

How is it possible to transfer the polarization to the whole sample if the ratio of the concentration of nuclear and electron spins is of the order of 10^3? With the process described above it is possible to hyperpolarize all the nuclear spins which are placed very close to the paramagnetic centres. For longer distances the hyperfine interaction fades away and the nuclear spins do not sense the previous effect. The solution comes with a recycle of a previously mentioned idea, this time for the nuclear spins. In fact the nuclear spins interact with each other through dipole interactions.

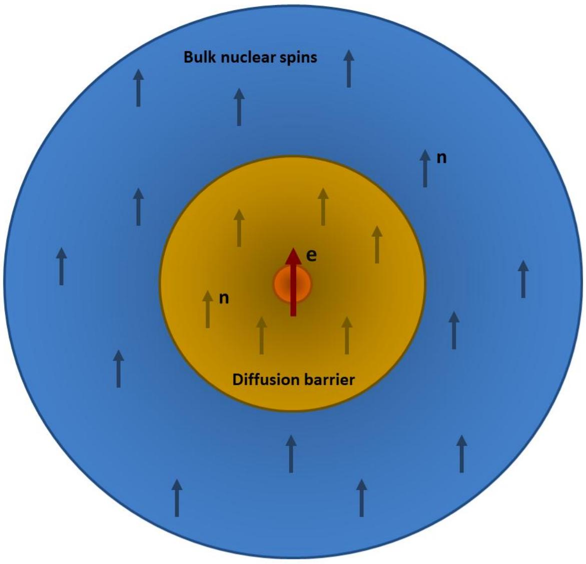

Figure 3.14: The yellow region represents the nuclear spins close to the electron of the radical while the blue region represents the nuclei in the bulk, sited distant from the electron. The polarization transfer from the nuclei of the diffusion barrier region to the ones of the bulk region is determined by the spin diffusion process.

Thanks to the dipole alphabet equations (eqs. 2.55) that contain the flip-flop term, the nuclear spins in the proximity of the paramagnetic center, that are already polarized, can transfer the polarization to the rest of the nuclear spins in the sample. By continuing irradiating the system the nuclear spins in the proximity regain always their polarization and become ”polarization sources” for the rest of the system. This process is called spin temperature diffusion[128]. The time for this process to take place is of the order of $T_2 \cdot n_{step}$, where n_{step} is the number of steps through which the process occurred.

3.5.3.2 Practical limitations of DNP

The solvents in which the TM is achieved are usually exploited for in-vivo molecular imaging and specifically for metabolic changes in the human body. There are basically two practical restrictions to this method. The radical, since it can be toxic for the human body, has to be removed before the solvent is injected and this has to happen very fast otherwise the increase of temperature will destroy the hyperpolarized state. There are several ways to achieve this, including the use of antioxidant scavangers[129] such as ascorbic acid (vitamin C), the radical extraction[130] from the dissolved sample in a hydrophobic solution and the filtering[131] after precipitation. The second holds for the proper polarization transfer. In order to have efficient polarization transfer from the unpaired electrons to the majority of the nuclei the radical has to be homogeneously dispersed[132]. The problem here is that if the forming solvent with the radical is slowly cooled, it will crystallize in an ordered phase system molecular crystal, and the radical will be segregated from the crystal. So it will be distant enough from the nuclei and the polarization will not be transferred. On the contrary, if the cooling is fast, the solvent can form a glass phase, and the radical will remain randomly and homogeneously dispersed.

There are different ways to obtain the glass phase. One of them is to add other substances like glycerol that creates defects in the lattice; these defects are randomly dispersed in the sample and act like hosts for the radical. Another way is to blend the ice formed with mechanical machination methods and obtain a powder that satisfies our restriction. But there is an even better solution to the problem not always achievable. Instead of adding the radical in the solvent, one can create the necessary unpaired electrons by exciting the molecules with, for example, ultra-violet (UV) radiation, some of the molecules reach a paramagnetic state. In practice one exploits the electrons already present in the substrate without the use of toxic radical. After some finite time the molecules will return to their normal state and then the solvent can be safely injected into the human body.

We have also to mention one more important drawback of DNP that is the long polarization build up times. Excluding the time needed for the sample preparation and cooling we need often a couple of hours to polarize the sample which is certainly a practical limitation. To overcome this drawback it has been investigated a method which combines the DNP with the Cross Polarization[133, 134, 135]. CP is another mechanism of polarization transfer that is useful in NMR spectroscopy, this time between two different nuclear species. Suppose that we have a very broad NMR line because of strong interaction between electrons and nuclear spins. The width of the line implies a large dispersion of resonance frequencies. So by a single $\frac{\pi}{2}$ NMR pulse one can flip only a portion A of the spins, those whose resonance lies in the proximity of the pulse frequency. After the $\frac{\pi}{2}$ pulse the total magnetization of these spins along $\widehat{z}$ axes is equal to zero because of the zero population difference and the corresponding spin temperature goes to infinity.

The spins at regions B do not sense the pulse and remain to their former situation with a relative magnetization along $\widehat{z}$ axes due to population difference and spin temperature equal to the lattice one. But both spins A and B are of the same species and interact through dipole nucleus-nucleus interaction.

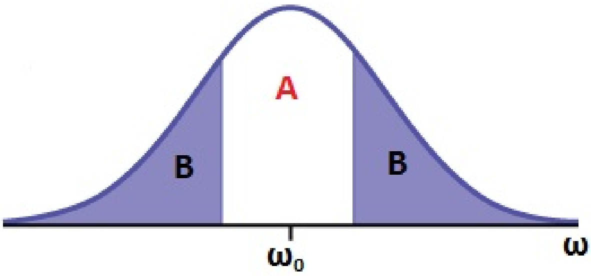

Figure 3.15: Resonance distribution of the nuclei. The blue areas represent the fraction of the nuclei that are not affected by the irradiation.

Thanks to the flip flop term one of the spins A can flip in a certain orientation and the corresponding spin B will flop on the opposite direction in order to equalize the population differences and thus the spin temperature will reach a temperature different from the one of the lattice. This mechanism as mentioned before is the T_2 relaxation. Then, at longer times, the two spin systems will return to equilibrium with the lattice via T_1 relaxation processes.

Since the T_2 relaxation does not require any interaction with the lattice the transfer of polarization will occur only if the Zeeman split, or better, the resonance frequencies of the two spin systems are very close or differ by a quantity smaller than the dipole interaction.

This process cannot work if one considers different spin species. If one has different spin species, the condition of the almost equal resonance frequencies cannot be satisfied. The solution to this problem was proposed by Hann. Even if the resonant frequencies are always different, namely

$$\gamma_S H_0 \neq \gamma_I H_0 \tag{3.21}$$

the precession frequencies of each nucleus around the RF field H_1 can be equal by irradiating both systems with two different fields that satisfy the condition

$$\frac{H_1^S}{H_1^I} = \frac{\gamma_I}{\gamma_S}. \tag{3.22}$$

Under this condition both nuclei in their respective rotating frames rotate at the same frequency. (figure 3.16)

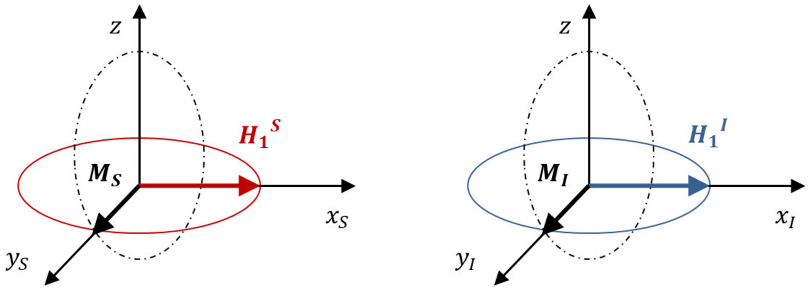

Figure 3.16: Equalizing the precessional frequencies of two different nuclear spins in the CP technique.

So, the component along $\hat{z}$ axes of the spins S rotation on the left side of the above figure will create as oscillating magnetic field that will be seen by the spins I as a small field perpendicular to the larger field H_1^I at the same rotation frequency. That satisfies exactly the resonance condition. So, the rotation of spin S will force the spin I to change orientation in the rotating frame implying a transfer of polarization from spin S to spin I. In this way, thanks to CP, the polarization is transferred to the nuclei with the lowest γ ratio and thus the NMR signal is enhanced. Combining CP with other DNP techniques results into hyperpolarization transfer between different nuclear spin species and further signal enhancement increasing, in the same time, the build-up polarization time.

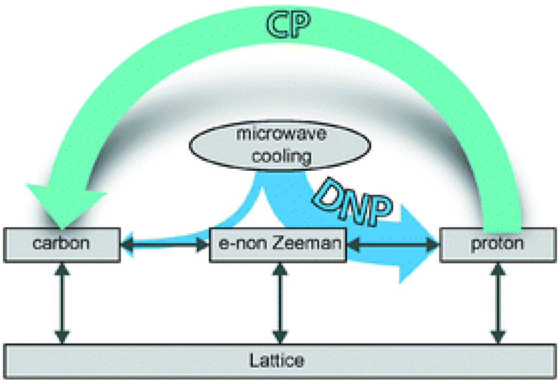

Figure 3.17: Combination of DNP and CP. The polarization is transferred to the ^1H and ^{13}C nuclei by the electrons via DNP and then between the nuclear species via CP. Figure adapted from *Batel et al.* [134]

One more drawback of the technique is the short lifetime of the hyperpolarized state. The sample remains hyperpolarized for a short period of time (several minutes). Of course this implies practical limitations since a polarization center needs to be next to each MRI scanner in order to be used in molecular imaging studies. This problem can be countered by a specific sample preparation. It is possible prepare a sample with two different phases: i) a phase that contains the radicals and a nuclear species A and ii) a phase that contains the same nuclear species A and another one B that you intend to polarize.

By irradiating the system, the unpaired electrons will be polarized and then the polarization is transferred to the spins A of the first phase. Then the polarization is transferred to the same spices A of the second phase, through spin diffusion, and finally arrives at the spins B. Now, since the radicals are spatially separated from the spins B, the hyperfine interaction is no longer effective ($\propto \frac{1}{r^3}$). When the sample is removed by the polariser the radicals relax very fast but the spins B remain hyperpolarized. After special conservation of the sample, at dewars with liquid helium and a relatively small magnetic field applied, the hyperpolarized state survives for several hours[136] and thus the samples can be transported in long distances.

Chapter 4

DNP performance and relaxation in β-CD derivatives

In this chapter the experimental results and the analysis of the aforementioned samples (see chapter 1.3) is presented. First we introduce the basic experimental procedure. Two different experimental configurations were used in order to cover the whole temperature range of the study. For the NMR-DNP measurements we covered the temperature range 1.6-4.2 K using a thermal bath cryostat. In order to reach temperatures below 4.2 K a large rotary pump was attached to the bath cryostat for the adiabatic pumping of liquid helium while, for the precise temperature measurement at the samples' position we used a Cernox sensor. From the vapour pressures at the liquid helium surface the temperature was also measured. Before the experiments, all the samples were immersed directly into the liquid N_2 dewar for fast solidification in an amorphous glass form. In this way the radical molecules remained homogeneously dispersed in the sample allowing an efficient spin diffusion (see subsection 3.5.3.2).

To cover the temperature range 10-320 K we used continuous flow cryostat, with He as cryogenic liquid. A remotely controlled system was used to control the temperature. Furthermore, different coils of the NMR probe resonant circuit were used depending on the configuration and the nucleus under investigation. For the NMR-DNP experiments we used saddle coils, for a better sample irradiation, while at higher temperature NMR measurements traditional solenoid coils were used. In the case of ^{1}H the coils were made by Cu, while in the case of ^{13}C the coils were made by Ag since the resonance frequency of copper nuclei is close to the one of carbon nuclei.

All the NMR and NMR-DNP experiments were performed in a superconducting magnet manufactured by Cryomagnetics, that reaches magnetic fields up to 9 T. For the present study the externally applied magnetic field was 3.4 T and 7 T. All the NMR signals were recorded using a solid-state Apollo Tecmag NMR spectrometer that is operational in a frequency range 6-220 MHz. The power of the NMR pulses, after the power amplifier, reached values up to

300 W.

More specifically, the spin-lattice and spin-spin relaxation times of the ^{1}H and ^{13}C nuclei were measured for the completely methylated doped and non-doped with radical TEMPO β-CD samples. The externally applied static magnetic field for most of the measurements was set to 3.4 T. A home-made DNP-NMR probe was inserted in a cryostat placed inside the superconducting magnet. A manually tunable Gunn diode oscillator was attached on the top of the probe to irradiate the sample in the microwave range 96-98 GHz, with an output power of 30 mW. The NMR RLC circuit was tuned suitably for the detection of the ^{1}H and ^{13}C excitation and the appropriate frequency filters were used. In particular, since the externally applied magnetic field was 3.4T, the ^{1}H the Larmor resonance frequency is $\omega_{^1H} \simeq 147MHz$ and the ^{13}C is $\omega_{^{13}C} \simeq 37MHz$. An extended range of microwave frequency was scanned in order to find the optimal DNP MW frequency.

To measure T$_1$ a train of saturation pulses, followed by a simple FID or a solid spin echo sequence was used. This saturating comb consists of multiple $\frac{\pi}{2}$ pulses perpendicular to the magnetic field direction in order to suppress all the magnetization components in the xy plane, allowing us to study systems with a big distribution of resonance frequencies due to the strong nuclear interactions. After the saturating pulses there is a varying delay time before the last $\frac{\pi}{2}$ (FID) or π pulse (spin echo) that leads to the signal. The magnetic recovery curves, from which we calculated the T$_1$ relaxation times, were constructed by recording the NMR signal as a function of the different delay times between the pulses. The experiments were performed over a wide temperature range as reported in the coming sections. For the spin-spin relaxation time T$_2$ a spin echo sequence was used, as reported in the Appendix chapter B, following the echo decay as a function of the separation between the pulses.

In the case of the Hepta- and Mono-Tempo samples a slightly different set-up and approach was followed. Here, the spin-lattice relaxation times of ^{1}H nuclei were measured with a simple free induction decay sequence (pulse length 2.4 μs). The main difference is found in the experimental set-up where an improved version of the probe was used. The Gun diode was substituted by an external microwave source fabricated by Agilent, that is operational at the frequency range 250 kHz-20 GHz with an output power (-20 - +13) dBm. On the top of the probe a frequency amplifier and multiplier ($\times 6$) was attached in order to reach the desired MW frequency, suitable for the DNP measurements. This change in the set-up allows us to scan a large frequency area with much more precision with respect to the analog system. In this way we are able to explore better the fundamental physical mechanisms that bring our system to the hyperpolarized state. The recovery is described by the following equation

$$M(t) = M_{OFF}\left[1 - e^{-\frac{t}{T_1}^{\beta}}\right] \tag{4.1}$$

in the case where the MW irradiation is switched off, while in the case that MW is on, we have

$$M(t) = M_{ON}\left[1 - e^{-\frac{t}{T_{POL}}^{\beta}}\right] \tag{4.2}$$

where β is the stretching coefficient, M_{OFF} is the nuclear steady magnetization in thermal equilibrium, M_{ON} is the out of equilibrium magnetisation in the presence of microwave irradiation and T_{POL} is the polarization time, namely the the required time for the system to reach the hyperpolarized state. The M_{OFF} and M_{ON} magnetizations are depicted in figure 4.1,left by the plateaus of the recovery magnetisation curves where we can see the relative signal enhancement due to the application of the DNP technique.

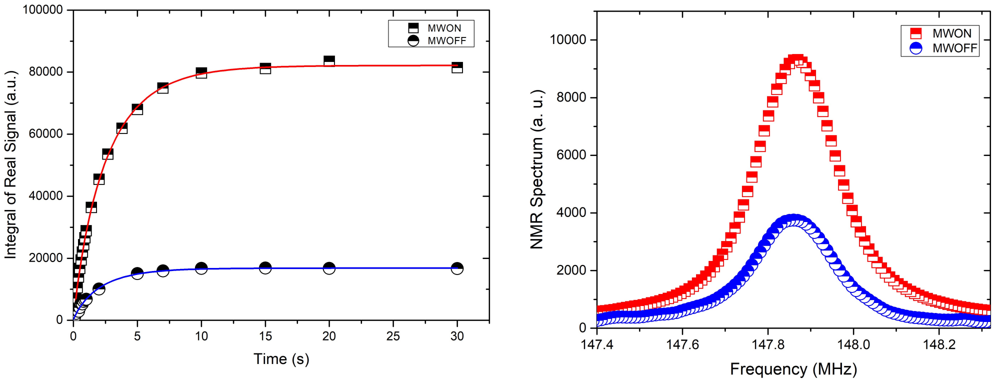

Figure 4.1: Magnetization recovery curve and NMR spectra of ^{1}H with and without MW irradiation of the completely methylated (left) and acetylated (right) $\beta - CDs$ at 4.2 K in a 3.4 T magnetic field. The intensity difference leads to the relative signal enhancement.

To derive T_1, the magnetization recovery curves were analysed with the use of the equations 4.1 and 4.2. The coefficient β in these equations describes the distribution of the T_1 times which could result, in our case, from a distribution of relaxation times caused by the inhomogeneous distribution of the radical molecules. When β tends to unity we approach the optimal case where the spin diffusion yields a common spin temperature and relaxation rate T_2. For all the cyclodextrins samples the stretching coefficient lies in the range $0.70 \leq \beta < 1$. Some examples of the effect of the DNP technique on the NMR signal can be seen in figure 4.1.

To study the behaviour of the Hepta-TEMPO radicals we performed two EPR experiments at 295 K and 120 K. A water cooled electromagnet was used to produce magnetic fields up to 1 T with an X-band spectrometer and an EPR TE_{102} mode rectangular cavity, both fabricated by Bruker. The microwave frequency was constant and equal to 9.46 GHz while the power was set to 18.6 mW. The amplitude of the signal modulation was set to 0.5 G.

4.1 DNP performance

The signal enhancement and the nuclear polarization are two of the basic quantities derived in DNP experiments. The ultimate goal of a DNP experiment is the highest possible signal enhancement and accordingly the highest nuclear polarization. In this section the above mentioned quantities will be presented for the samples investigated. The signal enhancement was calculated with the following equation

$$\epsilon = \frac{M_{ON}G_{OFF}}{M_{OFF}G_{ON}}, \tag{4.3}$$

where the values G_{ON}, G_{OFF} indicate the value of the receiver gains of the spectrometer with and without irradiation, respectively and M_{OFF} and M_{ON} represent are the thermal and the DNP enhanced magnetisation.

On the other hand, in order to calculate the nuclear polarization under MW irradiation we multiplied the thermal equilibrium polarization by ϵ.

$$P(\%) = \epsilon \cdot \tanh\left(\frac{\hbar\omega_n}{2k_BT}\right) \tag{4.4}$$

It is important here to mention that for all the samples containing both ^1H and ^{13}C nuclei the optimal microwave excitation frequency was the same independently of the nuclear species. This is a strong indication that the system is in the thermal mixing regime since in the solid effect regime the optimal frequency varies for different nuclei and should be shifted from the electron Larmor frequency by an amount corresponding to the nuclear Larmor frequency ($\omega_{DNP} = \omega_e \pm \omega_n$).

4.1.1 DNP in completely methylated β-CDs

For this sample series the DNP performance is reported in the figure 4.3 where the DNP enhancement and the nuclear polarization are shown both for ^{1}H and ^{13}C nuclei. Each point represents a separate DNP experiment and it has been obtained as discussed in the introduction of this chapter.

The DNP enhancement of ^{1}H (figure 4.3,left) shows a rather temperature independent behaviour with values that range between $20 \leq \epsilon \leq 30$ corresponding to a nuclear polarization in the range $2 \leq P(\%) \leq 6$. It is possible that this behaviour is due to the fact that although there is very strong coupling of the hydrogen nuclei the spin diffusion process (see section 3.5.3.1) is not optimal because of the fast nuclear relaxation. The substitution of the hydrogen nuclei of the methyl groups with deuterium may also result in a inhomogeneous spin temperature due to the non effective nuclear spin diffusion and in general a worse DNP performance[45]. Nevertheless, the very intense proton signal of these samples, despite the fast nuclear relaxation, might be promising for applications. On the other hand, the importance of the carbon

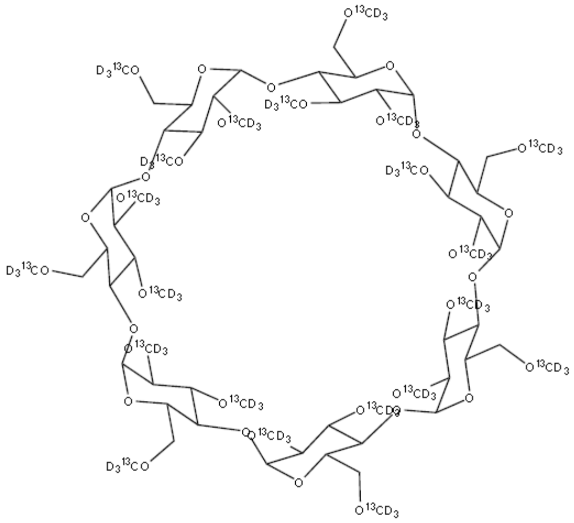

Figure 4.2: Completely methylated and deuterated β-Cyclodextrins marked with ^{13}C with chemical formula $C_{42}{}^{13}C_{21}H_{49}D_{63}O_{35}$.

nuclei for the applications lies in the long relaxation time even at room temperature and of course on the larger chemical shift which allows to better separate the signal from different molecules.

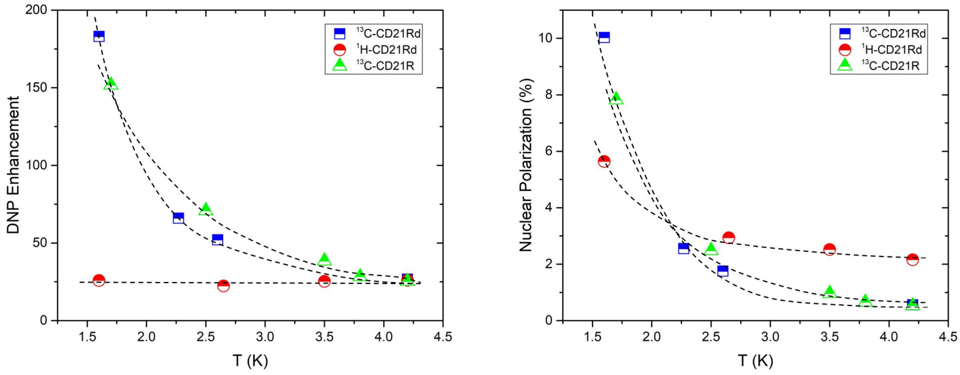

Figure 4.3: Temperature dependence of the DNP signal enhancement (left) and nuclear polarization (right) for proton and carbon nuclei of the completely methylated sample in a 3.4 T magnetic field. The green triangles, in both figures, represent the data from the past work Ref. [44] for comparison. Black dashed lines were added as guides to the eye. The error bars are within the symbols.

Regarding the ^{13}C nuclei performance, the hyperpolarization was efficient achieving a signal enhancement equal to $\epsilon \simeq 180$ at the lowest temperature (1.6 K) that corresponds to a nuclear polarization equal to $P(\%) \simeq 10\%$. It could be mentioned here that the ^{13}C NMR spectra has no particular internal structure and it can be described by a simple gaussian function. This is a rather good result in comparison to other studies[137, 138, 139, 140] if one considers the type of the radical that was used (TEMPO) and the relatively large size of the β-cyclodextrins which is not optimal for the polarization transfer process and the overall DNP performance. Another parameter that affects the DNP performance is the power of the microwave irradiation. It has been seen[137] that for an output power lower than 100 mW the saturation of the EPR spectra of the radicals was not optimal. In the experiments on this series, due to instrumental limitations, the microwave power was 30 mW. Increasing this value may result in even higher polarization. It is worth to be mentioned that the deuteration of the methyl groups, with respect to our past work[44], led to higher DNP signal enhancement and higher DNP enhanced nuclear polarization of ^{13}C nuclei, which was one of our objectives.

4.1.2 Comparison of the effect of Hepta- and Mono-TEMPO radicals on the DNP performance of β-CDs

In figures 4.5 and 4.6 the NMR signal enhancement and the DNP enhanced nuclear polarization of ^{1}H nuclei are presented for the samples of the Hepta- and Mono-TEMPO β-CD series under the optimal irradiation frequency.

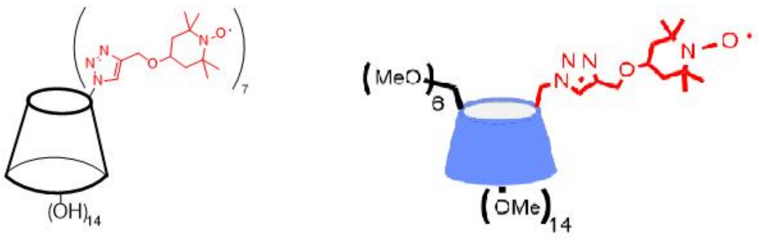

Figure 4.4: Hepta-TEMPO radical doped β-CD with all the seven OH groups of the small molecular rim coupled to TEMPO moieties (left) and Mono-TEMPO radical doped β-CD with all the 21 OH groups being methylated but one which carries a single TEMPO molecule (right). The error bars are within the symbols.

From these figures we are in a position to say that the optimal radical concentration for both sample series is 1% w/w since they present the highest enhancement. In fact, for the Hepta-TEMPO samples the corresponding enhancement of the signal at 1.6 K was $\epsilon \simeq 20$ with nuclear polarization equal to $P(\%) \simeq 4.5\%$ while for the Mono-TEMPO samples we had $\epsilon \simeq 60$ and $P(\%) \simeq 13\%$. The big difference in the DNP performance of the two series lies on the fact that the molecules in the Hepta-TEMPO samples, at lower temperature, reach a high-spin configuration[46] and the relaxation times of the ^{1}H nuclei are much faster resulting in a less efficient spin diffusion because of the broadening of the NMR line and a rapid loss of the hyperpolarized state.

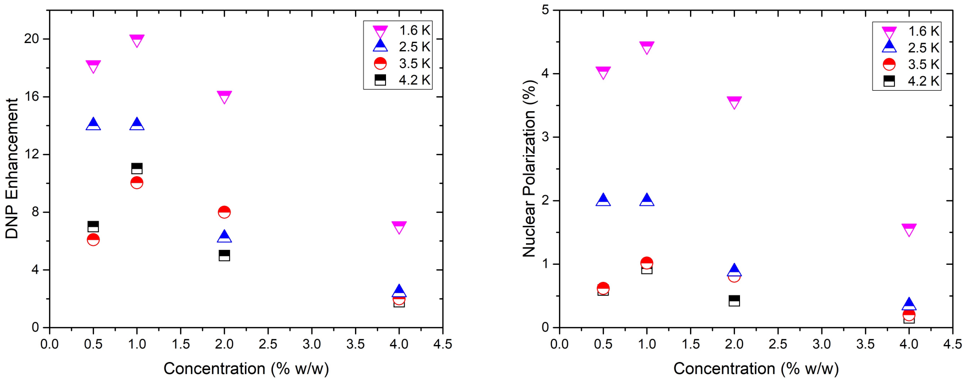

Figure 4.5: Radical concentration dependence of the DNP signal enhancement (left) and nuclear polarization (right) for ^{1}H nuclei of the Hepta-TEMPO samples in a 3.4 T magnetic field, at different temperatures. The error bars are within the symbols.

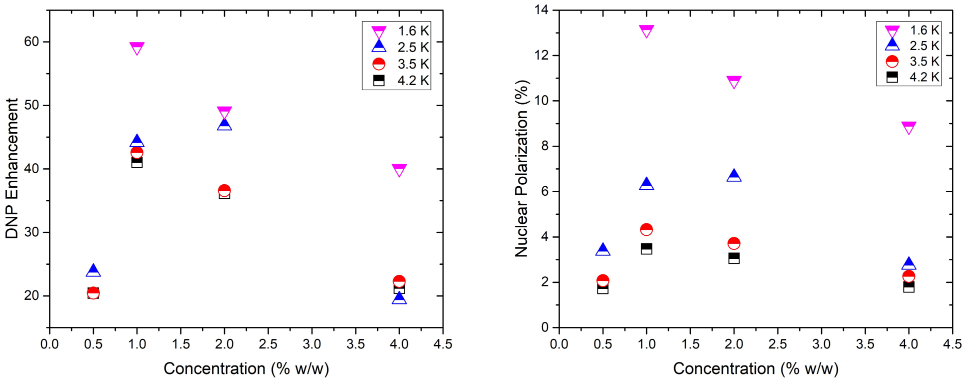

Figure 4.6: Radical concentration dependence of the DNP signal enhancement (left) and nuclear polarization (right) for ^{1}H nuclei of the Mono-TEMPO samples in a 3.4 T magnetic field, at different temperatures. The error bars are within the symbols.

Another important information that can be extracted from the figures 4.5 and 4.6 is that for lower and higher radical concentration than the optimal one the DNP performance reduces significantly. At lower radical concentrations (below 1%) the radical moieties are weakly coupled to each other and they are simply not enough to hyperpolarize properly the whole sample due to an unsatisfactory spin diffusion resulting in a poor polarization transfer throughout the sample. At high radical concentrations (above 1%) we have enhanced electronic spin correlations and an increased hyperfine interaction between the electrons and the nuclei[43]. This results in a non-effective spin diffusion because of the NMR line broadening and a faster relaxation of the nuclei. The polarization transfer is not optimal and it does not have enough time to occur across the whole sample resulting in an unsatisfactory DNP performance.

To complete the study of this "new" radical called Hepta-TEMPO we measured the effect of the radical onto the ^{1}H nuclear polarization for the A_6 (2% w/w) sample by sweeping the microwave irradiation frequency (figure 4.7). Each point of this curve was measured separately, after two minutes of continuous irradiation, with 60 MHz steps and 30 MHz steps close to the peaks.

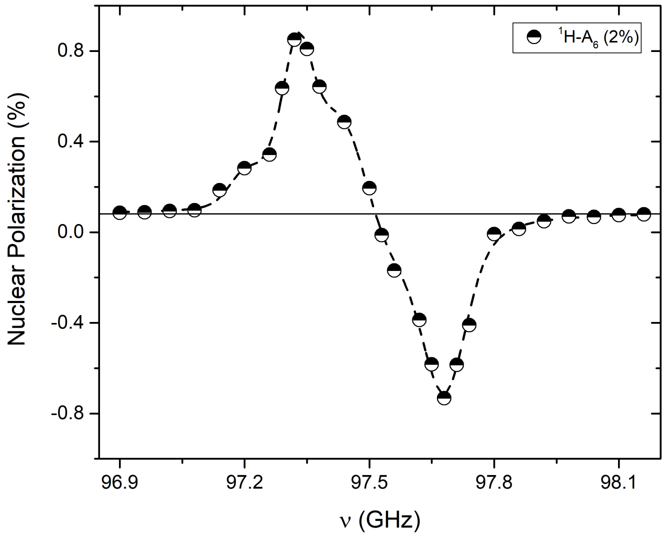

Figure 4.7: Microwave frequency dependence of ^{1}H polarization of the A_6 (2% w/w) Hepta-TEMPO sample at 4.2 K and 3.4 T. The polarization shows positive and negative peaks around ω_e as expected.

The microwave DNP spectrum of ^{1}H is characterised by two peaks with opposite sign that follow the positive and negative derivative of the ESR absorption spectrum of the radical. The two peaks are separated by almost 360 MHz (much longer than the nuclear Larmor frequency), which suggests that the dominant DNP mechanism here is the thermal mixing[141, 142, 123, 126]. In fact, if the principal mechanism was the solid effect the separation of the peaks would be equal to $2\nu_H \simeq 296MHz$, which is not the case. Nevertheless a small contribution through the solid effect cannot be excluded.

Furthermore, in the same figure we can notice that the ^{1}H DNP spectrum is broad and anisotropic which corresponds to the ESR spectrum of the TEMPO radical [48]. The g-factor anisotropy gives this slightly distorted spectra where the heights of the two peaks do not coincide and also gives rise to a broadening in the solid state phase. On the other hand, the hyperfine interaction with the unpaired electron, strongly localised on the nitroxide bond, and the ^{14}N nucleus gives rise to these two bumps on the left and the right side of the positive peak which correspond to different directions of the hyperfine tensor with respect to the external field[48].

4.1.3 Acetylated β-CDs

In figure 4.9 the DNP performance of the ^{1}H and the ^{13}C nuclei contained in the acetylated β-CD samples is shown, namely, the temperature dependence of the DNP enhancement and the DNP enhanced nuclear polarization.

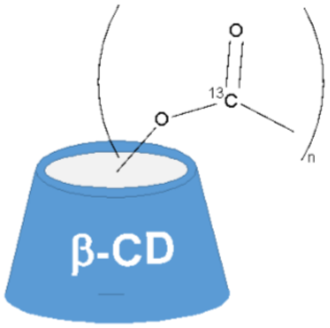

Figure 4.8: Acetylated β-CD molecule with an average number of seven carboxyl groups marked with ^{13}C.

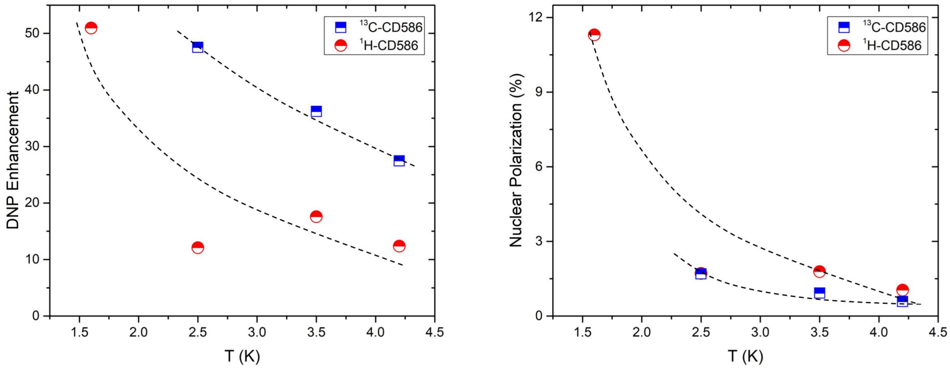

Figure 4.9: Temperature dependence of the DNP signal enhancement (left) and nuclear polarization (right) for proton and carbon nuclei of the acetylated radical doped sample in a 3.4 T magnetic field. Black dashed lines were added as guides to the eye. The error bars are within the symbols.

Regarding ^{1}H nuclei it seems that there is a temperature independent enhancement in the temperature range $2.5 \leq T \leq 4.2$ K, although decreasing even more the temperature an enhancement equal to 50 was achieved at the lowest temperature ($T = 1.6$ K), which corresponds to a nuclear polarization equal to almost 11%. The factor 50 of the enhancement increases tremendously the already strong signal of the protons although the fast relaxation at room temperature act as a limitation factor for practical applications of ^{1}H MRI of these molecules.

In the case of ^{13}C nuclei the highest enhancement value was found equal to almost 50 at temperature 2.5 K, while the corresponding nuclear polarization is almost 2%. In this sample the average number of ^{13}C nuclei per CD molecule is equal to seven. It is possible that the low concentration of the carbon nuclei leads to a less effective spin diffusion (since the nuclear dipole-dipole interaction is inversely proportional to the cube of the distance between the nuclei) and this in turn leads to a decreased nuclear polarization and thus a lower DNP enhancement. A higher concentration of carbon nuclei with a complete acetylation of the CD macromolecules, where all of the carboxyl groups would be marked with ^{13}C, would increase by a factor 3 the carbon nuclear concentration and it could most probably trigger a higher DNP performance.

4.2 Nuclear relaxation and polarization times at low temperatures

In this section we present the nuclear spin-lattice relaxation rate $(1/T_1)$ and the polarization rate $(1/T_{POL})$ behaviour as a function of the temperature. This study is essential since information about the dynamics that dominate our systems at low temperatures can be obtained $(1.6K \leq T \leq 4.2K)$, as well as about the microscopic mechanisms that contribute to the hyperpolarization. Deriving these informations is important in order to understand better the physics behind DNP and further improve the performance for the in-vivo molecular imaging application.

There are two main contributions to the nuclear relaxation, the hyperfine interaction between the nuclei and the free electrons of the radicals and the interaction of the nuclear system with the lattice with nuclei of the same or different species. The hyperfine interaction drives the nuclear relaxation in two ways; i) the electron spin flips and ii) the magnetic field fluctuations at the nuclear site induced by the lattice dynamics which change the e-n distance. It has been seen[17] that the second one has a much smaller fluctuation frequency than the first and contributes to an increase of the relaxation rate. In fact, the main contribution for the relaxation of the nuclei seems to arise from the lattice fluctuations. At such low temperatures all the molecular dynamics of the substrate are frozen but having in mind the amorphous nature of the material, we have to consider that the lattice fluctuations are not the crystalline phonon modes but the glassy dynamics. So, including all the contributions, for the nuclear relaxation rate we have

$$\left(\frac{1}{T_1}\right)_n = \left(\frac{1}{T_1}\right)_{n-n} + \sum_i \left(\frac{1}{T_1}\right)_{n-n_i} + \left(\frac{1}{T_1}\right)_{n-e} \tag{4.5}$$

where n is the nuclear system under study and n_i are the other nuclear species that are present in the sample.

Glassy modes show extremely slow dynamics as observed in disordered systems below the glass transition temperature and describe the molecular fluctuations at a stationary state close to an equilibrium position[17]. These fluctuations of the glassy lattice modify the local structure and thus by modulating the hyperfine interaction responsible for nuclear relaxation affect the relaxation of the nuclei. By increasing the temperature, the glassy dynamics become faster and faster, playing an important role in the relaxation of the nuclei. This effect is present even at very low temperatures, of the order of the Kelvin degree and thus affects also our results.

Since we are in the low temperature regime, the relaxation time T_1 which is governed by slow motion dynamics is described by equation 2.49. The fluctuations around an equilibrium position can be represented by an activated motion, with an energy barrier ΔE, which determines the correlation time that can be described by the Arrhenius law, namely

$$\tau_c = \tau_0 e^{\left(\frac{\Delta E}{T}\right)} \tag{4.6}$$

where τ_0 is the correlation time for $T \to \infty$. However, in a glassy phase the disorder leads to a distribution of barriers which gives rise to a distribution of correlation times

$$< \tau_c(T) >= \int \tau_c(T) p(\Delta E) d\Delta E \tag{4.7}$$

where $p(\Delta E)$ is the energy barrier distribution. So, from equation 2.49 which is expected to be valid at low temperature, the relaxation rate after the introduction of the distribution of the correlation times is

$$\frac{1}{T_1} \simeq \int \gamma^2 < \Delta h_\perp^2 > \frac{1}{\omega_0^2 \tau_c} e^{-\left(\frac{\Delta E}{T}\right)} p(\Delta E) d\Delta E. \tag{4.8}$$

for $\omega_0 \tau_c \gg 1$. It can be seen[43] that by choosing empirically a linear distribution $p(\Delta E) \propto \Delta E$ we have a dependence of the relaxation rate on the square of temperature, namely

$$\frac{1}{T_1} \propto T^2. \tag{4.9}$$

Of course by changing the distribution $p(\Delta E)$ the exponent can change.

Another important time scale can be determined in the presence of microwave irradiation: the polarization time. This parameter is linked to the spin-lattice relaxation time in the thermal mixing regime[143, 132]. Especially if there is an efficient thermal contact between the electron non-Zeeman and the nuclear Zeeman energy reservoir, namely, that the electron relaxation time is much longer than the time needed to fulfil the triple spin process[17], namely,

$$T_{1e} \gg T_{ISS}. \tag{4.10}$$

Under this assumption the following relations for the polarization time and for the time that the system remains in the hyperpolarized state, that is the spin-lattice relaxation time T_1, are satisfied[43, 48]:

$$\frac{1}{T_1} = \frac{1}{T_{1e}} \frac{N_e}{N_n} \left[1 - P_0^2(T)\right] \tag{4.11}$$

$$\frac{1}{T_{POL}} = \frac{1}{T_{1e}} \frac{N_e}{N_n} \tag{4.12}$$

where N_e, N_n are the concentrations of the radicals and the of nuclei while $P_0(T)$ is the nuclear thermal polarization as mentioned before. Both relaxation times are influenced by the spin concentrations and the electron relaxation but only the first depends on the electron thermal polarization since, in the case of the second equation, the electron system is saturated by the MW irradiation. Combining the equations 4.11 and 4.12 we have that

$$\frac{1}{T_1} = \frac{1}{T_{POL}} \left[1 - P_0^2(T)\right] \tag{4.13}$$

which is a relation that combines the two relaxations times. This relation will reveal if there are other relaxation processes involved besides the thermal mixing.
The equations 4.9 and 4.13 play a key role in the analysis presented in the next subsections.

4.2.1 Completely methylated β-CDs

In figures 4.10 and 4.11 the temperature dependence of the spin-lattice relaxation rate and of the inverse of the polarization time of hydrogen and carbon nuclei is presented. Of course, ^{1}H relaxes much faster than ^{13}C nuclei since $\gamma_H > \gamma_C$.

For the coefficients a and b obtained from the power law fit aT^b (figure 4.10) we find, a is almost equal for ^{1}H and ^{13}C while, regarding the b exponent, it is equal to 2.06 and 0.77 for proton and carbon nuclei, respectively. The basic contributions to this power law behaviour arise from the the slow lattice fluctuations described by the glassy dynamics (see eq. 4.8) and other secondary, less effective, nuclear interactions[45].

In fact, the exponent b for ^{1}H has a value close to 2 which underlines the effect of the glassy dynamics being in agreement with the theoretical description assuming a certain distribution of energy barriers, while the exponent b for ^{13}C seems to be associated with its position in the deuterated methyl group and one could consider a different distribution of energy barriers for the rotational motion[44], namely, different dynamics control the carbon relaxation time. Moreover, it is possible that other interactions are relevant, apart

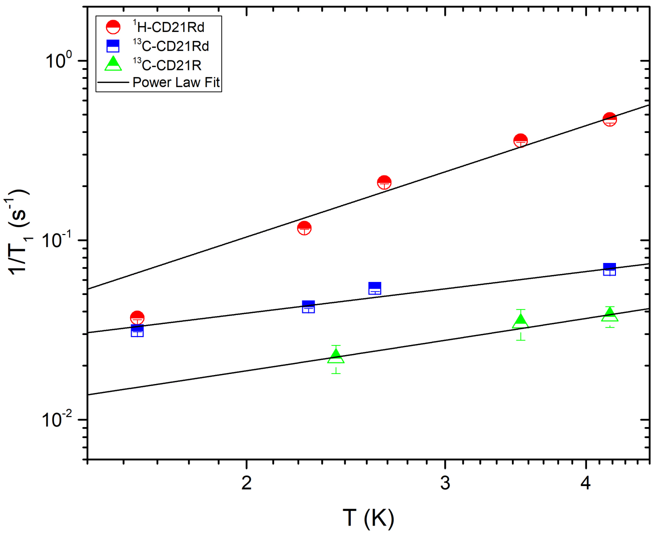

Figure 4.10: Temperature dependence of the nuclear spin-lattice relaxation rate for ^{1}H and ^{13}C nuclei of the completely methylated samples at 3.4 T. The experimental data have been fit according to the power law $y(T) = \mathrm{a}T^b$, with parameters for ^{1}H: a $= 0.025 \pm 0.008 K^{-b}s^{-1}$ and $b = 2.06 \pm 0.23$; for ^{13}C: a $= 0.023 \pm 0.003 K^{-b}s^{-1}$ and $b = 0.77 \pm 0.15$. The green triangles represent the data from the past work Ref. [44] for comparison.

from the hyperfine one. In fact, the magnetic nuclear dipole-dipole interaction among the carbon nuclei and the other nuclear species existing in the samples such as ^{1}H and D nuclei affects the T_1 relaxation time significantly. Indeed the data ^{13}C relaxation rate $\frac{1}{T_1}$ were scaled by the γ^2 of proton but the two curves do not coincide; this is another indication of the existence of additional relaxation processes. In equation 4.14 the terms have been written in such an order that indicates a decreasing strength of the interaction. The first one represents the hyperfine interaction of the ^{13}C nuclei and the electrons while the rest three terms describe the nuclear dipole-dipole interaction between the carbon nuclei and the other nuclear species like D and ^{1}H but also among the carbon nuclei as well. The interaction with deuterium is considered as stronger than with the protons because of the proximity of carbon nuclei with three D atoms in the methyl group, having in mind that the dipole-dipole interaction scales as $\frac{1}{r^3}$.

$$\frac{1}{T_1} = \left(\frac{1}{T_1}\right)_e + \left(\frac{1}{T_1}\right)_{^{13}C-^{2}D} + \left(\frac{1}{T_1}\right)_{^{13}C-^{1}H} + \left(\frac{1}{T_1}\right)_{^{13}C-^{13}C} \tag{4.14}$$

Nevertheless, one of the objectives that we wanted to achieve in this study by the deuteration of the methyl groups, with respect to our past work[44], was

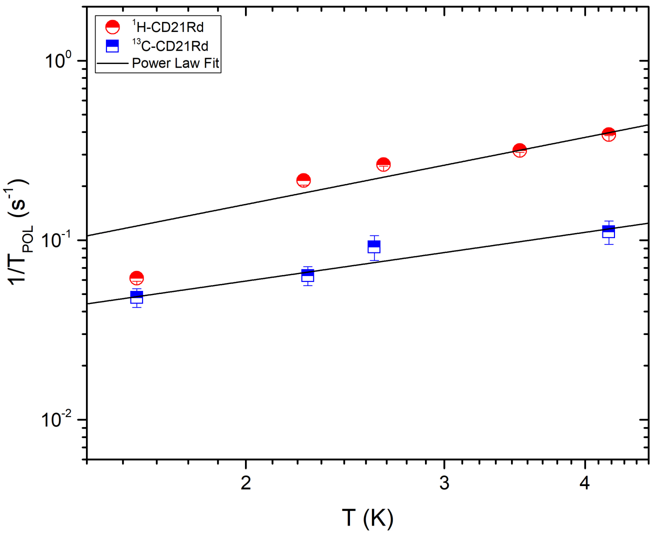

Figure 4.11: Temperature dependence of the inverse of the polarization times for ^{1}H and ^{13}C nuclei of the completely methylated samples at 3.4 T. The experimental data have been fit according to the power law $y(T) = \mathrm{a}T^b$, with parameters for ^{1}H: a $= 0.067 \pm 0.024K^{-b}s^{-1}$ and $b = 1.24 \pm 0.28$; for ^{13}C: a $= 0.026 \pm 0.004K^{-b}s^{-1}$ and $b = 0.98 \pm 0.15$.

to reach higher relaxation times for ^{13}C nuclei making this compound suitable for in-vivo molecular imaging applications. In this aspect, we succeeded by increasing T_1 especially at room temperature by a factor 10 (see section 4.3.1).

In figure 4.11 we have the polarization rate of ^{1}H and ^{13}C nuclei as a function of temperature. We observed a power law behaviour as well, with a lower b exponent in the case of protons, equal to 1.24, while in the case of carbon the b exponent is close to 1. Deviation from the theoretical value could be ascribed to the bottleneck effect where we have an indirect relaxation of the nuclei to the lattice driven by the electron spins fluctuations.

In fact, upon microwave irradiation the relaxation of the nuclei is influenced by the relaxation of the electrons ($\frac{1}{T_{1e}}$)and the time constant of the triple spin mechanism ($\frac{1}{T_{ISS}}$), characterising the thermal mixing[124, 17, 144, 145]. In the case of poor thermal contact between the electrons and the nuclei the ratio of the aforementioned times $\frac{T_{ISS}}{T_{1e}}$ is close to unity, while in the opposite case is significantly smaller than the unity. It is possible that here the deviation of the b exponents from the theoretical prediction is ascribed to a non effective spin diffusion mechanism. Considering the equation 4.13 derived in the thermal mixing framework, that associates $\frac{1}{T_1}$ and $\frac{1}{T_{POL}}$, we have in figure 4.12 that the results seem to be consistent with thermal mixing theory, especially in the case of hydrogen, while in the case of carbon there is a clear deviation.

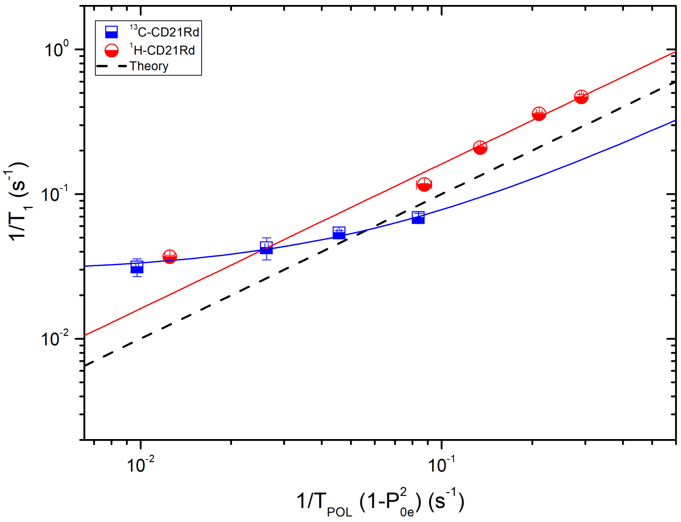

Figure 4.12: Plot of ^{1}H and ^{13}C as a function of $\frac{1}{T_{POL}}\left[1-P_0^2(T)\right]$ for the completely methylated samples at 3.4T. The dashed line represents the theoretical prediction. The experimental data have been fitted with linear function $y = A + Bx$, where A is fixed to zero for hydrogen nuclei, with parameters for ^{1}H: $A = 0$ and $B = 1.52 \pm 0.01$; for ^{13}C: $A = 0.029 \pm 0.004$ and $B = 0.51 \pm 0.09$.

Deviations from the theoretical line originate, also in this case, from a non effective spin diffusion because of the bottleneck effect, that is the indirect energy flow from the nuclei to the lattice, through the hyperfine interaction with the electrons or the incomplete saturation of the ESR spectrum of the radicals associated with the low output power of the microwave source.

A peculiarity of these samples is that the hyperpolarization build up time is only some tens of seconds as we can see for example in figure 4.13, where we have the build up of the nuclear polarization for ^{13}C nuclei at 2.1 K.
The polarization time found here is much faster with respect to the one observed in other systems[137, 146, 147, 148], where it ranges between several minutes and a few hours. This property makes the samples suitable for high resolution DNP-NMR experiments where fast repetition is needed and allows a DNP preparation time which is more suitable for applications.

4.2.2 Hepta- and Mono-TEMPO β-CDs

In this part we compare the DNP performance and the relaxation for different radicals, which are characterised by a different magnetic moment[46]. As regards the spin-lattice relaxation rate and the polarization rate of ^{1}H nuclei for the Hepta- and Mono-TEMPO samples as a function of temperature the plot of the experimental data are reported in figures 4.14 and 4.15 while the parameters of the power law fit provided for the same data are reported in

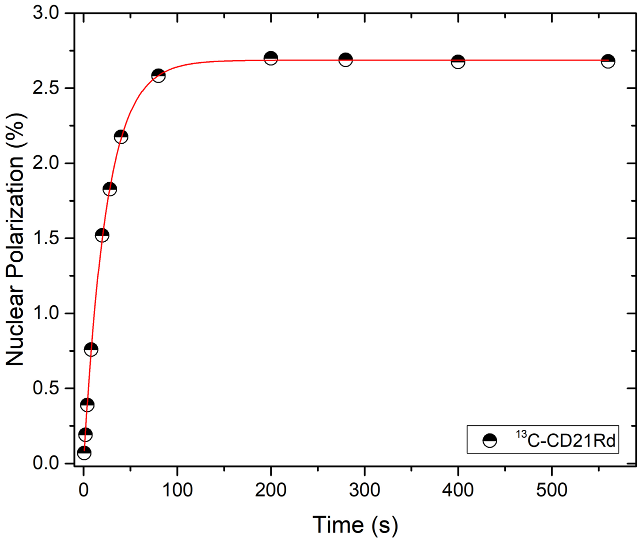

Figure 4.13: polarization build up for ^{13}C nuclei under MW irradiation at 2.1 K and 3.4 T.

tables 4.1 and 4.2 respectively.

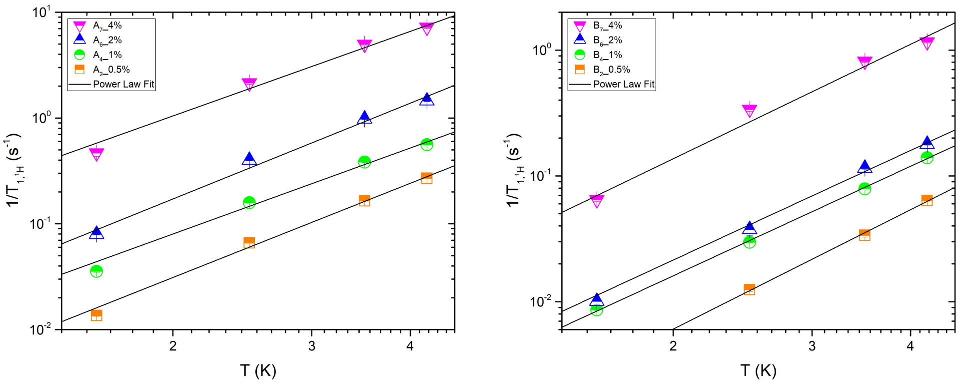

Figure 4.14: Temperature dependence of the relaxation rate for ^{1}H nuclei of the (left) Hepta-TEMPO and (right) Mono-TEMPO samples at 3.4 T. The experimental data have been fitted according to the power law $y(T) = \mathrm{a}T^{b}$; the parameters are reported in table 4.1.

The fit of the experimental data clearly indicates a power law behaviour but characterised by a larger exponent b ranging from 2.6 to 3.2 for all samples. This comes into a disagreement with the theoretical predictions where $b \simeq 2$. It has been noted elsewhere [132] that, although the power law behaviour is a characteristic property of the glassy dynamics, a higher b exponent indicates that the thermal coupling between electron and nuclear spins starts to be relevant. This can affect also the polarization rate $\frac{1}{T_{POL}}$ where the b parameter lies between 1.5 and 2.4, which is not far from the theoretical predictions. On the other hand, coefficient a increases as a function of the concentration up to 2.8 and 2.2 for Hepta- and Mono-TEMPO samples, respectively. We can also notice that the the values of this coefficient for the Hepta-TEMPO samples are an order of magnitude higher than the ones of the Mono-TEMPO samples.

Sample	**a ($\mathbf{K^{-b}s^{-1}}$)**	**b**
A_2 (0.5%)	0.0040 ± 0.0008	3.0 ± 0.2
A_4 (1%)	0.012 ± 0.003	2.7 ± 0.2
A_6 (2%)	0.021 ± 0.005	3.0 ± 0.2
A_7 (4%)	0.17 ± 0.05	2.6 ± 0.2
B_2 (0.5%)	0.0007 ± 0.0001	3.2 ± 0.1
B_4 (1%)	0.0022 ± 0.0001	2.89 ± 0.05
B_6 (2%)	0.0029 ± 0.0007	2.9 ± 0.2
B_7 (4%)	0.017 ± 0.004	3.0 ± 0.2

Table 4.1: Temperature dependence of ^{1}H relaxation rates fitting parameters for $y(T) = \mathrm{a}T^b$.

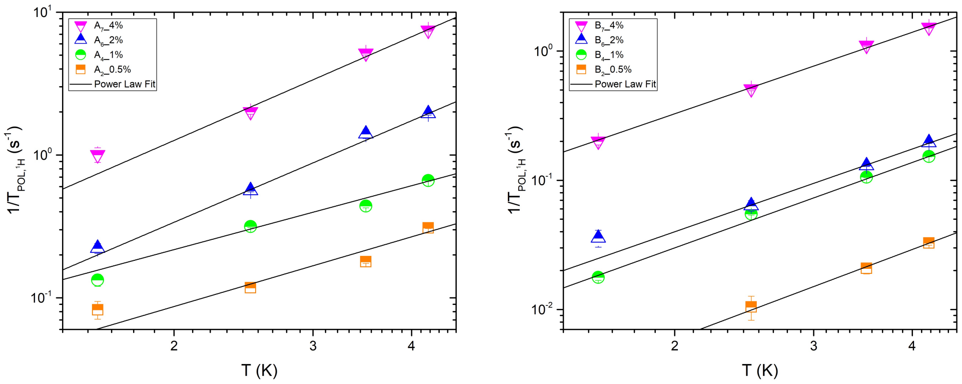

Figure 4.15: Temperature dependence of the inverse of the polarization times for ^{1}H nuclei of the (left) Hepta-TEMPO and (right) Mono-TEMPO samples at 3.4 T. The experimental data have been fitted according to the power law $y(T) = \mathrm{a}T^b$; the parameters are reported in table 4.2.

In order to prove that we are in the thermal mixing regime we plotted the nuclear relaxation time $\frac{1}{T_1}$ as a function of $\frac{1}{T_{POL}}\left[1 - P_0^2(T)\right]$ guided by the equation 4.12. Almost all the experimental data lie closely to the theoretical line (see figure 4.16); it is pointed out that the experiment matches the theoretical findings and the TM theory is suitable to describe these systems. An anomaly was noticed for B_2 (0.5% w/w) sample which indicates a different

Sample	**a ($\mathbf{K^{-b}s^{-1}}$)**	**b**
A_2 (0.5%)	0.03 ± 0.01	1.6 ± 0.4
A_4 (1%)	0.08 ± 0.02	1.5 ± 0.2
A_6 (2%)	0.066 ± 0.006	2.36 ± 0.08
A_7 (4%)	0.24 ± 0.06	2.4 ± 0.2
B_2 (0.5%)	0.0012 ± 0.0002	2.3 ± 0.1
B_4 (1%)	0.0066 ± 0.0006	2.20 ± 0.07
B_6 (2%)	0.009 ± 0.002	2.1 ± 0.2
B_7 (4%)	0.077 ± 0.009	2.09 ± 0.09

Table 4.2: Temperature dependence of ^{1}H inverse polarization times fitting parameters for $y(T) = \mathrm{a}T^b$.

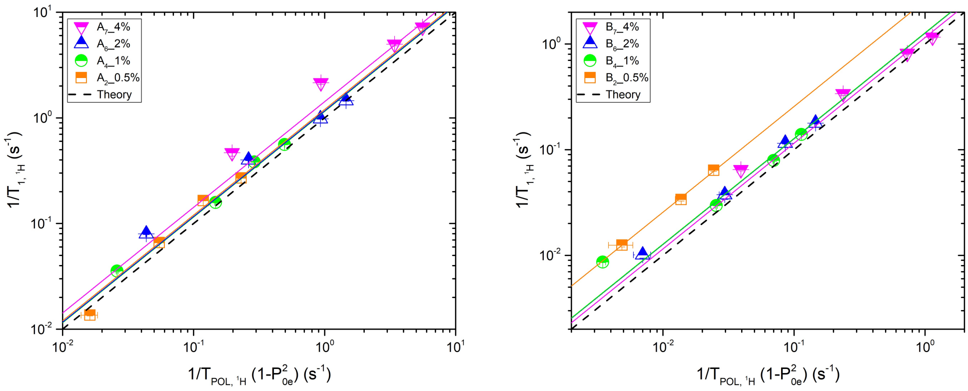

Figure 4.16: Plot of ^{1}H relaxation rate as a function of $\frac{1}{T_{POL}}\left[1 - P_0^2(T)\right]$ for (left) Hepta-TEMPO and (right) Mono-TEMPO samples at 3.4T. The dashed line represents the theoretical prediction. The experimental data have been fitted with linear function $y = A + Bx$, where A is fixed to zero; the parameters are reported in table 4.3.

source of nuclear relaxation other than the one that we have already considered, like the nuclear dipole-dipole interaction especially in samples with a low $\frac{N_e}{N_n}$ ratio.

Sample	**B**
A_2 (0.5%)	1.20 ± 0.09
A_4 (1%)	1.17 ± 0.06
A_6 (2%)	1.2 ± 0.2
A_7 (4%)	1.4 ± 0.2

Sample	**B**
B_2 (0.5%)	2.56 ± 0.005
B_4 (1%)	1.3 ± 0.2
B_6 (2%)	1.27 ± 0.04
B_7 (4%)	1.2 ± 0.1

Table 4.3: Relaxation rate of ^{1}H as a function of $\frac{1}{T_{POL}}\left[1 - P_0^2(T)\right]$ fitting parameters for $y = A + Bx$ where A is fixed to zero.

Upon increasing the radical doping in the samples the concentration of electron spins increases as well. In order to understand better the role of the electrons in the nuclear spin-lattice relaxation we plotted the proton $\frac{1}{T_1}$ as a function of the radical concentration at a given temperature (see figure 4.17). By this figure it seems that the concentration dependence of the relaxation has a power behaviour. Indeed, by fitting the experimental data with the power law $y(C) = mC^f$ for both sample series, we obtain the parameters reported in table 4.4.

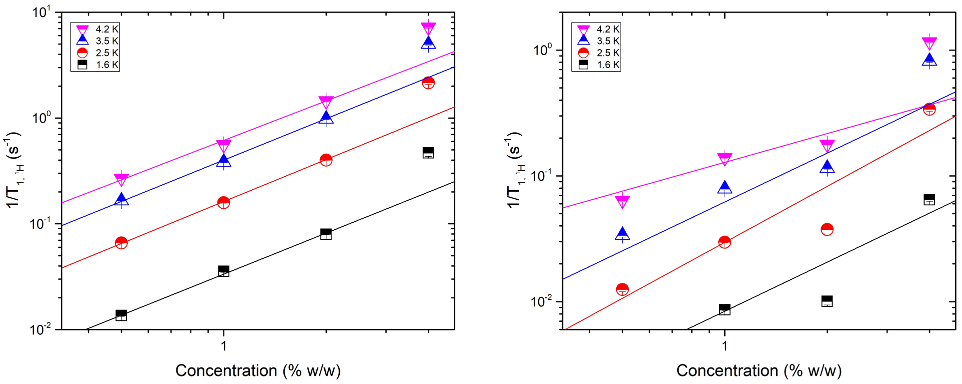

Figure 4.17: Relaxation rate of ^{1}H nuclei as a function of radical concentration of the (left) Hepta-TEMPO and (right) Mono-TEMPO samples at 3.4 T. The experimental data have been fitted according to the power law $y(C) = mC^f$; the parameters are reported in table 4.4.

T (K)	**m (s^{-1})**	**f**
4.2	0.061 ± 0.006	1.2 ± 0.2
3.5	0.40 ± 0.02	1.30 ± 0.09
2.5	0.16 ± 0.009	1.3 ± 0.1
1.6	0.034 ± 0.002	1.29 ± 0.09
T (K)	**m (s^{-1})**	**f**
4.2	0.13 ± 0.02	0.8 ± 0.4
3.5	0.06 ± 0.03	1.3 ± 0.6
2.5	0.030 ± 0.003	1.5 ± 0.3
1.6	0.008 ± 0.002	1.3 ± 0.4

Table 4.4: ^{1}H $\frac{1}{T_1}$ dependence of radical concentration fitting parameters for $y(C) = mC^f$.

It is important here to mention that the data where fitted without the addition of any constant term (intercept) in the power law relation. This means, in a first view, that the nuclear dipolar interaction among ^{1}H nuclei could be disregarded at such low temperatures. This leaves us with the hyperfine interaction as the only one responsible for the nuclear relaxation.

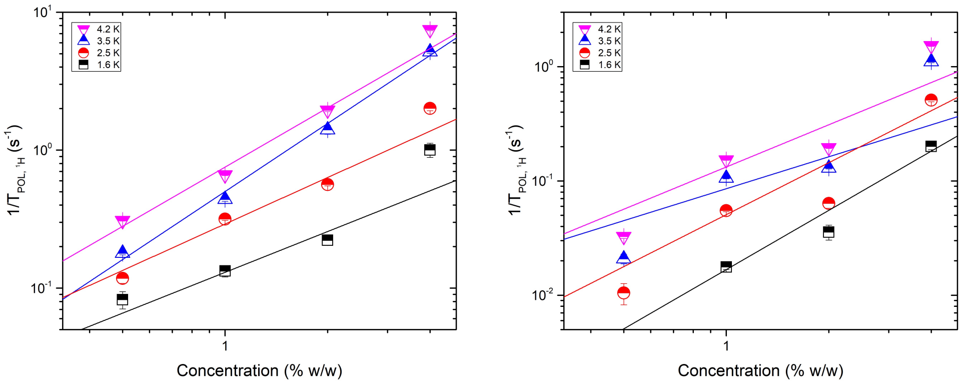

Figure 4.18: Inverse of polarization time of ^{1}H nuclei as a function of radical concentration of the (left) Hepta-TEMPO and (right) Mono-TEMPO samples at 3.4 T. The experimental data have been fitted according to the power law $y(C) = mC^f$; the parameters are reported in table 4.5.

T (K)	**m (s^{-1})**	**f**
4.2	0.75 ± 0.08	1.4 ± 0.2
3.5	0.50 ± 0.04	1.64 ± 0.09
2.5	0.29 ± 0.04	1.1 ± 0.2
1.6	0.13 ± 0.003	1.0 ± 0.4
T (K)	**m (s^{-1})**	**f**
4.2	0.13 ± 0.03	1.2 ± 0.5
3.5	0.09 ± 0.03	0.9 ± 0.9
2.5	0.05 ± 0.01	1.5 ± 0.3
1.6	0.017 ± 0.004	1.7 ± 0.3

Table 4.5: ^{1}H $\frac{1}{T_{POL}}$ dependence of radical concentration fitting parameters for $y(C) = mC^f$.

For $\frac{1}{T_1}$ the f value lies between 1.2 and 1.5 for Hepta-TEMPO but also for Mono-Tempo as well. This value indicates a rather strong dependence of the relaxation rate on the radical concentration and as a consequence, on the hyperfine interaction. For $\frac{1}{T_{POL}}$ we obtained almost the same f values ranging from 0.9 to 1.7 (see figure 4.18 and table 4.5). This is another indication that thermal mixing is indeed the mechanism responsible for the polarization transfer, in other terms that there is a good thermal contact between the nuclear spin ensemble and the electron spin ensemble, the non-Zeeman term.

It seems that the derived f values are not in agreement with the ones derived in other works on DNP substrates[132], where $f \simeq 3$. In order to further investigate this issue we have to take into account equation 4.11 and especially we have to understand the radical concentration dependence. It seems that the concentration of radicals has a double role here; i)in the $\frac{N_e}{N_n}$ ratio and ii) masked in the electron relaxation $\frac{1}{T_{1e}}$. The electron relaxation contains two different sources of relaxation; all the interactions between the electrons and the lattice (phonon, Raman process, Orbach process, low frequency pseudolocal vibrations)[48, 149, 150, 151] and the electron dipolar interaction. Those aspects are summarised in the equation 4.15 where $\left(\frac{1}{T_{1e}}\right)_{lat}$ and $\left(\frac{1}{T_{1e}}\right)_{dip}$ are the lattice and the dipole contribution to the electron relaxation rate.

$$\frac{1}{T_{1e}} = \left(\frac{1}{T_{1e}}\right)_{lat} + \left(\frac{1}{T_{1e}}\right)_{dip} \tag{4.15}$$

The first one is independent of the radical concentration but the second one has a clear dependence on it. So, it seems that this term, which is also related to the ISS process, is quite relevant here for $T \leq 4.2\,K$. At higher temperatures, above 4.2 K, the lattice contribution starts to interfere to the electron relaxation. The electron relaxation rate $\frac{1}{T_{1e}}$ is relevant to the calculation of the nuclear polarization rate as we can see in equation 4.12.

4.2.3 Acetylated β-CDs

To reduce the contribution to the relaxation from the methyl groups we considered the possibility of growing acetylated β-CDs. In figure 4.19 it is shown the temperature dependence of the relaxation rate and the polarization rate for the hydrogen and carbon nuclei respectively.

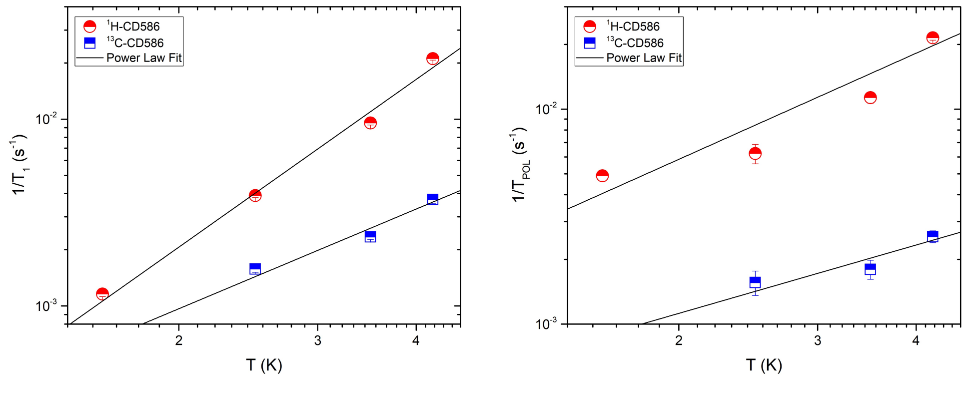

Figure 4.19: Temperature dependence of the nuclear spin-lattice relaxation rate (left) and polarization rate (right) for ^{1}H and ^{13}C nuclei of the acetylated radical doped sample at 3.4 T. The experimental data have been fit according to the power law $y(T) = \mathrm{a}T^{b}$, with parameters for $\frac{1}{T_1}$, ^{1}H: a $= (2.61 \pm 0.07) \times 10^{-4}\,K^{-b}s^{-1}$ and $b = 3.0 \pm 0.2$; and ^{13}C: a $= (3 \pm 2) \times 10^{-4}\,K^{-b}s^{-1}$ and $b = 1.8 \pm 0.4$; for $\frac{1}{T_{POL}}$, ^{1}H: a $= (2 \pm 1) \times 10^{-3}K^{-b}s^{-1}$ and $b = 1.6 \pm 0.4$; and ^{13}C: a $= (5 \pm 3) \times 10^{-4}\,K^{-b}s^{-1}$ and $b = 1.1 \pm 0.5$.

A power law of the form $y(T) = \mathrm{a}T^b$ was used in order to fit the experimental data. For the relaxation rate T_1 the exponents b for ^{1}H and ^{13}C nuclei were equal to 3 and 1.8 respectively. Regarding ^{13}C nuclei the b value is very close to the theoretically predicted b=2 given by the glassy dynamics of the organic substrate, as it is explained in the introduction of the present chapter. In the case of ^{1}H nuclei the b value is higher than the expected one. This is most probably ascribed to the existence of additional leakage processes besides the dominate hyperfine interaction. In fact, the concentration of hydrogen nuclei is high and the dipole-dipole interaction among them, in an intra- and intermolecular level, but also with the carbon nuclei could result in a deviation from the theory. On the other hand, the increase of the polarization rate T_{POL} with the increase of the temperature is lower than in the case of T_1 resulting in a smaller exponent b. Here, spin diffusion is much more effective for ^{1}H nuclei giving a b value close to the theoretical one while for ^{13}C nuclei we have a small deviation from the theoretical value. This is most probably attributed to the small concentration of carbon nuclei and the low coupling among them. Another reason could also be the high concentration of electron spins with respect to the nuclear ones, that make nuclei relax fast, faster than the time needed for an efficient polarization transfer to the inter sample. Both reasons effect the efficiency of spin diffusion and as a consequence the polarization time which depends on the ration of the electron and nuclear concentrations (see equation 4.12).

In order to investigate the mechanism responsible or the polarization transfer from the irradiated electrons to the two nuclear spin systems we plotted the relaxation rate as a function of $\frac{1}{T_{POL}}\left[1 - P_0^2(T)\right]$ for ^{1}H and^{13}C, as we can see in figure 4.20. A linear fit of the form $y = A + Bx$ was used to analyse the data with $A = 0$.

Concerning ^{1}H, we could say that the DNP mechanism in this case is the Thermal Mixing. The experimental data lie very close to the theoretical behaviour predicted by the theory. In fact, by fitting the results, the obtained B value is close to unity as the theory dictates. On the contrary, the experimental data for ^{13}C lie above the theoretical line and the B exponent is equal to 2. This is another indication that the low carbon concentration and the presence of extra relaxation processes prevent an effective spin diffusion, namely an effective DNP throughout the whole sample before relaxation processes start to be effecting.

4.3 Nuclear relaxation and molecular dynamics at higher temperature

It is of great importance, mainly for practical applications, to study the behaviour of the DNP substrates at higher temperatures, close to the human body one. In order to achieve that we measured the relaxation rate $\frac{1}{T_1}$ of

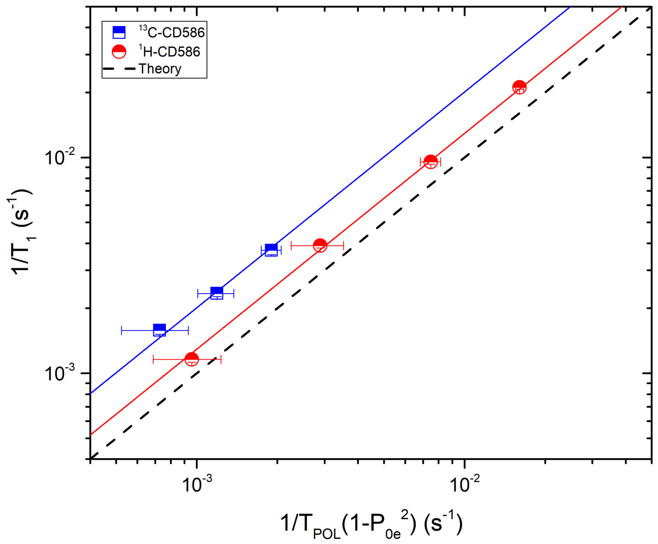

Figure 4.20: Plot of ^{1}H and ^{13}C as a function of $\frac{1}{T_{POL}}\left[1 - P_0^2(T)\right]$ for the acetylated radical doped sample at 3.4T. The dashed line represents the theoretical prediction. The experimental data have been fitted with linear function $y = A + Bx$, where A is fixed to zero, with parameters for ^{1}H: $B = 1.29 \pm 0.03$; for ^{13}C: $B = 2.01 \pm 0.06$.

proton and carbon nuclei as a function of temperature in the temperature range $10 < T < 320$ K. From this study we obtained information about the activated motions in the samples but also for the lifetime of the hyperpolarized state in the radical-free samples at 320 K.

4.3.1 Completely methylated β-CDs

In figures 4.21 and 4.24 we can see the experimental data of the spin-lattice relaxation rate as a function of temperature for carbon and proton nuclei of the radical doped and undoped completely methylated samples CD21Rd and CD21d, respectively.

In figure 4.21 we can detect three different regions[45] related to the frequency of the molecular motions. At lower temperatures ($5\,K \leq T \leq 30\,K$) we have the slow motion regime where the relaxation rate is mainly governed by the the spin fluctuations of the radical electron determined by the glassy dynamics and by the local fast spin fluctuations, the nuclear dipole-dipole interaction between the carbon nuclei and the hydrogen and deuterium nuclei modulated by the glassy dynamics of the amorphous material and the nearly frozen local molecular rotational motions as the ones of the methyl groups (see equation 4.16). The effect of the radicals is strongly visible in this regime increasing the relaxation rate by some orders of magnitude as we can see by the

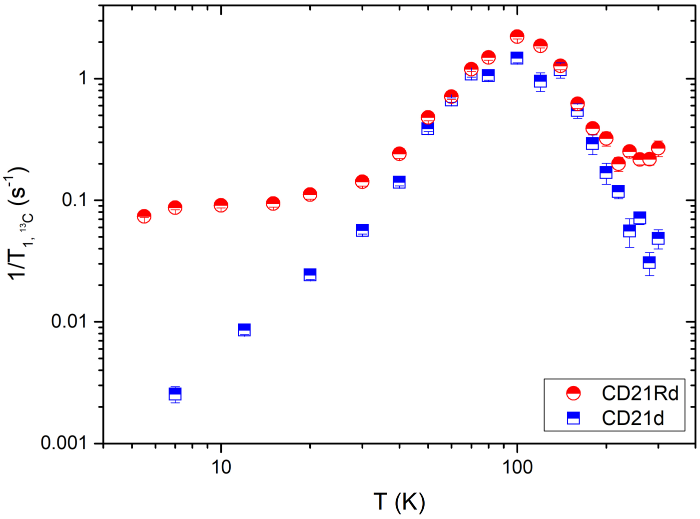

Figure 4.21: Logarithmic representation of the temperature dependence of the ^{13}C nuclear spin-lattice relaxation rate for the completely methylated samples with (CD21Rd) and without (CD21d) radicals in a 3.4 T magnetic field.

split of the two curves.

$$\left(\frac{1}{T_{1,n}}\right) = \left(\frac{1}{T_1}\right)_S^{fast\,fluct.} + \left(\frac{1}{T_1}\right)_S^{glassy\,dyn.} + \left(\frac{1}{T_1}\right)_I^{glassy\,dyn.} + \left(\frac{1}{T_1}\right)_I^{mol.\,rot.} \tag{4.16}$$

In this temperature range, the relaxation rate of both nuclei for the samples CD21d and CD21Rd has a power law behaviour (figure 4.22), characteristic of the glassy dynamics. Compared to the values of the a and b parameters at low temperatures (see figure 4.10) we have higher a values, related to the higher amplitude of local field fluctuations and lower b values for the doped sample which suggests a change of the barrier landscape at higher temperature. Following the discussion of section 4.2.2 this means that at higher temperature we have additional contributions (see eq. 4.15) to the electron relaxation rising from the lattice.

At intermediate temperatures ($40\,K \leq T \leq 200\,K$) we observe the presence of a common peak around 100 K. Especially in the case of carbon (figure 4.21) the two peaks coincide and the effect of the radicals on the relaxation rates vanishes. This suggests that these peaks, located at the same temperature, are most probably related to the presence of activated molecular motions, presumably the rotation of the CD$_3$ groups. Taking into account the broadening of the peaks, we used the BPP formula (eq. 2.4) to analyse the data, considering a rectangular distribution of the activation energy barrier E_A of total width 2Δ, so that[43]

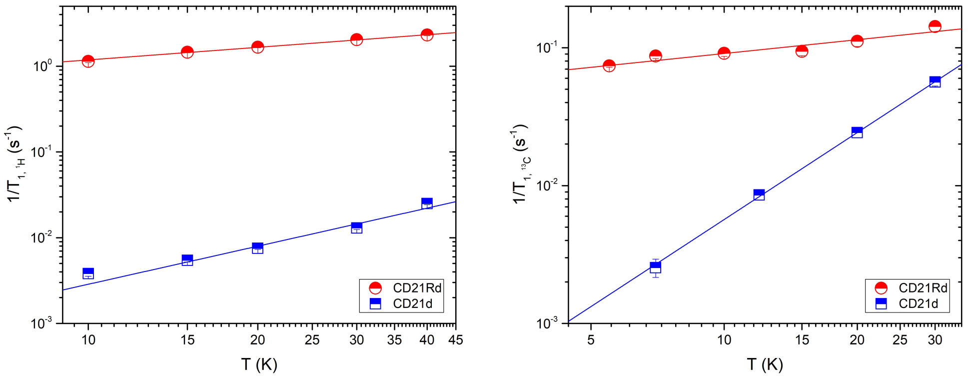

Figure 4.22: Temperature dependence of the nuclear relaxation rates for ^{1}H (left) and ^{13}C (right) nuclei of the completely methylated samples at 3.4 T. The experimental data have been fit according to the power law $y(T) = \mathrm{a}T^b$, with parameters for ^{1}H: CD21d, a $= (10 \pm 5) \times 10^{-5} K^{-b} s^{-1}$ and $b = 1.5 \pm 0.2$; CD21Rd, a $= 0.39 \pm 0.02 K^{-b} s^{-1}$ and $b = 0.49 \pm 0.02$; for ^{13}C: CD21d, a $= (4.5 \pm 0.4) \times 10^{-5} K^{-b} s^{-1}$ and $b = 2.10 \pm 0.03$; CD21Rd, a $= 0.042 \pm 0.004 K^{-b} s^{-1}$ and $b = 0.33 \pm 0.05$.

$$\begin{aligned} \frac{1}{T_{1n}} \cong \frac{\gamma^2}{2} \frac{< \Delta h_\perp^2 >}{\omega_n} \frac{T}{\Delta} \Bigg\{ & \arctan \left[\omega_n \tau_0 \exp \left(\frac{E_A + \Delta}{T} \right) \right] \\ & - \arctan \left[\omega_n \tau_0 \exp \left(\frac{E_A - \Delta}{T} \right) \right] \Bigg\}. \end{aligned} \tag{4.17}$$

From the fitting of the data with this variation of the BPP formula we obtained, among others, the values of energy barriers E_A. According to literature[152], these values correspond indeed to the rotation of the deuterated methyl groups CD$_3$. This activated rotation is the dominant nuclear relaxation mechanism in this temperature range since the two peak almost coincide regardless the effect of the radicals, while at low and high temperatures the effect of the radical is clear. From the analysis we also recovered the value of the amplitude of the fluctuating field $\langle \Delta h_\perp^2 \rangle$ which is of the order of the Gauss, characteristic value of the dipolar field of the nuclei.

At higher temperatures ($220\,K \leq T \leq 320\,K$) one observes (figure 4.24) a split of the two curves since in the sample with radicals there is an additional contribution to the relaxation from the electron dynamics. The ^{13}C relaxation time at 300 K of the sample CD21d (without radicals) is 33 s, indicating the lifetime of the hyperpolarized state. This is a sufficiently long time for some applications including the in-vivo molecular imaging.

In figure 4.24 the relaxation rate of ^{1}H nuclei as a function of temperature is presented. The contribution of the radicals to the nuclear relaxation is evident since the curve of the CD21Rd sample lies well above the curve of

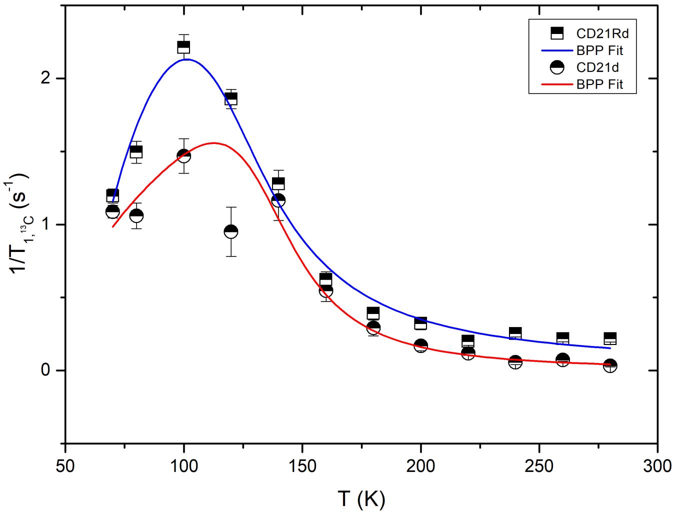

Figure 4.23: Plot of the temperature dependence of the relaxation rate $\frac{1}{T_1}$ of the ^{13}C nuclei fitted with the modified BPP function for the samples with (CD21Rd) and without (CD21d) radical. By the fitting parameters we have for the sample without radical that $E_A = (558 \pm 78)K$, $\Delta = (264 \pm 52)K$, $\tau_0 = (1.1 \pm 0.8) \times 10^{-11} s$ and $\langle \Delta h_\perp^2 \rangle = (5.8 \pm 0.4) \times 10^{-8} T^2$, while for the sample with radical we have $E_A = (733 \pm 93)K$, $\Delta = (388 \pm 60)K$, $\tau_0 = (1.9 \pm 1.4) \times 10^{-12} s$ and $\langle \Delta h_\perp^2 \rangle = (5.6 \pm 0.4) \times 10^{-8} T^2$.

the non doped sample. Around 100 K we do not see a clear peak like before, just a small bump instead. Carbon nuclei are more sensitive to CD_3 rotational motions than to glass transition, while for ^{1}H it is the opposite. Proton relaxation is less sensitive to the rotation of the methyl groups since they are less coupled with the deuterium atoms than the ^{13}C nuclei. What we observe here (figure 4.24) is a peak around 250 K for the doped sample (CD21Rd) and a clear increase of the relaxation rate for the non doped sample (CD21d) that indicated a peaks at a higher temperature. This can be either a thermal effect that is not present in the case of the ^{13}C or the contribution of an additional relaxation phenomenon.

The temperature dependence of the ^{1}H NMR linewidth (figure 4.26,left) is characterised by a sharp drop, above 200 K, for both samples. A sharp change of linewidth is more likely to describe a first order transition rather than a progressive slowing down of the molecular motions, so the peaks in figure 4.24 are most probably related to a glass transition[153], although it is difficult to say if it is really a first order transition without further investigation. The fact that these peaks are positioned at different temperatures is associated with the different stoichiometry of the samples which can slightly affect the lattice dynamics. In figure 4.25 we have two representative ^{1}H NMR spectra at 10 K

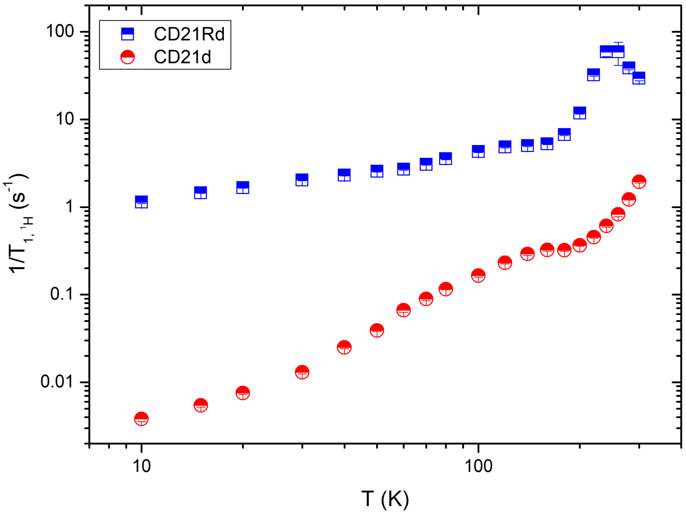

Figure 4.24: Logarithmic representation of the temperature dependence of the ^{1}H nuclear spin-lattice relaxation rate for the completely methylated samples with (CD21Rd) and without (CD21d) radicals in a 1.5 T magnetic field.

and 300 K that can be described by simple gaussian and lorentzian functions, respectively, while they do not present any particular internal structure.

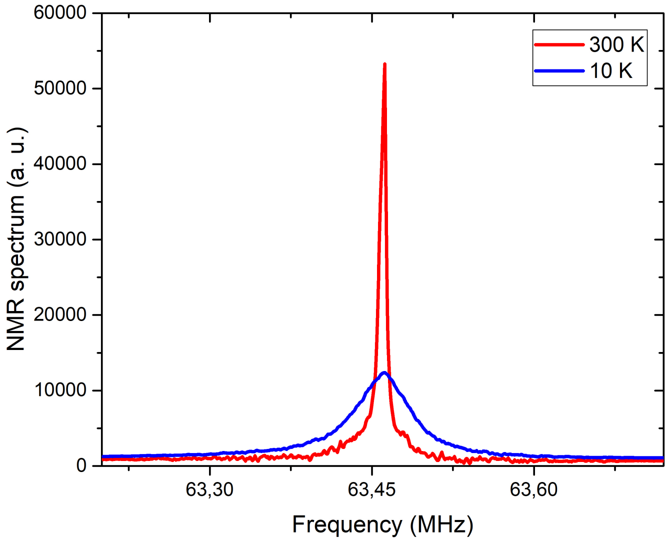

Figure 4.25: ^{1}H NMR spectrum of the radical doped completely methylated sample CD21Rd as a function of the NMR frequency at 10 K and 300 K in a 1.5 T magnetic field.

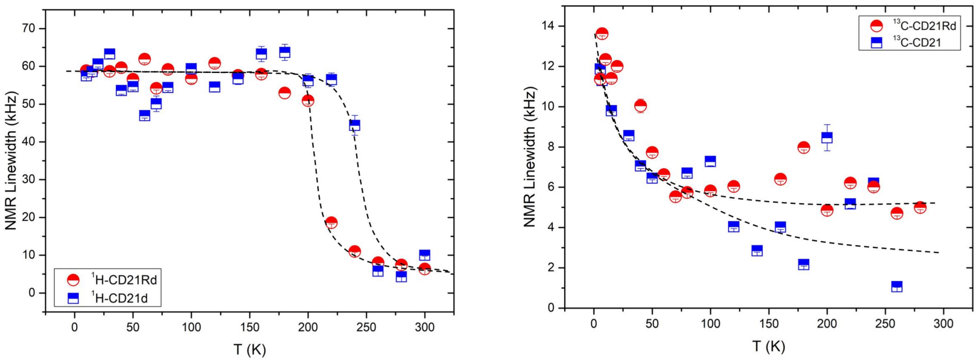

Figure 4.26: Temperature dependence of the NMR linewidth for both doped and non doped samples for ^{1}H nuclei in a 1.5 T magnetic field (left) and ^{13}C nuclei in a 3.4 T magnetic field (right).

In figure 4.26(right) we have the temperature dependence of the ^{13}C NMR linewidth for the doped and the undoped samples. At high temperatures the NMR linewidth is constant while around 100 K, where the peak in $\frac{1}{T_1}$ associated with the molecular rotations (figure 4.21), we detect a gradual broadening upon cooling down due to the slowing down of the motions.

For a complete picture of the high temperature NMR study we performed some measurements of the ^{13}C spin-spin relaxation time of the samples CD21d and CD21Rd, at different temperatures. In particular, in figure 4.27 we have the experimental data and the analysis of the relaxation rate $\frac{1}{T_2}$ as a function of time for both samples at T=70 K (left) and for the sample CD21d without radicals at 70 K and 300 K (right). Hahn echo sequence was used to measure the $\frac{1}{T_2}$ relaxation which was characterised by an exponential decay.

The results of the T_2 study indicate that in presence of radicals both relaxation times T_1 and T_2 are affected and more specifically they become shorter (figure 4.27,left). In fact this effect on the T_2 times results into an additional contribution to the linewidth of NMR spectrum that leads to a further shortening of the spin-lattice relaxation time T_1. On the other hand, if one considers the sample without radicals (CD21d), it can be noticed that the rotation of the methyl groups affects the spin-spin relaxation as we can see in figure 4.27(right), where $T_{2,CD21Rd}^{70K} < T_{2,CD21d}^{300K}$.

4.3.2 Hepta- and Mono-TEMPO β-CDs

It is crucial for the practical application of the Hepta- and Mono-TEMPO cyclodextrin macromolecules to study them at high temperatures, specifically close to the human body one. Here, the high temperature ^{1}H nuclear relaxation study of these samples up to 320 K is presented (figures 4.28 and 4.29).

In those figures we can observe some common behaviours. First of all, the effect of the radical on the proton relaxation rate is clear; as the concen-

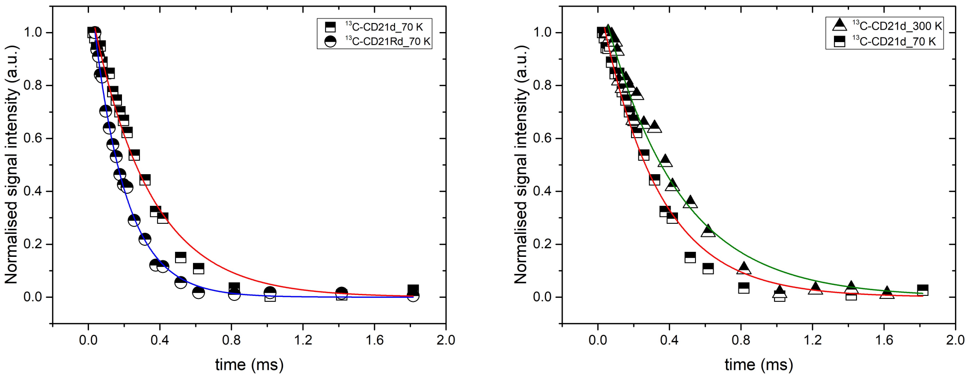

Figure 4.27: Comparison of the time dependence of the normalised NMR Hahn echo signal intensity as a function of the decay between $\frac{\pi}{2}$ and π RF pulses for ^{13}C nuclei in the completely methylated samples with and without radicals at different temperatures. The experimental data where fitted with the formula $y = y_0 + Ae^{-\frac{1}{T_2}}$ where $y_0 = 0$. For the relaxation times we have: (left) $T_{2,CD21d}^{70K} = (0.32 \pm 0.02)\, ms$, $T_{2,CD21Rd}^{70K} = (0.184 \pm 0.004)\, ms$ and (right) $T_{2,CD21d}^{300K} = (0.41 \pm 0.02)\, ms$.

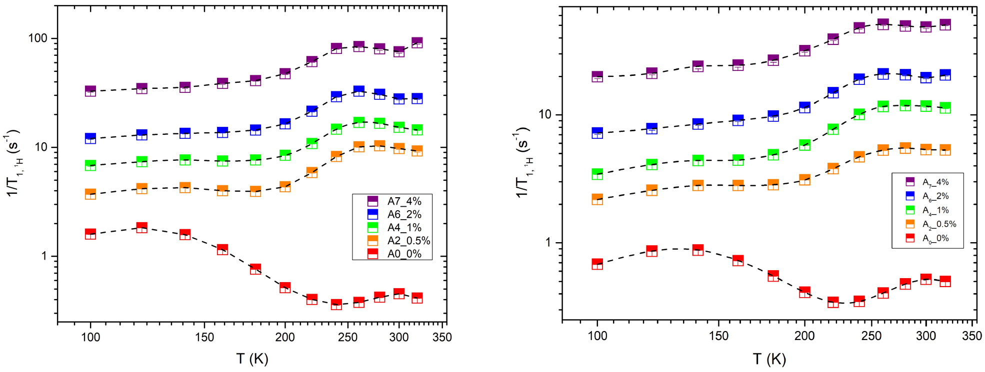

Figure 4.28: Logarithmic representation of the temperature dependence of the ^{1}H nuclear spin-lattice relaxation rate for the Hepta-TEMPO samples doped with different concentrations of radicals in a 3.4 T (left) and 7 T (right) magnetic field. The results of the undoped sample (A_0) are also depicted. Black dashed lines were added as guides to the eye. The labels represent the radical concentration of each sample.

tration of the radical (i.e. paramagnetic centres) increases the relaxation time decreases. The spin lattice relaxation becomes faster because of the increasing hyperfine interaction between the radicals and the ^{1}H nuclei.

We also observed a power law behaviour of the nuclear relaxation rate in the temperature range $20\, K \leq T \leq 80\, K$ (see figure 4.30) for the sam-

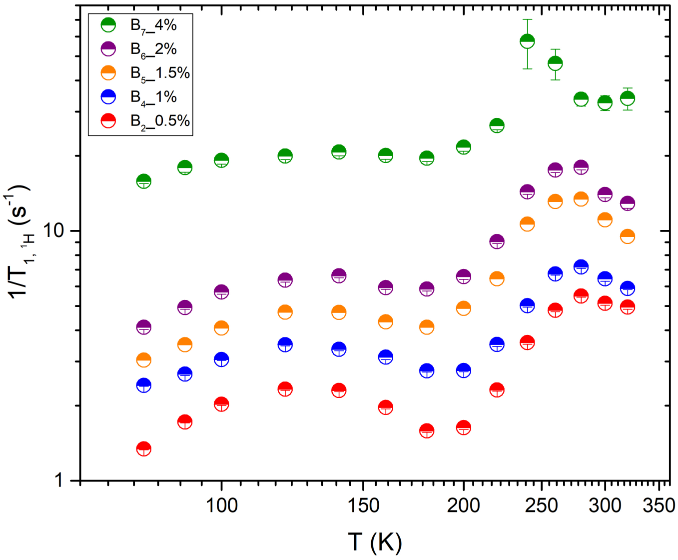

Figure 4.29: Logarithmic representation of the temperature dependence of the ^{1}H nuclear spin-lattice relaxation rate for the Mono-TEMPO samples doped with different concentrations of radicals in a 3.4 T magnetic field. The labels represent the radical concentration of each sample.

ples A_0, A_4 and A_6 (0%, 1% and 2% Hepta-TEMPO radical concentration, respectively) which is most probably ascribed to the glassy dynamics. Here we obtained similar b values for the samples doped with radicals ($b \simeq 0.5$) while for the undoped one we had a much higher b value equal to 2.8, fact that underlines the effect of the radicals to the nuclear relaxation by changing the lattice glassy dynamics. The value a (slope) change substantially with the increase of radical concentration, as expected; at zero radical concentration parameter a is five orders of magnitude lower while for 1% and 2% is $a_{A_4} = 0.52 \pm 0.05 K^{-b} s^{-1}$ and $a_{A_6} = 1.2 \pm 0.1 K^{-b} s^{-1}$ respectively. In comparison with the results at lower temperature ($1.6\,K \leq T \leq 4.2\,K$) we see that the b exponent is about 6 times lower while the a values are significantly higher (see table 4.1); we have a change in the distribution of the local dynamics of the amorphous glass matrix that starts to interact with the free electrons altering the electron relaxation times and consequently the nuclear relaxation[44]. It is worth to mention that the high temperature a and b parameters of the undoped A_0 sample match with the parameters of the doped samples at lower temperatures underling the dominant effect of the glassy dynamics at low temperatures.

In order to investigate this point we plotted the ^{1}H relaxation times of both samples series as a function of the concentration at higher temperatures (figure 4.31). The experimental data were fitted with the power law $y(C) = mC^f$ and the results are reported in table 4.6.

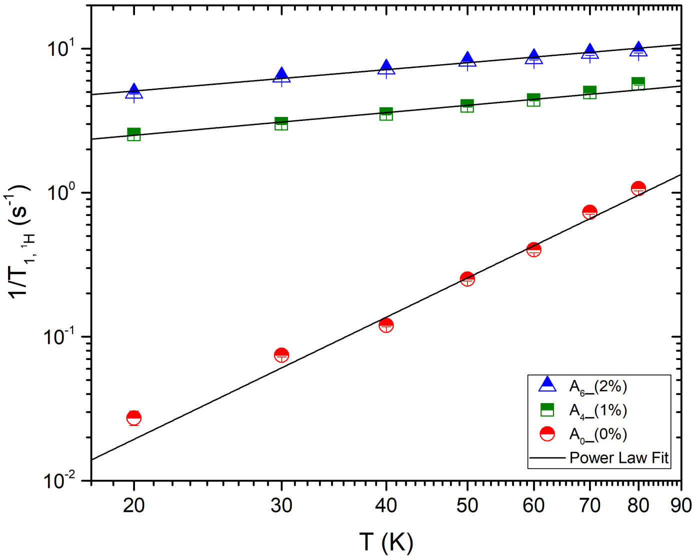

Figure 4.30: Temperature dependence of the inverse of the polarization times for ^{1}H nuclei of the A_0, A_4 and A_6 samples at 3.4 T. The experimental data have been fitted according to the power law $y(T) = \mathrm{a}T^b$. For A_0: $\mathrm{a} = (4 \pm 3) \times 10^{-6} K^{-b} s^{-1}$ and $b = 2.8 \pm 0.2$; A_4: $\mathrm{a} = 0.52 \pm 0.05 K^{-b} s^{-1}$ and $b = 0.52 \pm 0.03$; A_6: $\mathrm{a} = 1.2 \pm 0.1 K^{-b} s^{-1}$ and $b = 0.49 \pm 0.03$. The labels represent the radical concentration of each sample.

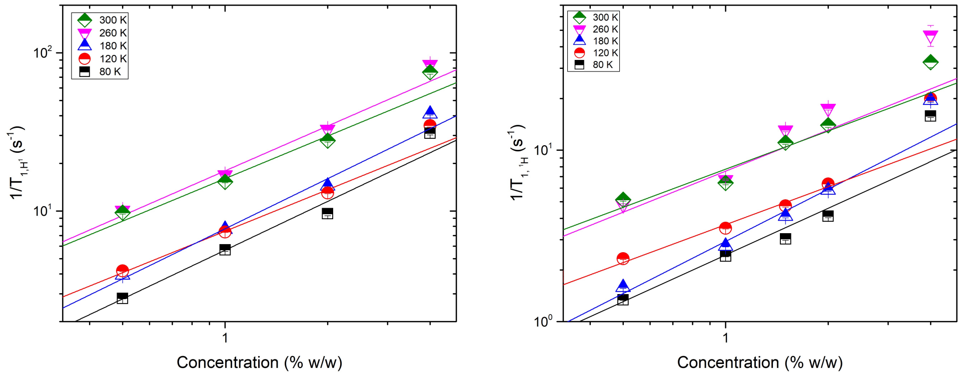

Figure 4.31: Relaxation rate of ^{1}H nuclei as a function of radical concentration of the (left) Hepta-TEMPO and (right) Mono-TEMPO samples at higher temperatures and 3.4 T. The experimental data have been fitted according to the power law $y(C) = mC^f$; the parameters are reported in table 4.6.

For both sample series we have a common behaviour as far as the fitting parameters are concerned. Parameter m increases with the temperature and

T (K)	**m (s^{-1})**	**f**
80	5.7 ± 0.2	1.02 ± 0.07
120	7.5 ± 0.3	0.87 ± 0.07
180	7.7 ± 0.4	1.05 ± 0.08
260	17.9 ± 0.9	0.93 ± 0.09
300	16 ± 1	0.9 ± 0.2

T (K)	**m (s^{-1})**	**f**
80	2.5 ± 0.2	0.9 ± 0.1
120	3.7 ± 0.2	0.7 ± 0.1
180	2.9 ± 0.2	1.0 ± 0.1
260	7.5 ± 0.7	0.8 ± 0.2
300	7.7 ± 0.6	0.7 ± 0.2

Table 4.6: ^{1}H $\frac{1}{T_1}$ dependence of radical concentration fitting parameters for $y(C) = mC^f$ at higher temperature of Hepta- (left) and Mono-TEMPO (right) samples.

parameter f lies between $0.7 \leqslant f \leqslant 1.05$. As expected the m values are much higher than at lower temperature while f values are reduced (see table 4.4). This is a clear indication that, at higher temperature, the electron relaxation is affected by the local lattice excitations of the material which are activated. The electron relaxation rate $\frac{1}{T_{1e}}$ (see eq. 4.15) increases and this modulates the electron-nucleus hyperfine interaction.

Furthermore, two peaks are displayed, one at lower temperature (around 125 K) and the other at high temperature (around 225 K). Having in mind the results of the previous subsection, this first peak is probably ascribed to the rotation of the methyl groups in the sample while the second one depicts the glass transition[45, 152, 153].

Following the same strategy as before, we tried to fit the experimental data with two different functions: the BPP function (eq. 4.17) and a variation of it that is the sum of two BPP functions and a power law function. The second one was used to fit both, the peak of the molecular rotations and the peak of the glass transition and to take under consideration the paramagnetic behaviour of the radical at higher temperature (figure 4.32).

From the value of the activation energy of the sample A_{0}–(0%) we can verify that this peak is indeed ascribed to the rotation of the methyl groups. For the Hepta-TEMPO samples (figure 4.29) this peak is clearly visible only for the undoped sample while for higher concentrations it is possible to define only its relative position by a slight difference in the slope. The effect of radicals on the glass transition peak is strong, giving rise to a broad peak that superimposed to the first one making the analysis difficult. During the transition the radicals are displaced trying to reorganise themselves in more favourable energetically positions. This relative motion is sensed by the the ^{1}H nuclei decreasing their relaxation time. The higher the radical concentration the more significant is the displacement of the peak towards lower temperatures.

The values of the activation energy of the samples A_{4}–(1%) and A_{6}–(2%), as far as the peak at higher temperature is concerned, is very close to the value found in the literature[154]. So it is safe to say that this peak is indeed ascribed to the glass transition. Deviations from this value are given by the different stoichiometry of the samples and the different thermal processing of

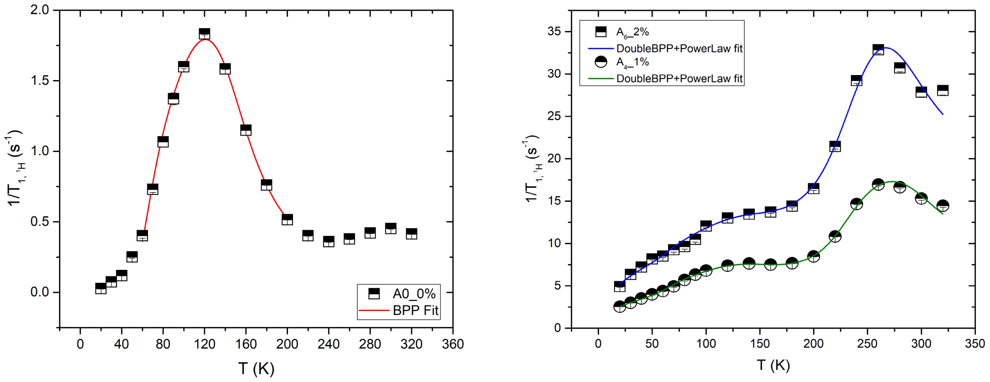

Figure 4.32: (left) Plot of the temperature dependence of the relaxation rate T_1 of the ^{1}H nuclei fitted with the BPP function for the A_0_(0%) sample. By the fitting parameters we have for the activation energy $E_A = (638 \pm 10)K$. (right) Plot of the temperature dependence of the relaxation rate T_1 of the ^{1}H nuclei fitted with the modified BPP function for the A_4_(1%) and A_6_(2%) samples. For the small bump on the right side (related to the rotation of the methyl groups) the value of E_A of the A_0 sample was kept fixed. By the fitting parameters we have that the activation energies are $E_A = (2800 \pm 500)K$ and $E_A = (2284 \pm 750)K$ respectively that corresponds to the glass transition.

the material.

It is worth to mention that the effect of the radicals in the proton relaxation rate is different between the Hepta- and the Mono-TEMPO sample. As we can see in figures 4.28 and 4.29, in the case of the Hepta-TEMPO sample the peak associated with the rotation of the methyl groups is overcome rapidly in the presence of the radicals and becomes difficult to define it. On the other hand, in the case of the Mono-TEMPO the peak remains clearly visible. This is due to the fact that the Hepta-TEMPO radicals make the relaxation of the nuclei much faster and as a result the contribution to the relaxation of the rotation of the methyl groups is not well sensed by the nuclei. In fact, we exploit the modified BPP function to study this high temperature peak properties for the Hepta- and Mono-TEMPO samples with different radical concentrations. The values of the fitting parameters are shown in table 4.7.

From the aforementioned results we can extract the following observations: i) the activation energy of the glass transition depends on the radical concentration. The higher the concentration the lower the activation energy, fact that can be seen also in figures 4.28 and 4.29 by the relative displacements of the peak, ii) the width of the peak depends on the concentration as well, noticing that the lower the concentration the broader the peak becomes and iii) the fluctuations of the local magnetic field at the site of nuclei because of the reorganisation of the molecular structure in the glass transition are more intense with respect to the activation of the rotation of the methyl groups while the

Sample	**E (K)**	**Δ (K)**	$< \mathbf{\Delta h_\perp^2} >$ **($\mathbf{T^2}$)**	**τ_0 (s)**
A_2_(0.5%)	3500 ± 900	600 ± 200	$(2.0 \pm 0.2) \times 10^{-6}$	$(2 \pm 5) \times 10^{-14}$
A_4_(1%)	2800 ± 500	400 ± 100	$(2.2 \pm 0.1) \times 10^{-6}$	$(2 \pm 3) \times 10^{-13}$
A_6_(2%)	2300 ± 750	200 ± 300	$(2.8 \pm 0.3) \times 10^{-6}$	$(1 \pm 3) \times 10^{-12}$
A_7_(4%)	2200 ± 900	190 ± 40	$(4.52 \pm 0.09) \times 10^{-6}$	$(1.4 \pm 0.1) \times 10^{-12}$
B_2_(0.5%)	3600 ± 1600	600 ± 300	$(1.6 \pm 0.2) \times 10^{-6}$	$(2 \pm 1) \times 10^{-14}$
B_4_(1%)	3700 ± 1300	550 ± 200	$(1.7 \pm 0.2) \times 10^{-6}$	$(1 \pm 6) \times 10^{-14}$
B_6_(2%)	3700 ± 2400	500 ± 400	$(2.6 \pm 0.6) \times 10^{-6}$	$(0.7 \pm 6) \times 10^{-14}$
B_7_(4%)	3200 ± 2900	-	$(3 \pm 1) \times 10^{-6}$	$(0.3 \pm 4) \times 10^{-14}$

Table 4.7: Fitted parameters for Hepta- and Mono-TEMPO samples according to the modified BPP function.

correlation time of the interaction was shorter by two orders of magnitude.

The temperature dependence of the NMR linewidth for the samples A_0, A_4 and A_6 is reported in figure 4.33. In accordance with the temperature dependence of ^{1}H relaxation rate (figure 4.28) we observed an abrupt decrease of the linewidth around 100 K which is ascribed to the rotation of the methyl groups while around 220 K we have a well defined change of slope attributed to the glass transition. Notably, NMR linewidth seems rather independent of the radical concentration, while usually, the higher the radical concentration it is the broader the linewidth becomes. Apart from this, we also observed that upon cooling, around 220 K and 100 K, the radical dependence of the linewidth changes. These rather odd features indicate that there is a dependence of the NMR linewidth from the cooling/heating rate[155]. When the cooling rate is fast the radicals remain at random sites and orientations while when it is slower they reorganise themselves in more ordered sites. This may apply changes in the local dipole interactions among the nuclei affecting in each turn the T_2 relaxation times and the NMR linewidth.

In order to explore more in detail the differences in the effect of the two types of radicals, we performed continuous wave (CW) EPR experiments on the Hepta-TEMPO samples at two different temperatures, 295 K and 120 K, to be compared with Mono-TEMPO EPR spectra in the literature[46, 48, 156] (see figure 4.34). Not surprisingly, we obtained a broad signal (~65 G peak to peak) where the resonance field and the position of the peaks is independent of the radical concentration and temperature. The effect of the radicals can be seen in the change of the EPR lines area which increases accordingly to the increase of their concentration.

The peculiar aspect here is that, according to the literature [156], the usual EPR spectrum of simple TEMPO radical (Mono-TEMPO) is the presence of three well resolved lines while in this case we have three superimposed ones. The number of the lines originates from the hyperfine interaction between the free electron, which is strongly localised in the nitroxide bond (see section 1.3), and the ^{14}N nucleus with nuclear spin equal to 1 (figure 4.35). The super-position of the peaks is most probably associated with the mutual

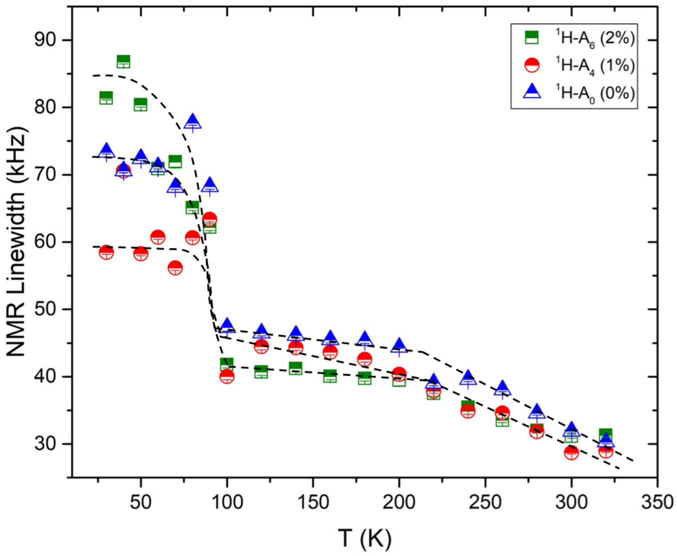

Figure 4.33: Temperature dependence of the NMR linewidth of ^{1}H nuclei for the samples A_0, A_4 and A_6 in a 3.4 T magnetic field. Black dashed lines were added as guides to the eye. The labels represent the radical concentration of each sample.

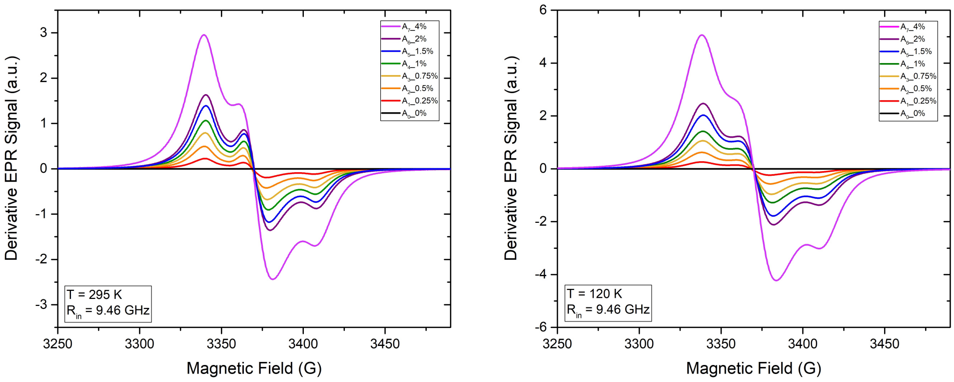

Figure 4.34: Normalized EPR signal as a function of magnetic field for the Hepta-Tempo samples at 295 K (left) and 120 K (right) temperature. The labels represent the radical concentration of each sample.

intramolecular interaction of the electron spins in the seven centres moieties since they are positioned at short distances in the small rim of the cyclodextrin molecule.

In fact, this system presents intramolecular interactions of antiferomagnetic (AFM) nature[46]. The Hepta-TEMPO molecule has a favourable configuration where one of the TEMPO units is at the center of the molecule while

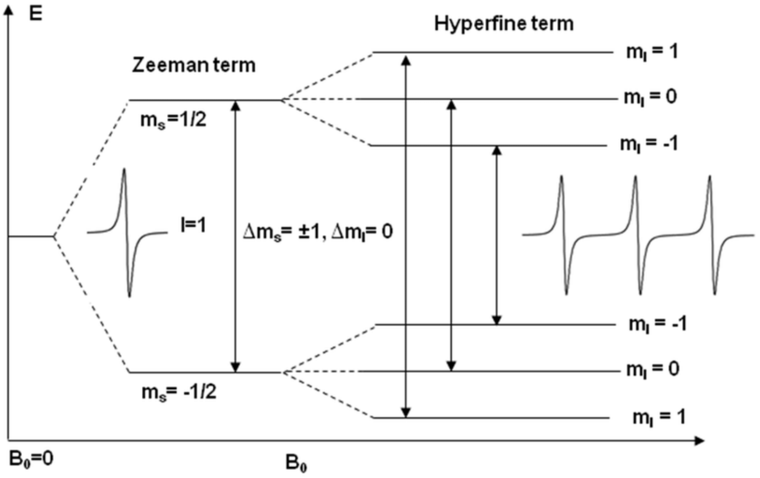

Figure 4.35: Energy level diagram of TEMPO radical as a function of the magnetic field. The electron Zeeman split and the addition of the hyperfine interaction with the nuclear spin $I = 1$ nitrogen nucleus is presented. Figure adapted from *Sahu et al.* [157].

the others remain around it forming a somehow distorted ring molecule. The interaction between the electron spins is much larger than the hyperfine interaction of the N nuclei and as a result we observe these superimposed peaks. This interaction of the electrons affects also the effective magnetic moment (μ_{eff}) that instead of a theoretical value equal to $7\mu_B$ (of a non interacting system) is reduced down to $4.2\mu_B$. Nevertheless, the effective magnetic moment of the Hepta-TEMPO per molecule is still higher than the one of the Mono-TEMPO ($1.7\mu_B$)[46]. Since relaxation rate is proportional to μ_{eff}^2 the Hepta-TEMPO radicals make the ^{1}H nuclei relax much faster than the Mono-TEMPO radicals and that is why we see the different effect in figures 4.28 and 4.29.

The value of the effective magnetic moment of Hepta-TEMPO suggests an electron spin value higher than $\frac{1}{2}$. By the formula $\mu_{eff} = g_e\sqrt{S\left(S+1\right)}\mu_B$, where g_e is the electron gyromagnetic ration, S is the electron spin and μ_B is Bohr magneton, one can find that the electron spin should be equal to $\frac{3}{2}$. The Hepta-TEMPO electron is characterised by four Zeeman split energy levels ($\pm\frac{1}{2}$, $\pm\frac{3}{2}$) and due to the hyperfine interaction with the N nuclei ($I = 1$) each one of these energy levels should be further split into $2I + 1$ lines. Since the Zeeman splitted electron levels are equally spaced and because of the selection rules $\Delta m_I = \pm 1$ and $\Delta m_S = 0$, we have 12 possible transitions that overlap with each other. This results into 3 superimposed broad EPR lines as we can see in figure 4.34. By the second integration of the EPR signals we obtained the area of the signal (figure 4.36,left) while by the equation 2.81 we calculated the number of spins per milligram for a spin value $S = \frac{3}{2}$ (figure 4.36,right).

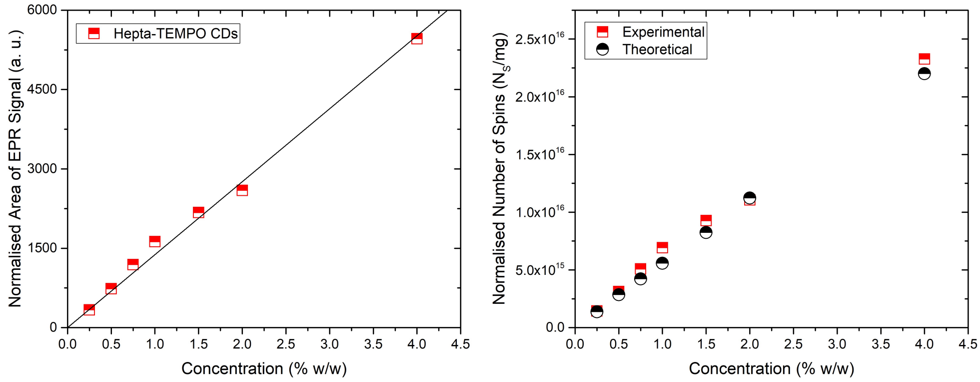

Figure 4.36: Area of the EPR signal of the Hepta-TEMPO sample normalised to the EPR samples mass (left) and experimental and theoretically simulated number of electron spins per milligram (right) as a function of radical concentration.

The electron gyromagnetic ratio was calculated from equation 2.80 with $g_e = 2.0068$, close to the free electron's one. The number of spins for each sample was calculated also theoretically by the equation 4.18 considering one effective spin per molecule, normalised to the total mass of each sample,

$$N_{S,theor.} = \frac{m\,[g]}{2782.12\,[g/mole]} \times N_A\,[mole^{-1}] \tag{4.18}$$

where m is the mass of the radical molecules that used in the synthesis of each different sample and $2782.12\,[g/mole]$ is the molecular weight of the Hepta-TEMPO doped molecules. In figure 4.36(left) we have a linear dependence of the area of the EPR signal as a function of the Hepta-TEMPO radical concentration, as expected. In figure 4.36(right) we have the theoretically calculated and experimental number of electron spins per milligram N_S/mg. We see that the experimental value coincides with the theoretical prediction justifying the value of an effective spin for the Hepta-TEMPO radical equal to $\frac{3}{2}$.

4.3.3 Acetylated β-CDs

The need for longer nuclear relaxation times drove the modification of our past experimental work on the methylated β-CDs[45] with the substitution of the deuterated methyl groups with carboxyl groups, labelled with ^{13} nuclei. The high temperature NMR study of ^{1}H for the acetylated samples with (CD586) and without (CD585) radicals is presented in figure 4.37.

From this figure we can distinguish a power law behaviour for both samples in the temperature range $20\,K \leq T \leq 60\,K$ which is a property of the glassy dynamics. In this temperature region it seems that the presence of radicals

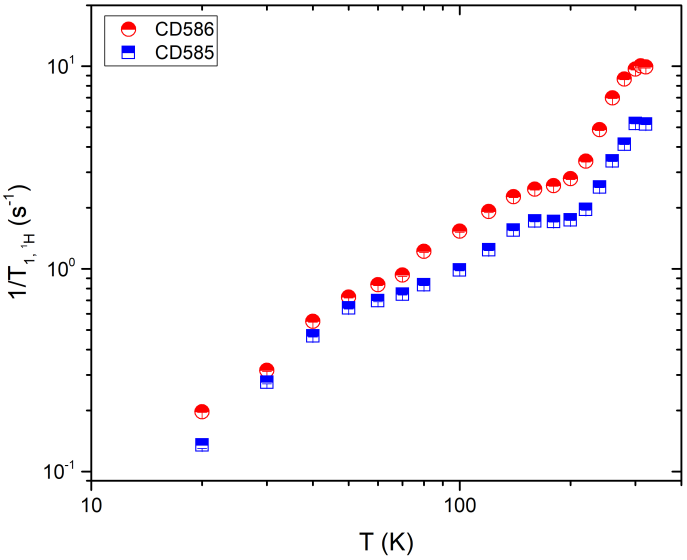

Figure 4.37: Logarithmic representation of the temperature dependence of the ^{1}H nuclear spin-lattice relaxation rate for the CD585 and CD586 samples in a 3.4 T magnetic field.

does not effect significantly the spin-lattice relaxation rate. Around 70 K the two curves start to split with the relaxation rates of the radical doped sample (CD586) to be higher than the ones of the undoped sample (CD585) while around 220 K we observe a sudden increase of the relaxation rates for both samples. This behaviour of the ^{1}H relaxation rate can be also seen in figure 4.38, where we have plotted the temperature dependence of the NMR linewidth.

This abrupt decrease of the NMR linewidth at 70 K is most probably associated with the activation energy of the carboxyl groups, according to the literature[158]. The change of slope at 220 K is attributed to the glass transition of the cyclodextrins as in the previously studied cases. As we can see in figure 4.39 that the shape of the NMR linewidth changes significantly with the temperature; at low temperatures it is clearly a gaussian curve while upon increasing the temperature it clearly transforms progressively into a lorentzian one, underlying the effect of motional narrowing to the NMR spectra (see also chapter 2). The data of the figure 4.38 where analysed accordingly.

In order to complete the high temperature study below 60 K for the CD585 and CD586 we present in figure 4.40 the temperature dependence of the relaxation rate for ^{1}H at the temperature range $20 \leq T \leq 60$ and for ^{13}C at the temperature range $10 \leq T \leq 30$. Both experimental datasets were fitted with a power law of the form $y(T) = \mathrm{a}T^b$. Above 30 K the signal of carbon was too weak, for the experimental set-up that was used, and thus indistinguishable

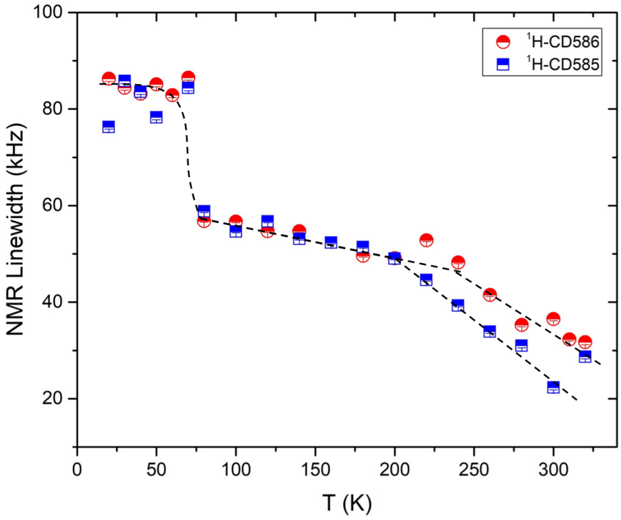

Figure 4.38: Temperature dependence of the NMR linewidth for both the acetylated samples, doped (CD586) and undoped (CD585), of ^{1}H nuclei in a 3.4 T magnetic field. Black dashed lines were added as guides to the eye.

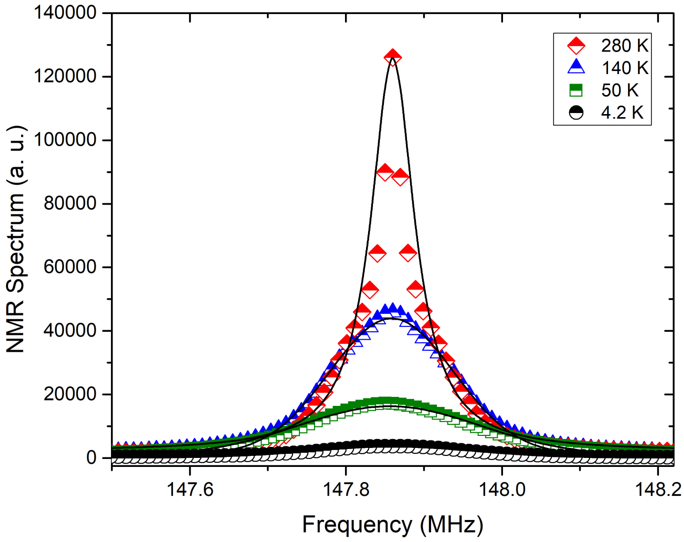

Figure 4.39: ^{1}H NMR spectrum of the radical doped acetylated sample CD586 as a function of the NMR frequency at four different temperatures in a 3.4 T magnetic field.

from the thermal noise.

Regarding the exponents b as obtained by the power law fit we have for the CD586 sample: $b_{^1H} = 1.37$ and $b_{^{13}C} = 1.5$. In comparison to what we found for the behaviour of the nuclear lattice relaxation rate in the temperature range $1.6\,K \leq T \leq 4.2\,K$ (figure 4.19) the b values are significantly lower, especially in the case of ^{1}H.

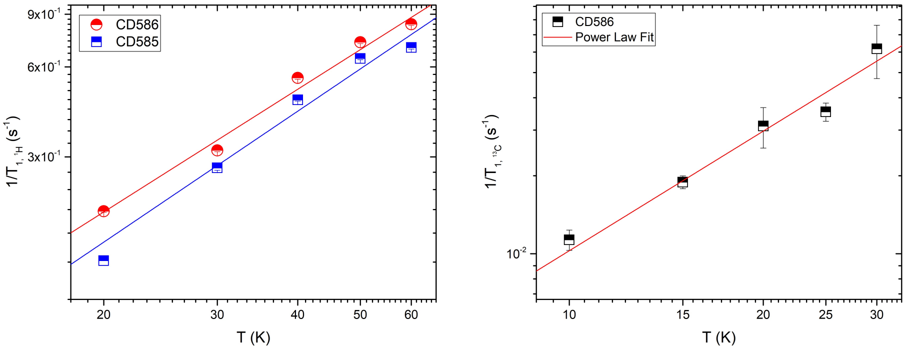

Figure 4.40: Temperature dependence of the nuclear relaxation rates for ^{1}H (left) and ^{13}C (right) nuclei of the radical doped (CD586) and undoped (CD585) acetylated samples at 3.4 T. The experimental data have been fit according to the power law $y(T) = \mathrm{a}T^b$, with parameters for ^{1}H: CD585, a $= (2 \pm 1) \times 10^{-3} K^{-b} s^{-1}$ and $b = 1.5 \pm 0.2$; CD586, a $= (3.3 \pm 0.9) \times 10^{-3} K^{-b} s^{-1}$ and $b = 1.37 \pm 0.08$; for ^{13}C: CD586, a $= (3 \pm 2) \times 10^{-4} K^{-b} s^{-1}$ and $b = 1.5 \pm 0.2$.

It is evident that, in this temperature range, the glassy dynamics is not the dominate relaxation process and other relaxation processes start to interfere in the nuclear relaxation. Nevertheless, in the case of ^{13}C, which is more suitable for molecular imaging applications, we achieved higher nuclear relaxation times (× 20) in comparison with our past work[45].

Conclusions

In this dissertation we succeded in the implementation of the Dynamic Nuclear Polarization in organic molecular compounds of biomedical and pharmaceutical interest, the β-Cyclodextrins. The study was focused in this kind of macromolecules mainly because of the important physicochemical properties that they possess but also because of the fact that, usually only small molecules are considered for DNP. Different variations of β-CDs were studied, in order to improve the overall DNP performance and contribute to the research of new, non-toxic and more efficient contrast agents for future in-vivo molecular imaging applications.

Continuing a past series of works[43, 44], we deuterated the completely methylated β-CDs labelled with ^{13}C (samples CD21d and CD21Rd) in order to increase the DNP performance and obtain longer relaxation times by reducing the spin-lattice relaxation driven by the dipolar coupling with ^{1}H nuclei. In fact, we succeed in a signal enhancement of the carbon nuclei up to 180 at 1.6 K that corresponds to a DNP enhanced nuclear polarization of 10% and relaxation time at room temperature equal to 33 s. Despite the fact that 33 s is not a sufficiently long time for the hyperpolarized samples to be transported at long distances, the high enhancement and the relatively long relaxation time makes this sample promising for biomedical applications although even longer relaxation times are needed. This led us to the substitution of the deuterated methyl groups with carboxyl groups labelled with ^{13}C (samples CD585 and CD586) containing oxygen nuclei with spin $I = 0$. Indeed we achieved much higher relaxation times by a factor of 20 at 1.6 K. These samples contain an average number of 7 carbon nuclei per molecule which leaded to a poor NMR signal at room temperature. Increasing the number of carboxyl groups could increase also the strength of the NMR signal. The DNP performance seems comparable to the aforementioned samples where for both a signal enhancement up to 50 at 2.5 K that corresponded to a nuclear polarization equal to 2.5%.

As regards the ^{1}H nuclei, in the case of the methylated samples we obtain a rather temperature independent signal enhancement in the range $20 \leq \epsilon \leq 30$ that corresponds to a nuclear polarization $2 \leq P(\%) \leq 6$. In the case of the acetylated samples we obtain a better DNP performance with a signal enhancement equal to 50 at 1.6 K, followed by a nuclear polarization equal to 11%. The large abundance of hydrogen nuclei in the human body and their fast relaxation at room temperature make them less useful for applications.

From the low temperature study of both samples for ^{1}H and ^{13}C nuclei we can safely say that the mechanism responsible for the polarization transfer is indeed the Thermal Mixing since the relaxation time $\frac{1}{T_1}$ as a function of $\frac{1}{T_{POL}}\left(1-P_e^2\right)$ shows a linear behaviour with a slope close to unity. Deviations from the theoretical trend are due to the existence of extra nuclear processes, other than the dominant interaction with the radical electrons including the dipole-dipole interaction with the same or different nuclear species, interaction with the lattice dynamics. From the temperature dependence of the relaxation rate at low temperature we obtained that glassy dynamics of the amorphous nature of the material dictates the nuclear relaxation. On the other hand, from the high temperature study, the behaviour of the relaxation rate as a function of temperature changes and a different glassy landscape starts to play a role progressively in the relaxation of the nuclei. At higher temperatures ($> 50\,K$) we noticed from the temperature dependence of the relaxation rate and of the NMR linewidth that carbon nuclei are more sensitive to the activation of molecular motions (rotation of the methyl and carboxyl groups) while hydrogen nuclei seem more sensitive to the glass transition of the material. This affects the echo decay very much like the motional narrowing where the signal shape is affected by the relative motion of the nuclei.

Regarding the Hepta- and Mono-TEMPO samples (series A_i and B_i) we compared the DNP performance of ^{1}H nuclei for different radical concentrations. The best results were obtained from the samples doped with 1% w/w of radicals. Despite our hopes, Mono-TEMPO samples performed 3 times better than this 'new' type of radical, with a DNP enhancement equal to 60 at 1.6 K and an enhanced nuclear polarization of 13%. The Hepta-TEMPO radical has almost 3 times higher effective magnetic moment ($\mu_{eff} = 4.2\mu_B$) and relaxes very fast; much faster than the time needed for an efficient spin diffusion. Nevertheless, for both series of samples we still see a good agreement with the Thermal Mixing theory. In all the samples of these sample series we observed two peaks in the temperature dependence of the relaxation rate followed by abrupt changes in the NMR linewidth. Those peaks were identified as the rotation of the methyl groups (around 120 K) and the glass transition (around 260 K) and the activation energies were recovered after the appropriate fitting with a variation of the BPP formula.

We also performed CW EPR measurements to analyse the local properties of Hepta-TEMPO radical. The EPR curves present three broad superimposed peaks due to the hyperfine interaction with a nucleus of spin $I = 1$ and we found that the effective spin of the 7 interacting electrons on the molecule rim is $S = \frac{3}{2}$.

The current work could be extended by studying different variants of the cyclodextrins like the complete acetylated molecule with carboxyl groups labelled with ^{13}C that is expected to provide more intense signal and presumably better DNP performance. The study of the DNP performance of the deuterium nuclei could be interesting in order to better understand the physics of the microscopic environment of the samples. The substitution of the β-CDs with α- or γ-CDs could also change the performance of the samples with their different sizes while it would be intrigued to study the polarization transfer to the guest-molecules when CDs form complex inclusions. Finally, as regards the experimental set-up, the use of swept and more intense microwave pulses could also increase even further the DNP performance. This could open the way for dissolution DNP experiments in order to study the performance of these materials in real conditions.

Appendix A

Experimental set-up

A.1 Nuclear Magnetic Resonance

An NMR basic equipment contains the spectrometer for the for the signal readout, a frequency generator for the excitation pulses, an amplifier to increase the signal that reaches the spectrometer, a decoupler which decouples the high power signal from the spectrometer to the pre-amplifier, the superconducting magnet and the NMR probe that holds the sample as we can see schematically in the following figure.

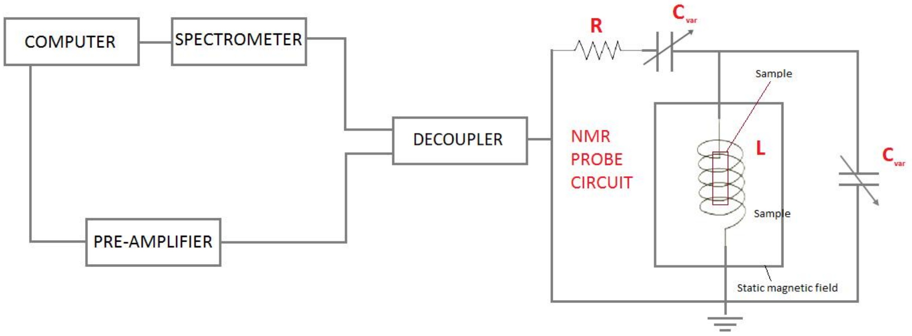

Figure A.1: Graphic representation of the NMR equipment basic block scheme. The NMR probe circuit contains a resistance R, a coil L and two external capacitors C_{var}. All those components complete an ordinary RLC circuit.

The coil which is used for the RF excitation pulses is used also for the reading of the signal. A voltage is induced in the coil thanks to the time dependent magnetic flux generated by the nuclear moments. This voltage is then analysed and becomes the signal of the spectrometer. The whole set up is remotely controlled by a computer. In order to excite properly the system and detect the response signal the NMR probe circuit has to be brought in resonance with the Larmor frequency of the nuclei that we intend to investigate. As it is known the resonance frequency of an RLC circuit is given by the formula

$$\omega_{probe} = \frac{1}{\sqrt{LC}} \tag{A.1}$$

where C is the total capacitance. So by controlling the variable capacitance one can change the resonance of the probe to be equal to the Larmor frequency.

A more detailed description of an NMR spectrometer is in the following picture where the electronic parts of the set-up, the pulse generation process and the signal detection process are presented.

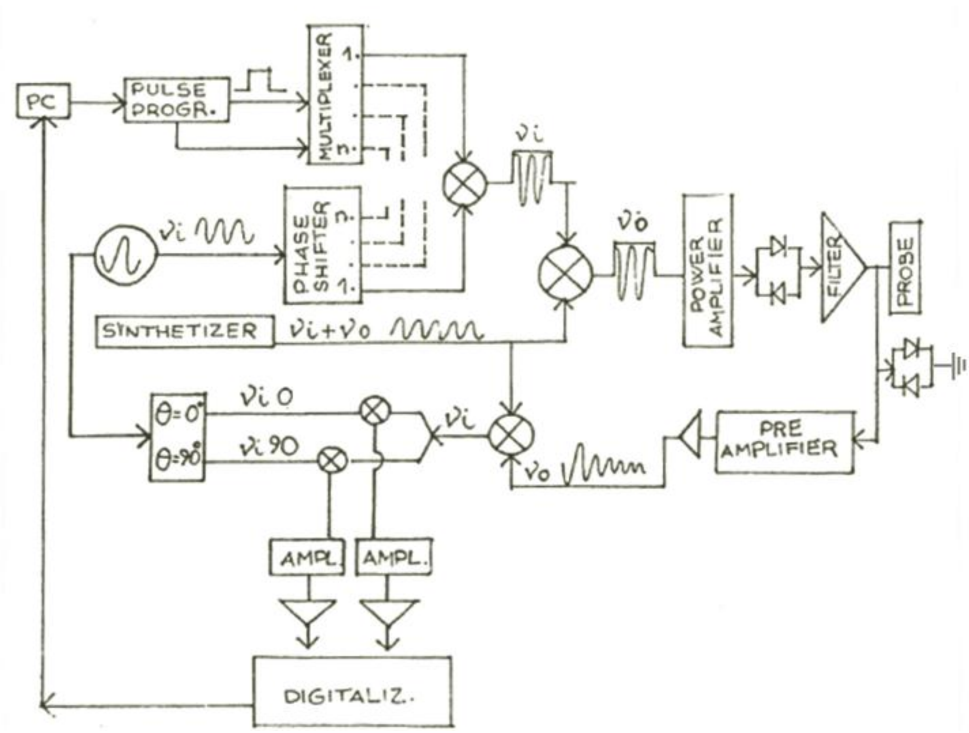

Figure A.2: Block diagram for an NMR spectrometer. This diagram contains the electronic parts, the pulse generation and the signal detection processes for an NMR experiment.

By controlling with the computer (PC) a pulse sequence TTL (transistor transistor logic) can be created. TTL is a common semiconductor technology for building discrete digital logic integrated circuits and the pulses that are produced are rectangular of 5 V. These pulses are characterized by two parameters: length and delay. A harmonic wave coming out from the phase shifter is then mixed with the TTL pulse producing a new pulse at an intermediate frequency (ν_i). Then the synthesizer generates another harmonic wave at a frequency of the sum of the intermediate frequency and the Larmor resonance frequency ($\nu_i + \nu_0$) in order to bring the initial pulse at the Larmor frequency. Now the pulse is ready to be amplified and cleaned passing by the decoupler and finally arrives to the probe and excites the sample. The nuclei in their turn produce a circularly polarized response signal that can be decomposed in two perpendicular fields dephased by 90°. So, the signal is mixed again with the pulse of the synthesizer in order to be brought to the intermediate frequency and then it is mixed with two pulses, dephased by 90°, at the intermediate frequency in order to collect the real and the imaginary part of the NMR signal as was described in chapter 2. This process is called quadrature detection. Finally the signal is amplified again and then digitalized with a typical dwell time in the 0.2-1 μs range in our experiments.

Since the NMR magnet is a superconductor one needs a particular architecture in order to bring it at low temperatures and reach the superconducting state. This architecture consists of three different chambers; a vacuum chamber and two others that host the cryogenic liquids. Usually liquid nitrogen and liquid helium are used which levels are monitored externally. Since the magnet is constantly in use the cryogenic liquids are refilled frequently. The maximum field that we can achieved with this apparatus at the Physics Department of the University of Pavia is 9.4 T although by changing the current of the superconducting coil and by choosing a different value one can set the magnetic field to lower values. When the magnetic field is changed there is a small voltage which is produced in the copper surrounding of the superconducting wires which can heat up and cause the quenching of the magnet. Thus, it is important to ramp the field slowly.

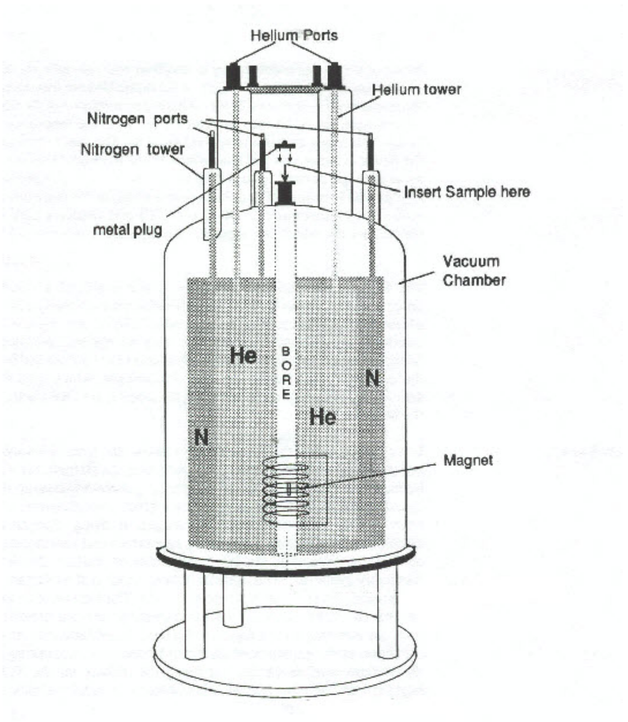

Figure A.3: Internal structure of an NMR superconducting magnet. Figure adapted from *Bruker BioSpin, AVANCE Beginners Guide.*

A.2 Cryogenic and vacuum system

For the low temperature experiments (1.6 K-4.2 K) a bath cryostat was used. It has almost the same architecture as the superconducting magnet since it also uses to reach low temperatures. Thus it contains the vacuum chamber as a temperature shielding and then two chambers that host the cryogenic liquids, as before. In the core of the cryostat there is a cavity that hosts the NMR probe where the sample holder is located. For the high temperature experiments (10 K-320 K) a straight arm flux cryostat was used with a continuous and regulated helium flux. In the bottom of the flux cryostat there is a heating resistance for the desired temperature stabilisation.

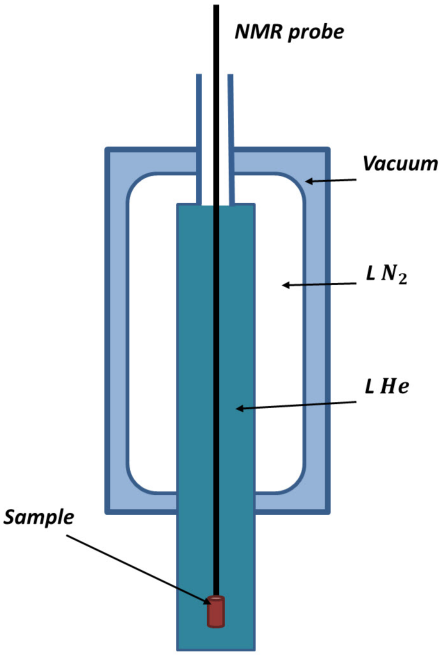

Figure A.4: Internal structure of a bath cryostat.

In order to isolate thermally the cryostats we need to produce vacuum to its outer chamber. For this we use a specific type of pump, the turbo molecular pump, since we need to achieve a vacuum, or better a pressure of 10^{-6} mbar.

In order to reach temperatures below 4.2 K with the bath cryostat a big positive-displacement rotary type pump was connected to the helium chamber. The vacuum produced by this pump was progressively increased, manually, by the valves that control the opening of the pump tubes in order to avoid a fast evaporation of helium. For a fine vacuum control a Saunders-Edwards speed valve was also used. It consists of a stator and two rotors that rotate in opposite orientations.

A.3 Dynamic Nuclear Polarization

In order to perform the DNP measurements we have to irradiate the system with microwaves. We used two different irradiation set-ups both attached to the same home-made DNP NMR probe; a manually tunable Gunn diode in the case of the methylated samples and an automatic external signal generator with high output power followed by an integrated amplifier/multiplier chain attached on the top of the probe. Waveguides pass, from the top, through the probe directly to the sample area allowing the direct irradiation of the sample. A diode in general is a semiconductor electrical component that allows the flow of current in only one direction having almost zero resistance while prevents the current flow in the opposite direction having high electrical resistance. A Gunn diode is a particular class of diodes that, as the others, exhibits non-linear current voltage behaviour and works on the principle of the Gunn effect. Now, the Gunn effect can be defined as generation of microwave power whenever the voltage applied to a semiconductor device exceeds the threshold voltage value[159]. It consists of three different layers all n type (doped GaAs) where the two are highly doped and the thinner one (8-10 μm) in the middle is less doped. The structure has been fabricated epitaxially. So, when a voltage higher than the voltage threshold is applied the electrons tend to move back and forth, that is they oscillate at a frequency of microwaves. This oscillation can be seen in the figure A.5. The current increases until the voltage threshold and then by increasing even more the voltage the current decreases and increases again. So by applying a low frequency electron pulse, thanks to this electron oscillation, the pulse will be amplified and microwave radiation will be emitted.

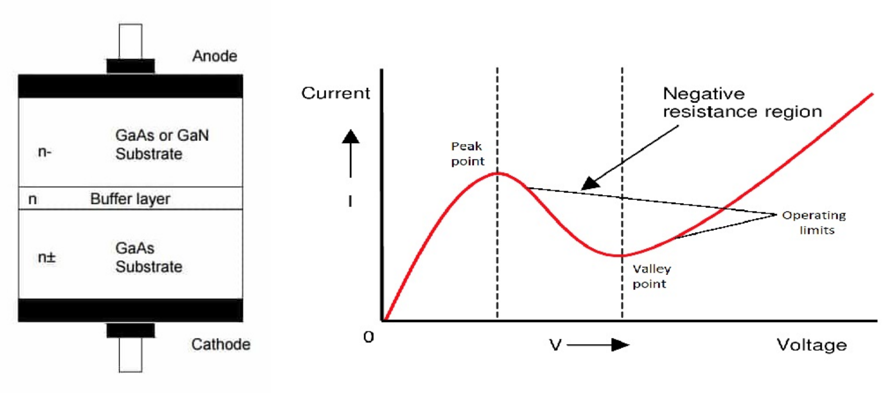

Figure A.5: On the right we have the structure of a Gunn diode with n doped GaAs fabricated epitaxially. On the left we see the voltage dependence of the current that passing through the diode. The Gunn diode works in the negative resistance region.

The second irradiation set-up components can be seen in figure A.6. On the right we have the microwave source that works in the frequency range

250 kHz-20 GHz with resolution equal to 0.001 Hz. It provides four different modes of operation : i) continuous wave (CW), ii) swept signal (SS), iii) analog modulation (AM) and iv) digital modulation (DM). For the experiments the CW mode at constant frequency (16.235 GHz) and constant output power (0 dBm) was used without any amplitude or frequency modulation. In order to generate MW in the W-band we used a frequency multiplier that contains non-linear circuits that distort the input signal, coming from the microwave source, generating high frequency harmonics. The frequency multiplication factor is (×6) while the output power is 15 dBm. Both devices were connected with a microwave guide of 25 mm radius and 50 Ohm resistance.

Figure A.6: Automatic external signal generator with high output power produced by Agilent (left) and integrated amplifier/multiplier chain produced by Virginia Diodes (right).

A.4 Electron Paramagnetic Resonance

A basic EPR set-up is schematically represented in figure A.7. It consists of an EPR cavity which is placed inside the magnet and hosts the sample. The irradiation at constant frequency is produced my the microwave source (Klystron) and reaches the sample through the microwave bridge. After the excitation of the electrons the response signal passes to the detector where it is recorded. The used spectrometer works in the band X (∼9.5 GHz) and was fabricated by Bruker.

The magnet is a hydro-cooled electromagnet that produces magnetic fields of variable intensity in the region 50 G-1 T. Inside the magnet there is a rectangular EPR cavity that is resonant in the transverse electric field mode TE_{102}, with the electric field to be equal to zero along the y axis. It is designed in such a way that creates standing electromagnetic waves inside (figure A.8,left). The electric and magnetic field components of these waves are completely out of phase. When the magnetic field is maximum the electric field is minimum and vice versa. In the center of the cavity, where the sample is placed, the electric field is maximum.

The produced microwaves enter the cavity through a small opening called Iris. Just before this opening there is a metallic plate called Iris screw (figure A.8,right) and this screw controls how much irradiation can go in and out of

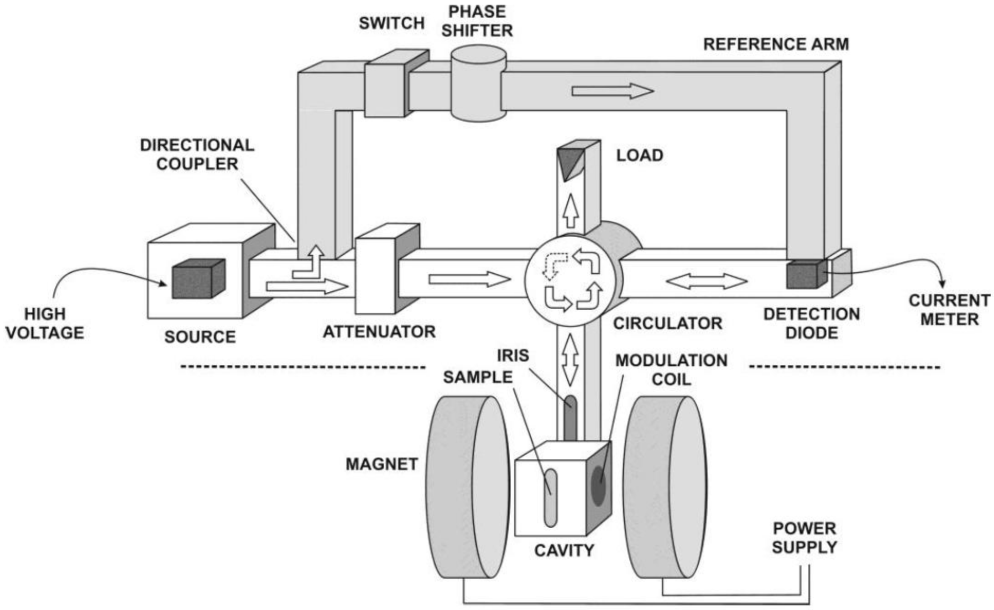

Figure A.7: Block diagram of a basic EPR equipment. Figure adapted from *Hagen, Biomolecular EPR Spectroscopy* [160].

the cavity. There is a single point of the screw where the cavity is critically coupled; all power enters in and no power is reflected out. At this point the cavity has the maximum figure of merit (Q factor) which can see in the equation A.2 where ν_0 is the irradiation frequency, E_{stored} is the energy that is stored in the cavity and P_{dis} is the dissipation power.

$$Q = 2\pi\nu_0 \frac{E_{stored}}{P_{dis}} \tag{A.2}$$

The Q factor depends of course on the size of the cavity but also in the material that it is made of. During an EPR experiment the sample absorbs the microwave irradiation, the Q factor is lowered with the cavity not being critically coupled any more. In the end the microwaves are reflected back to the microwave bridge.

The microwaves are produced by a device called Klystron (figure A.9)[161]. It consists of a hot cathode that produces electrons when heated. The produced electrons pass to the anode because of an applied high voltage difference between the anode and the cathode. Around the path of the electron there is an externally applied magnetic field that collimates the electron beam along the motion axis. Then the beam passes through a cavity resonator (buncher) with an AC potential; the first electrons entering the cavity are accelerated while the ones just before are decelerated. The second electrons that will be accelerated will catch the first decelerated electrons creating an electron bunch. These electron bunches will pass through a second cavity (catcher). In the catcher, the electric field opposes the motion of the electron bunches and

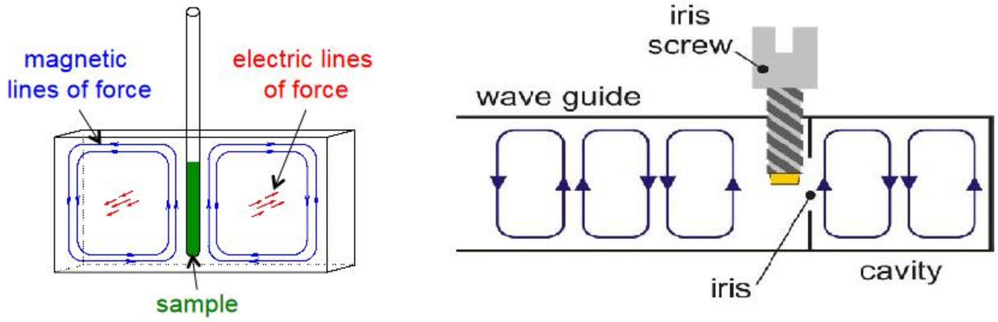

Figure A.8: Graphic representation of a rectangular EPR cavity (left) and the Iris aperture and screw (left).

as a result we have the emission of the microwaves by the decelerated electrons. The frequency of the microwaves depends on the voltage of the Klystron reflector. For the stabilisation of the irradiation frequency an automatic system of frequency control (AFC) was used that allows to fix the irradiation frequency produced by the klystron to the resonance frequency of the cavity.

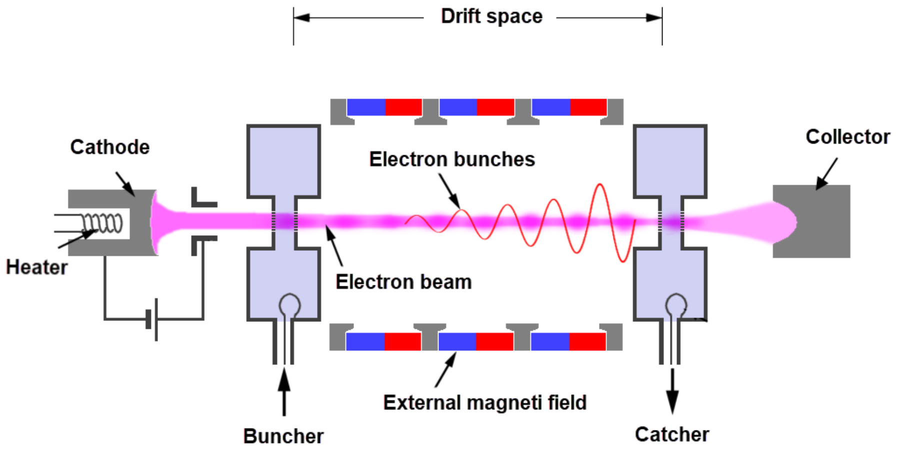

Figure A.9: Graphic representation of a two cavity Klystron microwave source. Figure created by *C. Whisky*.

After the microwave source the beam is split by a directional coupler in two components, one towards the cavity (microwave bridge) and the other one towards the reference arm, as we can see in figure A.7. On the microwave bridge the irradiation passes first by an attenuator, which is a device that allows the progressive passage of the irradiation and in the same time it strongly attenuates any reflection component, and arrives to the circulator. Then it is redirected to the cavity and the reflected by the cavity signal goes to the detector. Any unwanted reflection is attenuated in the Load. On the reference arm, there is a phase shifter that allows phase sensitive detection by stabilising a phase relation between the reference and reflected by the cavity signal.

Generally an EPR signal is very noisy. In order to increase the signal to noise ratio and obtain high quality spectra we use a technique called modulation field. This field is produced by two Helmholtz coils around the EPR cavity and it is sinusoidal. If there is an EPR signal the field modulation quickly sweeps through part of the signal and the reflected from the cavity microwaves are amplitude modulated in the same frequency. For an EPR signal, which is approximately linear over an interval as wide as the modulation amplitude, is transformed into a sine wave with an amplitude proportional to the slope of the signal. As a result, we measure the first derivative of the absorption signal (figure A.10).

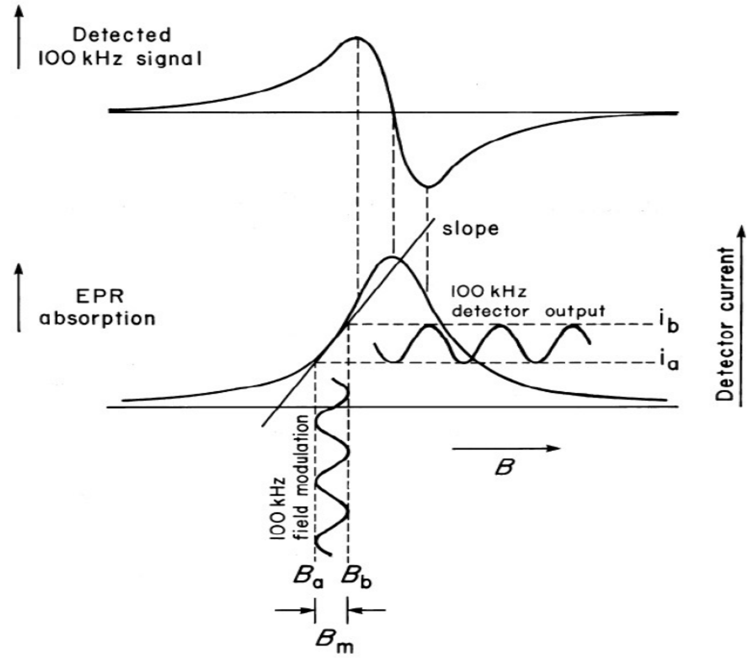

Figure A.10: Modulation effect on the output current of the detector. The magnetic field varies between the extremes B_a and B_b and the current varies sinusoidally between the values i_a and i_b.

There are two essential parameters of the modulation; the frequency and the amplitude. The frequency has to be smaller than the linewidth of the signal and usually it is set to 100 kHz range. On the other hand, if the amplitude is too low, we obtain a low signal intensity. If it is too high the signal becomes broader and distorted. As a general line, the modulation amplitude has to be smaller than 10% of the distance between the positive and the negative peak of the spectra. It is crucial to optimise all the parameters in order to obtain a good signal.

Appendix B

List of samples

Sample	**TEMPO(%)**	^{13}**C atoms**	**D atoms**	**Sample Category**
CD21d	0	yes	yes	Completely methylated
CD21Rd	1	yes	yes	Completely methylated
A_0	0	no	no	RAMEB
A_1	0.25	no	no	Hepta-TEMPO
A_2	0.5	no	no	Hepta-TEMPO
A_3	0.75	no	no	Hepta-TEMPO
A_4	1	no	no	Hepta-TEMPO
A_5	1.5	no	no	Hepta-TEMPO
A_6	2	no	no	Hepta-TEMPO
A_7	4	no	no	Hepta-TEMPO
B_1	0.25	no	no	Mono-TEMPO
B_2	0.5	no	no	Mono-TEMPO
B_3	0.75	no	no	Mono-TEMPO
B_4	1	no	no	Mono-TEMPO
B_5	1.5	no	no	Mono-TEMPO
B_6	2	no	no	Mono-TEMPO
B_7	4	no	no	Mono-TEMPO
CD585	0	yes	no	Acetylated
CD586	1	yes	no	Acetylated

Table B.1: Complete list of all studied samples.

Bibliography

[1] E. Lucaccini, L. Sorace, F. Adelnia *et al.* NMR and μ^+SR detection of unconventional spin dynamics in Er(trensal) and Dy(trensal) molecular magnets. *Phys. Rev. B* **100**, 174416 (2019).

[2] Y. Song, S. Utsuzawa and Y. Tang. Low fields but high impact: Ex-situ NMR and MRI. *J. Magn. Reson.* **306**, 109–111 (2019).

[3] A. Vignoli, V. Ghini, G. Meoni *et al.* High-Throughput Metabolomics by 1D NMR. *Angew. Chem. Int. Ed.* **58**, 968–994 (2019).

[4] C. P. Gordon, S. Shirase, K. Yamamoto *et al.* NMR chemical shift analysis decodes olefin oligo- and polymerization activity of d^0 group 4 metal complexes. *PNAS USA* **115**, E5867–E5876 (2018).

[5] R. Horst, K. A. Farley, B. L. Kormos *et al.* NMR spectroscopy: the swiss army knife of drug discovery. *J. Biomol. NMR* **74**, 509–519 (2020).

[6] E. Hatzakis. Nuclear Magnetic Resonance (NMR) Spectroscopy in Food Science: A Comprehensive Review. *Compr. Rev. Food Sci. Food Saf.* **18**, 189–220 (2019).

[7] M. Goldman. Dynamic nuclear polarization. *C. R. Phys.* **20**, 694–705 (2019).

[8] B. J. Albert, C. Gao, E. L. Sesti *et al.* Dynamic Nuclear Polarization Nuclear Magnetic Resonance in Human Cells Using Fluorescent Polarizing Agents. *Biochemistry* **57**, 4741–4746 (2018).

[9] G. Parigi, E. Ravera, M. Bennati *et al.* Understanding Overhauser Dynamic Nuclear Polarisation through NMR relaxometry. *Mol. Phys.* **117**, 888–897 (2019).

[10] K. O. Tan, R. T. Weber, T. V. Can *et al.* Adiabatic Solid Effect. *J. Phys. Chem. Lett.* **11**, 3416–3421 (2020).

[11] Y. Li, A. Equbal, T. Tabassum *et al.* ^1H Thermal Mixing Dynamic Nuclear Polarization with BDPA as Polarizing Agents. *J. Phys. Chem. Lett.* **11**, 9195–9202 (2020).

[12] W. Liao, B. Ghaffari, C. P. Gordon *et al.* Dynamic Nuclear Polarization Surface Enhanced NMR spectroscopy (DNP SENS): Principles, protocols, and practice. *Curr. Opin. Colloid. Interface Sci.* **33**, 63–71 (2018).

[13] L. Malwina, S. Andrzej and K. Michal. Characteristic of Cyclodextrins: Their Role and Use in the Pharmaceutical Technology. *Curr. Drug Targets* **21**, 14 (2020).

[14] L. Melone, A. Bach, G. Lamura *et al.* Cyclodextrin-Based Organic Radical Contrast Agents for in vivo Imaging of Gliomas. *ChemPlusChem* **85**, 1171–1178 (2020).

[15] J. G. Skinner, L. Menichetti, A. Flori *et al.* Metabolic and Molecular Imaging with Hyperpolarised Tracers. *Mol. Imaging Biol.* **20**, 902–918 (2018).

[16] E. B. Adamson, K. D. Ludwig, D. G. Mummy *et al.* Magnetic resonance imaging with hyperpolarized agents: methods and applications. *Phys. Med. Biol.* **62**, 81–123 (2017).

[17] M. Filibian, S. Colombo Serra, M. Moscardini *et al.* The role of the glassy dynamics and thermal mixing in the dynamic nuclear polarization and relaxation mechanisms of pyruvic acid. *Phys. Chem. Chem. Phys.* **16**, 27025–27036 (2014).

[18] A. S. L. Thankamony, J. J. Wittmann, M. Kaushik *et al.* Dynamic nuclear polarization for sensitivity enhancement in modern solid-state NMR. *Prog. Nucl. Magn. Reson. Spectrosc.* **102-103**, 120–195 (2017).

[19] V. Z. Miloushev, K. R. Keshari & Holodny, A. I. Hyperpolarization MRI: Preclinical Models and Potential Applications in Neuroradiology. *Top. Magn. Reson. Imaging* **25**, 31–37 (2016).

[20] J. T. Grist, M. A. McLean, F. Riemer *et al.* Quantifying normal human brain metabolism using hyperpolarized [1-^{13}C]pyruvate and magnetic resonance imaging. *Neuroimage* **189**, 171–179 (2019).

[21] A. L. Kern and J. Vogel-Claussen. Hyperpolarized gas MRI in pulmonology. *Br. J. Radiol.* **91**, 20170647 (2018).

[22] G. Crini. Review: A History of Cyclodextrins. *Chem. Rev.* **114**, 10940–10975 (2014).

[23] T. Loftsson and M. E. Brewster. Pharmaceutical applications of cyclodextrins: basic science and product development. *J. Pharm. Pharmacol.* **62**, 1607–1621 (2010).

[24] E. Fenyvesi, M. Vikmon & Szente, L. Cyclodextrins in Food Technology and Human Nutrition: Benefits and Limitations. *Crit. Rev. Food Sci. Nutr.* **56**, 1981–2004 (2016).

[25] A. Villiers. Sur la fermentation de la fècule par l'action du ferment butyrique. *Comp. Rend. Acad. Sci.* **112**, 536–538 (1891).

[26] F. Schardinger. Bildung kristallisierter polysaccharide (dextrine) aus stärkekleister durch microben. *Zentralbl. Bakteriol. Parasitenk. Abt. II* **29**, 188–197 (1911).

[27] E. M. Martin Del Valle. Cyclodextrins and their uses: a review. *Process Biochem.* **39**, 1033–1046 (2004).

[28] J. Szejtli. Introduction and General Overview of Cyclodextrin Chemistry. *Chem. Rev.* **98**, 1743–175 (1998).

[29] S. K. Das, R. Rajabalaya, S. David *et al.* Cyclodextrins-The Molecular Container . *Res. J. Pharm., Biol. Chem. Sci.* **4**, 1694 (2014).

[30] C. J. Bruns. Exploring and Exploiting the Symmetry-Breaking Effect of Cyclodextrins in Mechanomolecules. *Symmetry* **11**, 1249 (2019).

[31] P. Jansook, N. Ogawa & Loftsson, T. Cyclodextrins: structure, physicochemical properties and pharmaceutical application. *Int. J. Pharm.* **535**, 272–284 (2018).

[32] M. N. Roy, D. Ekka, S. Saha *et al.* Host–guest inclusion complexes of α and β-cyclodextrins with α-amino acids. *RSC Adv.* **4**, 42383–42390 (2014).

[33] M. Kfoury, D. Landy and S. Fourmentin. Characterization of Cyclodextrin/Volatile Inclusion Complexes: A Review. *Molecules* **23**, 1204 (2018).

[34] V. B. Chaudhary. CYCLODEXTRIN INCLUSION COMPLEX TO ENHANCE SOLUBILITY OF POORLY WATER SOLUBLE DRUGS: A REVIEW. *Int. J. Pharm. Sci. Res.* **4**, 68–76 (2013).

[35] A. Haimhoffer, A. Rusznyák, K. Réti-Nagy *et al.* Cyclodextrins in Drug Delivery Systems and Their Effects on Biological Barriers. *Sci. Pharm.* **87**, 33 (2019).

[36] V. J. Stella, V. M. Rao, E. A. Zannou *et al.* Mechanisms of drug release from cyclodextrin complexes. *Adv. Drug Deliv. Rev.* **36**, 3–16 (1999).

[37] F. Schibilla, L. Stegemann, C. A. Strassert *et al.* Fluorescence quenching in β-cyclodextrin vesicles: membrane confinement and host–guest interactions. *Photochem. Photobiol. Sci.* **15**, 235–243 (2016).

[38] X. Mei, S. Yang, D. Chen *et al.* Light-triggered reversible assemblies of azobenzene-containing amphiphilic copolymer with β-cyclodextrin-modified hollow mesoporous silica nanoparticles for controlled drug release. *Chem. Commun.* **48**, 10010–10012 (2012).

[39] O. Bekers E. V. Uijtendaal, J. H. Beijnen *et al.* Cyclodextrins in the Pharmaceutical Field. *Drug Dev. Ind. Pharm.* **17**, 1503–1549 (1991).

[40] S. V. Kurkov and T. Loftsson. Cyclodextrins. *Int. J. Pharm.* **453**, 167–180 (2013).

[41] Y. Liu, Y. Chen, X. Gao *et al.* Application of cyclodextrin in food industry. *Crit. Rev. Food. Sci. Nutr.* **0**, 1–15 (2020).

[42] J. Szejtli. Cyclodextrins in Food, Cosmetics and Toiletries. *Stärke* **34**, 379–385 (1982).

[43] F. Caracciolo, P. Carretta, M. Filibian *et al.* Dynamic Nuclear Polarization of β-Cyclodextrin Macromolecules. *J. Phys. Chem. B* **121**, 2584–2593 (2017).

[44] F. Caracciolo, A. L. Paioni, M. Filibian *et al.* Proton and Carbon-13 Dynamic Nuclear Polarization of Methylated β-Cyclodextrins. *J. Phys. Chem. B* **122**, 1836–1845 (2018).

[45] F. Caracciolo, E. Charlaftis, L. Melone *et al.* Molecular dynamics and hyperpolarization performance of deuterated β-cyclodextrins. *J. Phys. Chem. B* **123**, 3731–3737 (2019).

[46] F. Caglieris, L. Melone, F. Canepa *et al.* Effective magnetic moment in cyclodextrin–polynitroxides: potential supramolecular vectors for magnetic resonance imaging. *RSC Adv.* **5**, 76133–76140 (2015).

[47] O. L. Lebedev and S. N. Kazarnovskii. Catalytic oxidation of aliphatic amines with hydrogen peroxide. *Zhur. Obshch. Khim.* **30**, 1631–1635 (1960).

[48] T. Wenckebach. *Essentials of Dynamic Nuclear Polarization* (Spindrift, 2016).

[49] D. Guarin, S. Marhabaie, A. Rosso *et al.* Characterizing Thermal Mixing Dynamic Nuclear Polarization via Cross-Talk between Spin Reservoirs. *J. Phys. Chem. Lett.* **8**, 5531–5536 (2017).

[50] K. N. Hu, V. S. Bajaj, M. Rosay *et al.* High-frequency dynamic nuclear polarization using mixtures of TEMPO and trityl radicals. *J. Chem. Phys.* **126**, 044512 (2007).

[51] A. Ajoy, R. Nazaryan, K. Liu & all. Enhanced dynamic nuclear polarization via swept microwave frequency combs. *Proc. Natl. Acad. Sci. U.S.A.* **115**, 10576–10581 (2018).

[52] J. Szejtli. *Cyclodextrins in Pharmaceuticals* (Springer, Dordrecht, 1988).

[53] B. Vuichoud, J. Milani, A. Bornet *et al.* Hyperpolarization of deuterated metabolites via remote cross-polarization and dissolution dynamic nuclear polarization. *J. Phys. Chem. B* **118**, 1411–1415 (2014).

[54] K. Kumagai, M. Akakabe, M. Tsuda *et al.* Observation of glycolytic metabolites in tumor cell lysate by using hyperpolarization of deuterated glucose. *Biol. Pharm. Bull.* **37**, 1416–1421 (2014).

[55] K. M. Brindle. Imaging Metabolism with Hyperpolarized ^{13}C-Labeled Cell Substrates. *J. Am. Chem. Soc.* **137**, 6418–6427 (2015).

[56] L. Melone, M. Petroselli, N. Pastori *et al.* Functionalization of Cyclodextrins with N-Hydroxyphthalimide Moiety: A New Class of Supramolecular Pro-Oxidant Organocatalysts. *Molecules* **20**, 15881–15892 (2015).

[57] P. Hermann, J. Kotek, V. Kubicek *et al.* Gadolinium(iii) complexes as MRI contrast agents: ligand design and properties of the complexes. *Dalton Trans.* 3027–3047 (2008).

[58] A. Fatima, Md. W. Ahmad, A. K. Al Saidi *et al.* Recent Advances in Gadolinium Based Contrast Agents for Bioimaging Applications. *Nanomaterials* **11** (2021).

[59] J. Ramalho, R. C. Semelka, M. Ramalho *et al.* Gadolinium-Based Contrast Agent Accumulation and Toxicity: An Update. *AJNR Am. J. Neuroradiol.* **37**, 1192–1198 (2016).

[60] K. N. Hu, H. Yu, T. M. Swager *et al.* Dynamic Nuclear Polarization with Biradicals. *J. Am. Chem. Soc.* **126**, 10844–10845 (2004).

[61] M. Porel, M. F. Ottaviani, S. Jockusch *et al.* Control of spin–spin exchange interactions in polynitroxides through inclusion within γ-cyclodextrin. *RSC Adv.* **3**, 427–431 (2013).

[62] S. Guo, X. Wang, Z. Li *et al.* A nitroxides-based macromolecular MRI contrast agent with an extraordinary longitudinal relaxivity for tumor imaging via clinical T1WI SE sequence. *J. Nanobiotechnol.* **19**, 244 (2021).

[63] F. Bellia, D. La Mendola, C. Pedone *et al.* Selectively functionalized cyclodextrins and their metal complexes. *Chem. Soc. Rev.* **38**, 2756–2781 (2009).

[64] P. R. Ashton, R. Königer, J. F. Stoddart *et al.* Amino acid derivatives of β-cyclodextrin. *J. Org. Chem.* **61**, 903–908 (1996).

[65] A. Gadelle and J. Defaye. Selective Halogenation at Primary Positions of Cyclomaltooligosaccharides and a Synthesis of Per-3,6-anhydro Cyclomaltooligosaccharides. *Angew. Chem., Int. Ed. Engl.* **30**, 78–80 (1991).

[66] C. P. Slichter. *Principles of Magnetic Resonance* (Springer, Berlin, Heidelberg, 1990).

[67] I. I. Rabi, J. R. Zacharias, S. Millman *et al.* A New Method of Measuring Nuclear Magnetic Moment. *Phys. Rev.* **53**, 318–318 (1938).

[68] C. Berthier M. Horvatić, M. H. Julien *et al.* Nuclear magnetic resonance in high magnetic field: Application to condensed matter physics. *C. R. Phys.* **18**, 331–348 (2017).

[69] C. Chachaty. Applications of NMR methods to the physical chemistry of micellar solutions. *Prog. Nucl. Magn. Reson. Spectrosc.* **19**, 183–222 (1987).

[70] M. Elyashberg. Identification and structure elucidation by NMR spectroscopy. *Trends Anal. Chem.* **69**, 88–97 (2015).

[71] H. E. Gottlieb, V. Kotlyar & Nudelman, A. NMR Chemical Shifts of Common Laboratory Solvents as Trace Impurities. *J. Org. Chem.* **62**, 7512–7515 (1997).

[72] D. Marion. An Introduction to Biological NMR Spectroscopy. *Mol. Cell. Proteom.* **12**, 3006–3025 (2013).

[73] Wüthrich, K. The way to NMR structures of proteins. *Nat. Struct. Mol. Biol.* **8**, 923–925 (2001).

[74] W. P. Aue, E. Bartholdi & Ernst, R. R. Two-dimensional spectroscopy. Application to nuclear magnetic resonance. *J. Chem. Phys.* **64**, 2229–2246 (1976).

[75] M. Haris, S. K. Yadav, A. Rizwan *et al.* Molecular magnetic resonance imaging in cancer. *J. Transl. Med.* **13**, 313 (2015).

[76] J. R. Singer. Blood Flow Rates by Nuclear Magnetic Resonance Measurements. *Science* **130**, 1652–1653 (1959).

[77] Hwang, J. H. & Choi, C. Use of in vivo magnetic resonance spectroscopy for studying metabolic diseases. *Exp. Mol. Med.* **47**, 139 (2015).

[78] N. Proietti, D. Capitani & Tullio, V. D. Nuclear Magnetic Resonance, a Powerful Tool in Cultural Heritage. *Magnetochemistry* **4** (2018).

[79] S. Esslinger, C. Fauhl-Hassek & Wittkowski, R. *Authentication of Wine by ^{1}H-NMR Spectroscopy: Opportunities and Challenges*, chap. 6, 85–108 (ACS Symp. Ser. Am. Chem. Soc, Vol. 1203, 2015).

[80] H. Ebrahimnejad, H. Ebrahimnejad, A. Salajegheh *et al.* Use of Magnetic Resonance Imaging in Food Quality Control: A Review. *J. Biomed. Phys. Eng.* **8**, 127–132 (2018).

[81] J. A. Weil and J. R. Bolton. *Electron Paramagnetic Resonance: Elementary Theory and Practical Applications* (Wiley, 2006).

[82] T. Biskup. Structure-Function Relationship of Organic Semiconductors: Detailed Insights From Time-Resolved EPR Spectroscopy. *Front. Chem.* **7**, 10 (2019).

[83] M. M. Roessler and E. Salvadori. Principles and applications of epr spectroscopy in the chemical sciences. *Chem. Soc. Rev.* **47**, 2534–2553 (2018).

[84] U. Eichhoff and P. Höfer. Medical applications of EPR. *Low Temp. Phys.* **41**, 62–66 (2015).

[85] M. Ubbink, A. Perrakis & Jeschke, G. The contribution of modern EPR to structural biology. *Emerg. Top. Life Sci.* **2**, 9–18 (2018).

[86] S. Wilczyński, B. Pilawa, R. Koprowski *et al.* Free radicals properties of gamma-irradiated penicillin-derived antibiotics: piperacillin, ampicillin, and crystalline penicillin. *Radiat. Environ. Biophys.* **53**, 203–10 (2014).

[87] P. M. Plonka. Electron paramagnetic resonance as a unique tool for skin and hair research. *Exp. Dermatol.* **18**, 472–84 (2009).

[88] Y. Kodama, O. Rodrigues Jr, R. H. L. Garcia *et al.* Study of free radicals in gamma irradiated cellulose of cultural heritage materials using Electron Paramagnetic Resonance. *Radiat. Phys. and Chem.* **124**, 169–173 (2016).

[89] R. T. Weber. Moder EPR Applications From Beer to Deer. *Brucker BioSpin Corp. EPR Division* (2011).

[90] N. Bloembergen, E. M. Purcell & Pound, R. V. Relaxation Effects in Nuclear Magnetic Resonance Absorption. *Phys. Rev.* **73**, 679–712 (1948).

[91] A. Abragam and M. Goldman. Principles of dynamic nuclear polarisation. *Rep. on Prog. in Phys.* **41**, 395–467 (1978).

[92] J. L. Bjorkstam, J. Listerud, M. Villa *et al.* Motional narrowing of a gaussian NMR line. *J. Magn. Reson.* **65**, 383–394 (1985).

[93] M. D. Hürlimann. Carr–Purcell Sequences with Composite Pulses. *J. Magn. Reson.* **152**, 109–123 (2001).

[94] H. Y. Carr and E. M. Purcell. Effects of Diffusion on Free Precession in Nuclear Magnetic Resonance Experiments. *Phys. Rev.* **94**, 630–638 (1954).

[95] C. Karunakaran and M. Balamurugan. Chapter Four - Electron Paramagnetic Resonance Spectroscopy. In Karunakaran, C. (ed.) *Spin Resonance Spectroscopy*, 169–228 (Elsevier, 2018).

[96] H. M. Swartz. Electron spin resonance: A comprehensive treatise on experimental techniques by C. P. Poole, Jr. *Med. Phys.* **11**, 568–569 (1984).

[97] L. V. Rychkova, V. P. Lutoev, B. A. Makeev *et al.* Magnetic susceptibility and NEXAFS, EPR spectra of co-doped Bi_3NbO_7. *J. Mater. Res. Technol.* **9**, 8013–8019 (2020).

[98] R. W. Hooper, B. A. Klein & Michaelis, V. K. Dynamic Nuclear Polarization (DNP) 101: A New Era for Materials. *Chem. Mater.* **32**, 4425–4430 (2020).

[99] M. L. Hirsch, N. Kalechofsky, A. Belzer *et al.* Brute-Force Hyperpolarization for NMR and MRI. *J. Am. Chem. Soc.* **137**, 8428–8434 (2015).

[100] K. Munnemann and H. Spiess. The art of signal enhancement. *Nat. Phys.* **7**, 522–523 (2011).

[101] T. G. Walker and W. Happer. Spin-exchange optical pumping of noble-gas nuclei. *Rev. Mod. Phys.* **69**, 629–642 (1997).

[102] M. Kirby, S. Svenningsen, N. Kanhere *et al.* Pulmonary ventilation visualized using hyperpolarized helium-3 and xenon-129 magnetic resonance imaging: differences in COPD and relationship to emphysema. *J. Appl. Physiol.* **114**, 707–715 (2013).

[103] C. Witte, M. Kunth, J. Döpfert *et al.* Hyperpolarized Xenon for NMR and MRI Applications. *J. Vis. Exp.* **67**, 4268 (2012).

[104] J. E. Roos, H. P. McAdams, S. Sivaram *et al.* Hyperpolarized Gas MR Imaging: Technique and Applications. *Magn. Reson. Imaging Clin. N. Am.* **23**, 217–229 (2015).

[105] B. M. Goodson. Nuclear magnetic resonance of laser-polarized noble gases in molecules, materials, and organisms. *J. Magn. Reson.* **155**, 157–216 (2002).

[106] T. C. Eisenschmid, R. U. Kirss, P. P. Deutsch *et al.* Para hydrogen induced polarization in hydrogenation reactions. *J. Am. Chem. Soc.* **109**, 8089–8091 (1987).

[107] P. Bhattacharya, E. Y. Chekmenev, W. F. Reynolds *et al.* Parahydrogen-induced polarization (PHIP) hyperpolarized MR receptor imaging in vivo: a pilot study of 13C imaging of atheroma in mice. *NMR Biomed.* **24**, 1023–1028 (2011).

[108] J. Eills, J. W. Blanchard, T. Wu *et al.* Polarization transfer via field sweeping in parahydrogen-enhanced nuclear magnetic resonance. *The Journal of Chemical Physics* **150**, 174202 (2019).

[109] A. Pravdivtsev, G. Buntkowsky, S. Duckett *et al.* Parahydrogen-induced polarization of amino acids. *Angew. Chem. Int. Ed.* **60** (2021).

[110] C. R. Bowers and D. P. Weitekamp. Parahydrogen and synthesis allow dramatically enhanced nuclear alignment. *J. Am. Chem. Soc.* **109**, 5541–5542 (1987).

[111] G. P. Michael and D. P. Weitekamp. Net NMR alignment by adiabatic transport of parahydrogen addition products to high magnetic field. *Chem. Phys. Lett.* **145**, 255–258 (1988).

[112] J.King, K. Jeong, C. Vassiliou *et al.* Room-temperature in situ nuclear spin hyperpolarization from optically pumped nitrogen vacancy centres in diamond. *Nat. Commun.* **6**, 8965 (2015).

[113] P. Dutta, G. V. Martinez & Gillies, R. J. Nanodiamond as a New Hyperpolarizing Agent and Its ^{13}C MRS. *J. Phys. Chem. Lett.* **5**, 597–600 (2014).

[114] D. Abrams, M. E. Trusheim, D. R. Englund *et al.* Dynamic Nuclear Spin Polarization of Liquids and Gases in Contact with Nanostructured Diamond. *Nano Lett.* **14**, 2471–2478 (2014).

[115] I. Schwartz, J. Scheuer, B. Tratzmiller *et al.* Robust optical polarization of nuclear spin baths using Hamiltonian engineering of nitrogen-vacancy center quantum dynamics. *Sci. Adv.* **4**, 8978 (2018).

[116] A. W. Overhauser. Polarization of Nuclei in Metals. *Phys. Rev.* **92**, 411–415 (1953).

[117] A. Abragam and W. G. Proctor. Spin Temperature. *Phys. Rev.* **109**, 1441–1458 (1958).

[118] C. E. Soliverez. The contact hyperfine interaction: an ill-defined problem. *J. Phys. C: Solid State Phys.* **13**, 1017 (1980).

[119] T. R. Carver and C. P. Slichter. Polarization of Nuclear Spins in Metals. *Phys. Rev.* **92**, 212–213 (1953).

[120] T. R. Carver and C. P. Slichter. Experimental Verification of the Overhauser Nuclear Polarization Effect. *Phys. Rev.* **102**, 975–980 (1956).

[121] W. Wenckebach. The Solid Effect. *Appl. Magn. Reson.* **34**, 227 (2008).

[122] B. Corzilius. Theory of solid effect and cross effect dynamic nuclear polarization with half-integer high-spin metal polarizing agents in rotating solids. *Phys. Chem. Chem. Phys.* **18**, 27190–27204 (2016).

[123] W. T. Wenckebach. Dynamic nuclear polarization via thermal mixing: Beyond the high temperature approximation. *J. Magn. Reson.* **277**, 68–78 (2017).

[124] S. C. Serra, A. Rosso & Tedoldi, F. Electron and nuclear spin dynamics in the thermal mixing model of dynamic nuclear polarization. *Phys. Chem. Chem. Phys.* **14**, 13299–13308 (2012).

[125] A. Lascialfari, M. Filibian, C. Sangregorio *et al.* In vivo biomedical applications of magnetic resonance and magnetic materials. *Riv. Nuovo Cimento Soc. Ital. Fis.* **36**, 211–271 (2013).

[126] J. Wolber, F. Ellner, B. Fridlund *et al.* Generating highly polarized nuclear spins in solution using dynamic nuclear polarization. *Nucl. Instrum. Methods. Phys. Res. B* **526**, 173–181 (2004).

[127] K. R. Thurber and R. Tycko. Theory for cross effect dynamic nuclear polarization under magic-angle spinning in solid state nuclear magnetic resonance: The importance of level crossings. *J. Chem. Phys.* **137**, 084508 (2012).

[128] G. R. Khutsishvili. SPIN DIFFUSION. *Sov. Phys. Usp.* **8**, 743–769 (1966).

[129] P. Mieville, P. Ahuja, R. Sarkar *et al.* Scavenging Free Radicals To Preserve Enhancement and Extend Relaxation Times in NMR using Dynamic Nuclear Polarization. *Angew. Chem. Int. Ed.* **49**, 6182–6185 (2010).

[130] T. Harris, C. Bretschneider and L. Frydman. Dissolution DNP NMR with solvent mixtures: substrate concentration and radical extraction. *J. Magn. Reson.* **211**, 96–100 (2011).

[131] B. Vuichoud, A. Bornet, F. de Nanteuil *et al.* Filterable Agents for Hyperpolarization of Water, Metabolites, and Proteins. *Chem. Eur. J.* **22**, 14696–14700 (2016).

[132] M. Filibian, E. Elisei, S. Colombo *et al.* Nuclear magnetic resonance studies of DNP-ready trehalose obtained by solid state mechanochemical amorphization. *Phys. Chem. Chem. Phys.* **18**, 16912–16920 (2016).

[133] A. Bornet, S. Jannin, R. Melzi *et al.* Cross Polarization for Dissolution Dynamic Nuclear Polarization Experiments at Readily Accessible Temperatures $1.2 < T < 4.2K$. *Appl. Magn. Reson.* **43**, 107–117 (2012).

[134] M. Batel, A. Hunkeler, A. Däpp *et al.* Cross-polarization for dissolution dynamic nuclear polarization. *Phys. Chem. Chem. Phys.* **16**, 21407–21416 (2014).

[135] A. Bornet and S. Jannin. Optimizing dissolution dynamic nuclear polarization. *J. Magn. Reson.* **264**, 13–21 (2016).

[136] X. Ji, A. Bornet, B. Vuichoud *et al.* Transportable hyperpolarized metabolites. *Nat. Commun.* **8**, 13975 (2017).

[137] F. Kurdzesau, B. van den Brandt, A. Comment *et al.* Dynamic nuclear polarization of small labelled molecules in frozen water-alcohol solutions. *J. Phys. D: Appl. Phys.* **41**, 155506 (2008).

[138] H. Johannesson, S. Macholl and J. H. Ardenkjaer-Larsen. Dynamic Nuclear Polarization of [1-^{13}C]pyruvic acid at 4.6 tesla. *J. Magn. Reson.* **197**, 167–175 (2009).

[139] S. Macholl, H. Johannesson and J. H. Ardenkjaer-Larsen. Trityl biradicals and ^{13}C dynamic nuclear polarization. *Phys. Chem. Chem. Phys.* **12**, 5804–5817 (2010).

[140] W. Meyer, J. Heckmann, C. Hess *et al.* Dynamic polarization of ^{13}C nuclei in solid ^{13}C labeled pyruvic acid. *Nucl. Instrum. Methods Phys. Res. A: Accel. Spectrom. Detect. Assoc. Equip.* **631**, 1–5 (2011).

[141] S. Reynolds and H. Patel. Monitoring the Solid-State Polarization of ^{13}C, ^{15}N, ^{2}H, ^{29}Si and ^{31}P. *Appl. Magn. Reson.* **34**, 495–508 (2008).

[142] L. Lumata, A. K. Jindal, M. E. Merritt *et al.* DNP by thermal mixing under optimized conditions yields >60,000-fold enhancement of ^{89}Y NMR signal. *J. Am. Chem. Soc.* **133**, 8673–8680 (2011).

[143] A. J. Leggett. Nuclear Magnetism: Order and Disorder. *Phys. Bull.* **34**, 29 (1983).

[144] S. C. Serra, A. Rosso and F. Tedoldi. On the role of electron-nucleus contact and microwave saturation in thermal mixing DNP. *Phys. Chem. Chem. Phys.* **15**, 8416–8428 (2013).

[145] S. C. Serra, M. Filibian, P. Carretta *et al.* Relevance of electron spin dissipative processes to dynamic nuclear polarization via thermal mixing. *Phys. Chem. Chem. Phys.* **16**, 753–764 (2014).

[146] W. de Boer, M. Borghini, K. Morimoto *et al.* Dynamic polarization of protons, deuterons, and carbon-13 nuclei: Thermal contact between nuclear spins and an electron spin-spin interaction reservoir. *J. Low Temp. Phys.* **15**, 249–267 (1974).

[147] J. H. Ardenkjaer-Larsen, B. Fridlund, A. Gram *et al.* Increase in signal-to-noise ratio of $>$ 10,000 times in liquid-state NMR. *Proc. Natl. Acad. Sci. U S A* **100**, 10158–10163 (2003).

[148] A. Kiswandhi, B. Lama, P. Niedbalski *et al.* The effect of glassing solvent deuteration and Gd^{3+} doping on ^{13}C DNP at 5 T". *RSC Adv.* **6**, 38855–38860 (2016).

[149] H. Sato, S. E. Bottle, J. P. Blinco *et al.* Electron spin-lattice relaxation of nitroxyl radicals in temperature ranges that span glassy solutions to low-viscosity liquids. *J. Magn. Reson.* **191**, 66–77 (2008).

[150] J. R. Harbridge, S. S. Eaton and G. R. Eaton. Electron Spin-Lattice Relaxation Processes of Radicals in Irradiated Crystalline Organic Compounds. *J. Phys. Chem. A* **107**, 598–610 (2003).

[151] M. Kveder, D. Merunka, M. Jokic *et al.* Electron spin-lattice relaxation in solid ethanol: Effect of nitroxyl radical hydrogen bonding and matrix disorder. *Phys. Rev. B* **80**, 052201 (2009).

[152] K. P. Scharwachter, D. H. Hochmuth, H. Dittmann *et al.* Synthesis, resolution, and investigation of the rotational interconversion process of atropisomeric 1,n-diaza[n]paracyclophanes using cyclodextrin-mediated capillary zone electrophoresis. *Chirality* **13**, 679–690 (2001).

[153] S. Shimpi, B. Chauhan, P. Shimpi *et al.* Cyclodextrins: application in different routes of drug administration. *Acta Pharm.* **55**, 139–156 (2005).

[154] K. Kaminski, K. Adrjanowicz, E. Kaminska *et al.* Impact of water on molecular dynamics of amorphous α-, β-, and γ-cyclodextrins studied by dielectric spectroscopy. *Phys. Rev. E* **86**, 031506 (2012).

[155] T. Takahashi, D. Jerome and K. Bechgaard. An NMR study of the organic superconductor : $(\mathrm{TMTSF})_2\mathrm{ClO}_4$. *J. Phys. France* **45**, 945–952 (1984).

[156] C. Casati, P. Franchi, R. Pievo *et al.* Unraveling Unidirectional Threading of α-Cyclodextrin in a [2]Rotaxane through Spin Labeling Approach. *J. Am. Chem. Soc.* **134**, 19108–19117 (2012).

[157] I. D. Sahu and G. A. Lorigan. Electron Paramagnetic Resonance as a Tool for Studying Membrane Proteins. *Biomolecules* **10**, 763 (2020).

[158] M. McEntee, W. Tang, M. Neurock *et al.* Mechanistic Insights into the Catalytic Oxidation of Carboxylic Acids on Au/TiO_2: Partial Oxidation of Propionic and Butyric Acid to Gold Ketenylidene through Unsaturated Acids. *ACS Catal.* **5**, 744–753 (2015).

[159] H. Kroemer. Theory of the Gunn effect. *Proc. IEEE* **52**, 1736–1736 (1964).

[160] W. R. Hagen. *Biomolecular EPR spectroscopy* (CRC press, 2008).

[161] A. S. Gilmour. *Klystrons, Traveling Wave Tubes, Magnetrons, Cross-Field Amplifiers, and Gyrotrons* (Artech House, UK, 2011).